

# Innovative Nanomaterials for Thermal Applications

Guest Editors: Yan Wang, Hua Bao, Yalin Dong, Rajib Paul,  
and Hua Deng





---

# **Innovative Nanomaterials for Thermal Applications**

Journal of Nanomaterials

---

## **Innovative Nanomaterials for Thermal Applications**

Guest Editors: Yan Wang, Hua Bao, Yalin Dong, Rajib Paul,  
and Hua Deng



---

Copyright © 2017 Hindawi Publishing Corporation. All rights reserved.

This is a special issue published in "Journal of Nanomaterials." All articles are open access articles distributed under the Creative Commons Attribution License, which permits unrestricted use, distribution, and reproduction in any medium, provided the original work is properly cited.

## Editorial Board

- Domenico Acierno, Italy  
Katerina Aifantis, USA  
Nageh K. Allam, USA  
M. Amaral, Portugal  
Martin Andersson, Sweden  
Raul Arenal, Spain  
Ilaria Armentano, Italy  
Vincenzo Baglio, Italy  
Lavinia Balan, France  
Thierry Baron, France  
Andrew R. Barron, USA  
Hongbin Bei, USA  
Daniel Bellet, France  
Stefano Bellucci, Italy  
Enrico Bergamaschi, Italy  
Samuel Bernard, France  
D. Bhattacharyya, New Zealand  
Sergio Bietti, Italy  
Giovanni Bongiovanni, Italy  
Theodorian Borca-Tasciuc, USA  
Mohamed Bououdina, Bahrain  
Torsten Brezesinski, Germany  
C. Jeffrey Brinker, USA  
Christian Brosseau, France  
Philippe Caroff, Australia  
V. M. Castaño, Mexico  
Albano Cavaleiro, Portugal  
Bhanu P. S. Chauhan, USA  
Shafiu Chowdhury, USA  
Jin-Ho Choy, Republic of Korea  
Kwang-Leong Choy, UK  
Yu-Lun Chueh, Taiwan  
Elisabetta Comini, Italy  
Giuseppe Compagnini, Italy  
David Cornu, France  
M. A. Correa-Duarte, Spain  
P. Davide Cozzoli, Italy  
Shadi A. Dayeh, USA  
Luca Deseri, USA  
Yong Ding, USA  
Philippe Dubois, Belgium  
Zehra Durmus, Turkey  
Joydeep Dutta, Oman  
Ali Eftekhari, USA  
Samy El-Shall, USA
- Ovidiu Ersen, France  
Claude Estournès, France  
Andrea Falqui, KSA  
Matteo Ferroni, Italy  
Ilaria Fratoddi, Italy  
Alan Fuchs, USA  
Miguel A. Garcia, Spain  
S. Ghosh, Singapore  
P. K. Giri, India  
Russell E. Gorga, USA  
Jihua Gou, USA  
Jean M. Greneche, France  
Smrati Gupta, Germany  
Kimberly Hamad-Schifferli, USA  
Simo-Pekka Hannula, Finland  
Michael Harris, USA  
Yasuhiko Hayashi, Japan  
F. Hernandez-Ramirez, Spain  
Michael Z. Hu, USA  
Nay Ming Huang, Malaysia  
Shaoming Huang, China  
Zafar Iqbal, USA  
Balachandran Jeyadevan, Japan  
Xin Jiang, Germany  
Rakesh Joshi, Australia  
J.-w. Kang, Republic of Korea  
Hassan Karimi-Maleh, Iran  
Antonios Kelarakis, UK  
Alireza Khataee, Iran  
Ali Khorsand Zak, Iran  
Philippe Knauth, France  
Ralph Krupke, Germany  
Christian Kübel, Germany  
Prashant Kumar, UK  
Eric Le Bourhis, France  
Jun Li, Singapore  
Meiyong Liao, Japan  
Shijun Liao, China  
Silvia Licoccia, Italy  
Wei Lin, USA  
Nathan C. Lindquist, USA  
Zainovia Lockman, Malaysia  
Nico Lovergine, Italy  
Jim Low, Australia  
Jue Lu, USA
- Ed Ma, USA  
Laura M. Maestro, Spain  
Gaurav Mago, USA  
Muhamamd A. Malik, UK  
Devanesan Mangalaraj, India  
F. Marotti de Sciarra, Italy  
Sanjay R. Mathur, Germany  
Tony McNally, UK  
Yogendra Mishra, Germany  
Paulo Cesar Morais, Brazil  
Paul Munroe, Australia  
J.-M. Myoung, Republic of Korea  
Rajesh R. Naik, USA  
Albert Nasibulin, Russia  
Toshiaki Natsuki, Japan  
Koichi Niihara, Japan  
Natalia Noginova, USA  
Sherine Obare, USA  
Won-Chun Oh, Republic of Korea  
Atsuto Okamoto, Japan  
Abdelwahab Omri, Canada  
Ungyu Paik, Republic of Korea  
Piersandro Pallavicini, Italy  
Edward A. Payzant, USA  
Alessandro Pegoretti, Italy  
Ton Peijs, UK  
O. Perales-Pérez, Puerto Rico  
Jorge Pérez-Juste, Spain  
Alexey P. Popov, Finland  
Philip D. Rack, USA  
Peter Reiss, France  
Orlando Rojas, USA  
Marco Rossi, Italy  
Ilker S. Bayer, Italy  
Cengiz S. Ozkan, USA  
Sudipta Seal, USA  
Shu Seki, Japan  
V. Šepelák, Germany  
Huaiyu Shao, China  
Prashant Sharma, USA  
Donglu Shi, USA  
Bhanu P. Singh, India  
Surinder Singh, USA  
Vladimir Sivakov, Germany  
Adolfo Speghini, Italy



---

Marinella Striccoli, Italy  
Xuping Sun, KSA  
Ashok K. Sundramoorthy, India  
Angelo Taglietti, Italy  
Bo Tan, Canada  
Leander Tapfer, Italy  
Valeri P. Tolstoy, Russia  
Muhammet S. Toprak, Sweden  
R. Torrecillas, Spain  
Achim Trampert, Germany

Takuya Tsuzuki, Australia  
Tamer Uyar, Turkey  
Bala Vaidhyanathan, UK  
Luca Valentini, Italy  
Ester Vazquez, Spain  
Ajayan Vinu, Australia  
Ruibing Wang, Macau  
Shiren Wang, USA  
Yong Wang, USA  
M. Willander, Sweden

Ping Xiao, UK  
Zhi Li Xiao, USA  
Yangchuan Xing, USA  
Doron Yadlovker, Israel  
Yoke K. Yap, USA  
Kui Yu, Canada  
William Yu, USA  
Michele Zappalorto, Italy  
Renyun Zhang, Sweden

# Contents

---

## **Innovative Nanomaterials for Thermal Applications**

Yan Wang, Hua Bao, Yalin Dong, Rajib Paul, and Hua Deng  
Volume 2017, Article ID 6540120, 2 pages

## **Study on NO Heterogeneous Reduction Mechanism under Gasification Condition**

Xiangyong Huang, Chengbin Zhang, Xiaochuan Li, and Che Huang  
Volume 2016, Article ID 1735929, 8 pages

## **Thermal Properties of Silver Nanoparticle Sintering Bonding Paste for High-Power LED Packaging**

Ping Zhang, Rongzhuang Wei, Jianhua Zeng, Miao Cai, Jing Xiao, and Daoguo Yang  
Volume 2016, Article ID 8681513, 6 pages

## **Nonlinear Absorptions of CdSeTe Quantum Dots under Ultrafast Laser Radiation**

Zhijun Chai, Yachen Gao, Degui Kong, and Wenzhi Wu  
Volume 2016, Article ID 9138059, 5 pages

## **Effect of Strain on Thermal Conductivity of Si Thin Films**

Xingli Zhang and Guoqiang Wu  
Volume 2016, Article ID 4984230, 5 pages

## **Synthesis and Thermoelectric Properties of C<sub>60</sub>/Cu<sub>2</sub>GeSe<sub>3</sub> Composites**

Degang Zhao, Jiai Ning, Shuyu Li, and Min Zuo  
Volume 2016, Article ID 5923975, 7 pages

## **Active Multiple Plasmon-Induced Transparency with Graphene Sheets Resonators in Mid-Infrared Frequencies**

Jicheng Wang, Baojie Tang, Xiushan Xia, and Shutian Liu  
Volume 2016, Article ID 3678578, 8 pages

## Editorial

# Innovative Nanomaterials for Thermal Applications

**Yan Wang,<sup>1</sup> Hua Bao,<sup>2</sup> Yalin Dong,<sup>3</sup> Rajib Paul,<sup>4,5</sup> and Hua Deng<sup>6</sup>**

<sup>1</sup>*Department of Mechanical Engineering, University of Nevada, Reno, NV 89557, USA*

<sup>2</sup>*University of Michigan-Shanghai Jiao Tong University Joint Institute, Shanghai Jiao Tong University, Shanghai 200240, China*

<sup>3</sup>*Department of Mechanical Engineering, University of Akron, Akron, OH 44325, USA*

<sup>4</sup>*Department of Macromolecular Science and Engineering, Case Western Reserve University, Cleveland, OH 44106, USA*

<sup>5</sup>*Department of Physics, Heritage Institute of Technology, Anandapur, Kolkata 700107, India*

<sup>6</sup>*Western Digital Corporation, San Jose, CA 95131, USA*

Correspondence should be addressed to Yan Wang; wang896@purdue.edu

Received 6 November 2016; Accepted 7 November 2016; Published 29 January 2017

Copyright © 2017 Yan Wang et al. This is an open access article distributed under the Creative Commons Attribution License, which permits unrestricted use, distribution, and reproduction in any medium, provided the original work is properly cited.

With continued advancement in nanotechnology, numerous innovative nanomaterials, possessing internal features or surface structures of nanoscale dimension, have emerged as golden materials for sustainable and efficient energy solutions. Thermal properties of nanomaterials depend upon many factors that are usually insignificant in bulk materials. In particular, surface properties, interfacial structures, and quantum or classical size effects prominently determine the thermal transport in nanomaterials, leading to carrier scatterings and localization that are otherwise absent or unobvious in bulk materials.

Through this special issue, we aim to enlighten the fundamental understanding of thermal transport and energy conversion processes at the nanoscale and facilitate the development of innovative nanomaterials for thermal applications.

In D. Zhao et al.'s work, nanosized  $C_{60}$  powder was incorporated with  $Cu_2GeSe_3$  powder by ball milling and then  $C_{60}/Cu_2GeSe_3$  composites were prepared by spark plasma sintering. The authors found that as the concentration of  $C_{60}$  increases, the electrical resistivity and the Seebeck coefficient of  $C_{60}/Cu_2GeSe_3$  composites increase while the thermal conductivity decreases significantly. A maximum figure of merit  $ZT$  of 0.20 has been achieved at 700 K for the 0.9%- $C_{60}/Cu_2GeSe_3$  composites, rendering this material potentially useful for high temperature applications.

In P. Zhang et al.'s work, low-temperature sintered nanosilver pastes were attempted to interconnect large-power LED and substrates. The authors found that the shear strength

of the low-temperature sintered nanosilver paste increases as the temperature or pressure increases. This material also shows relatively low thermal resistance.

X. Zhang and G. Wu conducted nonequilibrium molecular dynamics simulations of strained Si thin films. The thermal conductivity was found to decrease as the tensile strain increases and increase as the compressive strain increases, which could aid the modification of the thermal conductivity, and, moreover, the thermal management of Si-thin-film-based devices.

Z. Chai et al. investigated nonlinear absorption of CdSeTe quantum dots in toluene using the femtosecond Z-scan technique at 800 nm. The authors investigated the open-aperture Z-scan behaviors of the samples on the local nonlinear responses, including two-phonon absorption (TPA) coefficient. It was demonstrated that, under the conditions of high-repetition rate, heat accumulation and bleaching of ground state are responsible for the decrease of the TPA coefficient.

J. Wang et al. proposed a multiple plasmon-induced transparency (PIT) device operated in the midinfrared region and investigated the phase coupling between two graphene resonators. The multimode PIT resonances were found to be dynamically tunable by varying the chemical potential of graphene resonators, which could be potentially useful for various energy applications.

X. Huang et al. used the density functional theory to study the chemisorption of NO and successive heterogeneous

reduction mechanisms on the well-defined char models under carbon/char-CO<sub>2</sub> gasification condition. Their results indicate that intensive gasification surface is likely to be thermally unfavorable and the O-down mode is regarded as the most inactive pathway for the absorption of NO.

All these papers show how nanomaterials can be well understood and utilized for various thermal and energy applications.

### **Acknowledgments**

The guest editors would like to thank the authors who contributed to this issue. The lead guest editor would like to thank all the other guest editors for their dedication to this issue.

*Yan Wang  
Hua Bao  
Yalin Dong  
Rajib Paul  
Hua Deng*

## Research Article

# Study on NO Heterogeneous Reduction Mechanism under Gasification Condition

Xiangyong Huang,<sup>1,2</sup> Chengbin Zhang,<sup>1</sup> Xiaochuan Li,<sup>2</sup> and Che Huang<sup>2</sup>

<sup>1</sup>Key Laboratory of Energy Thermal Conversion and Control of Ministry of Education, School of Energy and Environment, Southeast University, Nanjing, Jiangsu 210096, China

<sup>2</sup>School of Hydraulic, Energy and Power Engineering, Yangzhou University, Yangzhou, Jiangsu 225127, China

Correspondence should be addressed to Chengbin Zhang; cbzhang@seu.edu.cn

Received 6 May 2016; Revised 18 July 2016; Accepted 27 July 2016

Academic Editor: Rajib Paul

Copyright © 2016 Xiangyong Huang et al. This is an open access article distributed under the Creative Commons Attribution License, which permits unrestricted use, distribution, and reproduction in any medium, provided the original work is properly cited.

Chemisorption of NO and successive heterogeneous reduction mechanisms on the well-defined char models under carbon/char-CO<sub>2</sub> gasification condition were investigated using density functional theory at the B3LYP/6-31G (d) level of theory. The characteristics of gasification process were concluded and incorporated into the theoretical calculations by establishing three gasification char models and taking into account the presence of CO in ambient gas pool. The results indicate that both the configuration of char model and adsorption mode have significant influence on the NO adsorption energy. Intensive gasification surface is likely to be thermally unfavorable and the O-down mode is regarded as the most inactive approach for NO's adsorbing. Finally, NO heterogeneous reduction mechanisms on the three char models under gasification are proposed based on detailed analysis on thermodynamic data and atomic bond populations.

## 1. Introduction

Understanding the conversion mechanism of nitric oxide (NO) in combustion and coal conversion processes is the basis of controlling and reducing NO emission. Extensive researches have been conducted on the heterogeneous reaction between NO and char/carbonaceous surface [1–3]. The electrons/atoms/molecules involved in the reactions are microscopically small and transfer fast enough beyond the detection limits of instruments, especially at high temperature exceeding several hundred degrees Celsius. Therefore, they are hard to be directly observed in experiments, which hinders the intrinsic understanding. Quantum chemical calculations, providing a promising alternative method to obtain the mechanistic information such as geometries, energies, and vibrational frequencies for the explanation of macroscopic experimental results, have been regarded as an effective tool for removing the barriers.

A pioneering work conducted by Kyotani and Tomita [4] focused on the reaction of carbon and NO or N<sub>2</sub>O by using ab initio molecular orbital theory. A mechanism of N<sub>2</sub> formation

from C-NO or C-N<sub>2</sub>O reaction was proposed. Montoya et al. [3] investigated the heterogeneous pathways for the reaction  $C(N) + NO \rightarrow N_2 + N_2O + CO$  in the presence of O<sub>2</sub>. They found that the reaction of NO molecule with char yields predominantly N<sub>2</sub> and CO and small amount of N<sub>2</sub>O in the presence of O<sub>2</sub>.

Recently, Jiang's team [1, 5] carried out a series of density functional theory (DFT) calculations to study the heterogeneous reduction between NO and char-bound nitrogen. NO chemisorption of direct nitrogen-nitrogen interaction and N<sub>2</sub> desorption from medium chemisorbed surface during coal combustion were investigated based on thermodynamics and kinetics evaluation. Reaction rate of rate-limiting step involved in N<sub>2</sub> desorption and the overall NO reduction rate were obtained.

These studies above opened the door a crack for a molecular-level understanding of the heterogeneous reactions between NO and char/carbon. However, the understanding of the process is still far from complete because of the complexity of gas-solid heterogeneous interaction. Most studies have focused on the conventional air-fired

conditions and less information is available on the molecular explanation for gasification condition or combustion with high concentration of CO<sub>2</sub>. The aim of the present study is to set up molecular char models suitable for gasification condition and propose a preliminary NO heterogeneous reduction mechanism using DFT calculations.

## 2. Computational Details

*2.1. Physical Model.* It is widely accepted that CO<sub>2</sub> gasification of coal char plays an important role during the coal conversion process and some combustion technologies such as oxyfuel combustion with CO<sub>2</sub> concentration in flue gas over 60% [6]. Not only the fundamental combustion issues such as coal ignition and char burnout but also pollutant abatement issues such as nitrogen conversion are all affected by gasification reactions [7–9]. Therefore, it is essential to take into account the effects of CO<sub>2</sub> gasification in quantum chemical calculations. In the present work, the issue is treated deliberately and the solution is implemented by establishing appropriate char models and taking into account the presence of CO, an important product of CO<sub>2</sub> gasification, in ambient gas pool.

Actually, the gasification process, especially the reactions of char/carbon with the oxygen-containing gases, O<sub>2</sub>, CO<sub>2</sub>, and H<sub>2</sub>O, has been studied extensively for it is coupled in many thermal conversions processes [10, 11]. Different gasification mechanisms have been proposed using quantum chemical calculation based on experimental observations. A common procedure comprising three brief steps is concluded as follows:

- (1) An oxygen-containing gas molecule firstly is chemisorbed onto a well-defined carbon surface and covers some active sites.
- (2) Oxygen atom(s) covalently bond to a carbon atom and remain on the surface while the other atoms leave from the surface after a series of elementary reactions.
- (3) The C-C bonding in the parent carbon matrix is weakened by the C-O bonding and leads to breakage. Finally, the oxygen atom(s) leave the surface in the formation of CO or CO<sub>2</sub> and some active sites are created.

In the procedure, the oxygen atom's adsorption and desorption lead to the cyclic change of active sites on carbon surface, which drives the gasification reaction cycle to loop continuously. Therefore, the carbon surface with adsorbed oxygen atom(s) can be regarded as a symbolical structure in carbon/char-CO<sub>2</sub> gasification. Moreover, the accumulation of oxygen atom on char surface will increase when the gasification reaction becomes intense due to more reactions occurring simultaneously. Based on the recognition, three char models used in this work are proposed and presented in Figure 1. Each model is characterized by the attachment of O atom(s) to a conventional char model in zigzag configuration (five six-membered benzene rings). The number of oxygen atoms is an indicator of gasification condition; that is, one, two, and three preadsorbed O atom(s) correspond to mild

gasification, moderate gasification, and intensive gasification, respectively.

The conventional char model in zigzag configuration with five six-membered benzene rings is chosen as a main frame here due to the following merits:

- (1) The model possesses good physical reality and its size and configuration are in accordance with experimental observation [11].
- (2) The suitable size of the model not only is large enough to minimize edge effects but also gives a reasonable tradeoff between accuracy and computational cost.

*2.2. Chemical Method.* All calculations were conducted at the B3LYP DFT level of theory with the 6-31G(d) basis set. This method is recognized to produce fairly accurate bond energies, thermodynamic data, and reasonably small spin contamination [12, 13]. It has been proved to be rational to apply the method to polyaromatic molecules by a lot of previous work [4, 11]. The spin multiplicity of each structure was determined with the typical procedure as that described in literature [4]. Single point energy calculations at several electronic states are performed and the one giving the lowest energy is determined as the electronic ground state. The default convergence criteria embedded in Gaussian (maximum force, <0.000450; RMS (root-mean-square) force, <0.000300; maximum displacement, <0.001800; and RMS displacement, <0.001200, all the values in atomic units) were used in geometry optimization.

The heat of reaction, denoted by  $\Delta H$ , is defined as a difference between the total energies of the optimized products and the sum of the energies of the corresponding reactants. The possible paths of NO heterogeneous reduction over gasification char surface have been evaluated according to the thermal parameters and bonding strengths of the species involved in the process. All calculations were carried out using the Gaussian 09 package [14].

## 3. Results and Discussion

*3.1. Chemisorption of NO on the Char Models.* Chemisorption is crucial in many cases for a reaction because it initiates the subsequent reactions. And thus, the configuration of the reaction system is largely determined by chemisorption process. Theoretical calculations on NO adsorption on the three char models were made to obtain the characteristics of NO adsorption on the char models. The typical adsorption modes used in this work are shown in Figure 2.

As seen from Figure 3, it could be concluded that both the configuration of char model and adsorption mode have significant influence on the NO adsorption energy obtained from frequency calculation. The adsorption energy varies dramatically with different char models. For side-on mode and vertical-N-down mode, the energy value decreases roughly as the number of preadsorbed O atoms increases with the same adsorption mode; that is, the adsorption energy is generally ranked in a descending order for certain adsorption mode:  $\Delta H_{ad,M0} > \Delta H_{ad,M1} > \Delta H_{ad,M2} > \Delta H_{ad,M3}$ . But the O-down mode does not satisfy the principle. However, it is

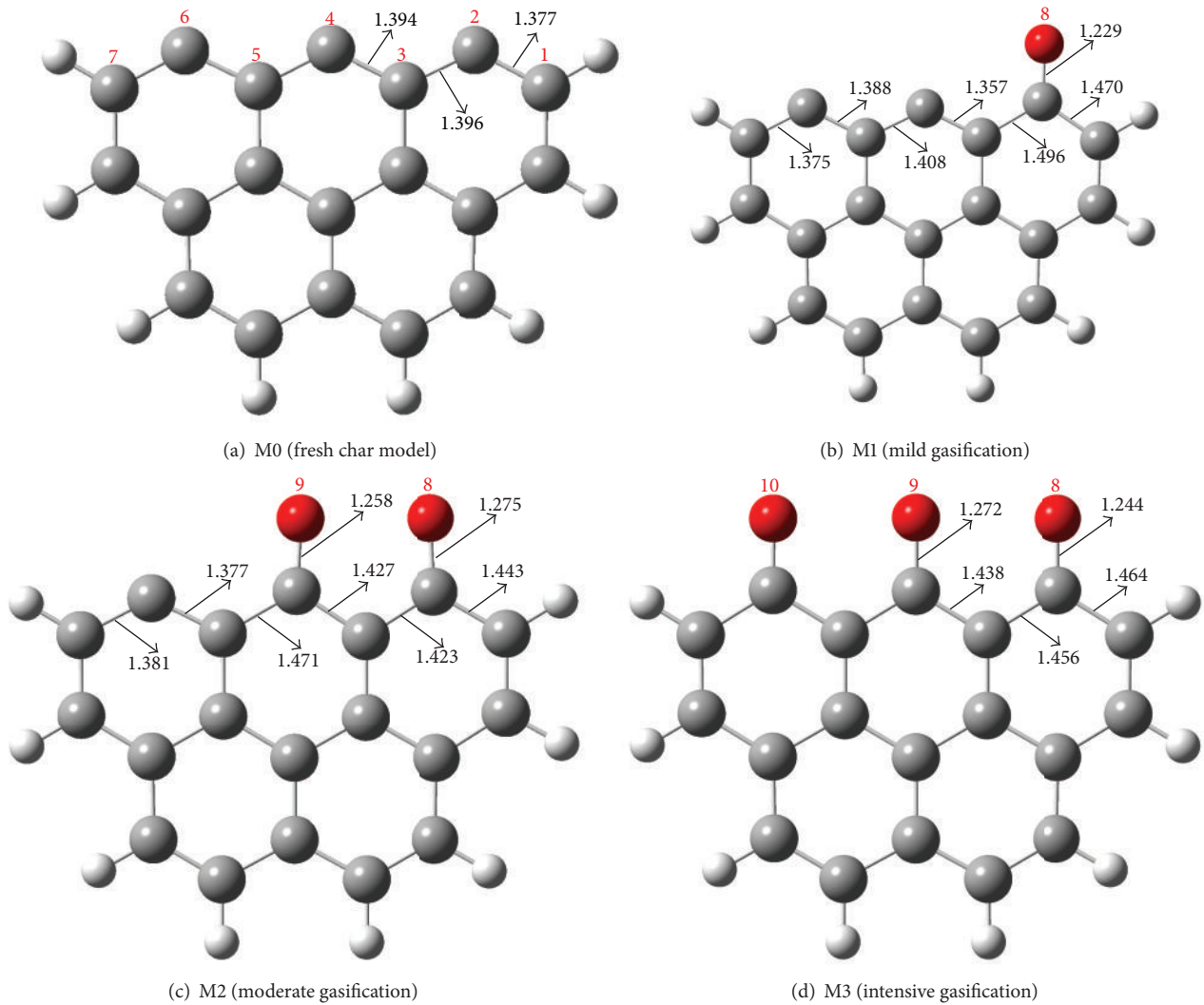


FIGURE 1: Char models in gasification (bond lengths are given in angstroms. The numerical order of the first C layer in other species is the same as that in M0).

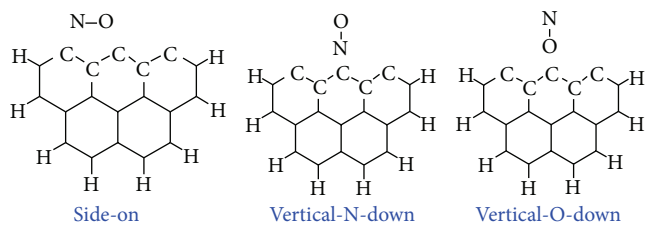


FIGURE 2: Schematic diagram of side-on, N-down, and O-down modes for NO adsorption.

deduced that the char surface where gasification reactions are taking place is not favorable to the NO adsorption. Actually, the adsorption energies are all close to zero for all modes with the M3 model, which means that it is difficult for NO to bond well with the intensive gasification surface or NO can only physically adsorb on the surface. Hence, the conclusion may have negative impact on the follow-up NO

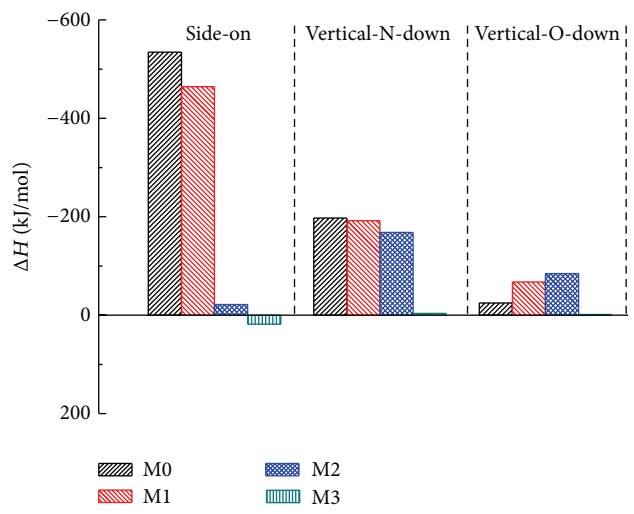


FIGURE 3: Adsorption heat of NO on char surface under gasification condition.

heterogeneous reduction on coal char. Fortunately, there still exist several positive factors: (1) the gasification reactions proceed with carbon-CO<sub>2</sub> interaction cycles involving a dynamic balance of active sites. The balance is implemented by the consumption by small gaseous molecules' adsorption and the generation by surface complex's leaving the matrix with bond cleavage. Therefore, in practical application, there remain active sites for NO to be adsorbed even for intensive gasification condition; (2) the CO concentration near the char surface is rather great due to the accumulation resulting from limited CO diffusion rate and high CO generation rate. As a consequence, the oxygen is consumed by the remaining CO and the oxidation of nitrogen-containing is inhibited. Moreover, the presence of CO increases the reducibility of the atmosphere, which is benefit for both homogeneous and heterogeneous reduction of NO<sub>x</sub>.

The adsorption modes have great influence on the magnitudes of the energy value. It is clearly indicated that, for the M0 and M1 models, the values magnitudes are ranked in a descending order:  $\Delta H_{ad,side-on}$  ( $\sim 500$  kJ/mol) >  $\Delta H_{ad,N-down}$  ( $\sim 200$  kJ/mol) >  $\Delta H_{ad,O-down}$  ( $\leq 100$  kJ/mol). However, it is not suitable for M2 and M3 models. It can be briefly concluded that, for the M0 and M1 models, the side-on mode can obtain the most stable structure while for the M2 model the N-down mode is the most stable way to be adsorbed.

Moreover, the adsorption modes differ in the sensitivity to the char models. For side-on mode, significant difference can be found in the adsorption energies with different char models while the other two modes seem less sensitive to the variation of char models, although their values are relatively small. It should be noted that the heat values of vertical-O-down mode with different char models are generally low and it can be regarded as the most inactive approach for NO to be adsorbed.

**3.2. NO Heterogeneous Reduction Mechanism on the M2 Char Model.** DFT calculations were conducted and the optimized structures discussed below are drawn in Figure 4 and the optimized parameters for the selected bonds of the structures involved in the NO heterogeneous reduction pathways are listed in Table 1. Some atoms of the species are numbered to facilitate the following discussions. For simplicity, NO heterogeneous reduction mechanism on the M2 char model is sometimes abbreviated to M2 pathway, and it is similar for the cases of the M1 char model and the M3 char model.

NO heterogeneous reduction process is initiated by its chemisorption on char surface. It has been identified N-down mode is the most stable chemisorption way for NO on model M2 and an intermediate, structure IM1, is generated by the chemisorption process with a transition state as depicted in Figure 5.

It can be seen that the N(10)-O(11) bond in IM1 exhibits a relatively weak bonding with a Milliken bond population of 0.184 which is lower significantly than that of other bonds. It is further reduced to 0.012 in IM2 and the corresponding bond length increases from 1.221 Å to 1.423 Å after a CO molecule's adsorption on IM1. And then the bond becomes weak enough

TABLE 1: Optimized parameters for the selected bonds of the structures involved in the NO heterogeneous reduction pathways.

Species	Bond	Length (Å)	Population
IM1	C(2)-O(8)	1.277	0.387
	C(4)-O9	1.263	0.453
	C(6)-N(10)	1.358	0.261
	N(10)-O(11)	1.221	0.184
IM2	C(2)-O(8)	1.269	0.405
	C(4)-O9	1.267	0.420
	C(6)-N(10)	1.340	0.342
	N(10)-O(11)	1.423	0.012
	O(11)-C(12)	1.333	0.159
	C(12)-O(13)	1.189	0.491
IM3	C(2)-O(8)	1.238	0.555
	C(4)-O9	1.359	0.192
	O9-N(10)	1.430	0.144
	N(10)-C(6)	1.336	0.299
IM4	C(2)-O(8)	1.233	0.548
	C(4)-O9	1.340	0.309
	C(6)-N(10)	1.321	0.387
	O9-C(11)	1.437	0.206
	C(11)-N(10)	1.377	0.331
	C(11)-O(12)	1.201	0.622
IM4-1	C(2)-O(8)	1.233	0.580
	C(4)-O9	1.372	0.207
	C(6)-N(10)	1.398	0.026
	N(10)-N(11)	1.339	0.035
	N(11)-O(12)	1.214	0.287
IM4-2	C(2)-O(8)	1.274	0.398
	C(4)-O9	1.260	0.451
	C(6)-N(10)	1.381	0.306
	N(10)-C(11)	1.207	0.548
	C(11)-O(12)	1.177	0.592
IM4-3	C(2)-O(8)	1.232	0.571
	C(6)-N9	1.297	0.418
	C(11)-N9	3.018	0.012
	C(11)-O(12)	1.167	0.587
	C(11)-O(10)	1.171	0.562
IM5	C(1)-C(2)	1.468	0.362
	C(2)-C(3)	1.489	0.196
	C(3)-C(4)	1.373	0.338
	C(4)-C(5)	1.387	0.302
	C(5)-C(6)	1.465	0.278
	C(6)-C(7)	1.454	0.340
	C(2)-O(8)	1.232	0.572
	C(6)-N(9)	1.297	0.445
IM6	C(2)-O(8)	1.243	0.512
	C(4)-O(9)	1.241	0.560
	C(6)-N(10)	1.339	0.182
	N(10)-N(11)	1.146	0.542

TABLE 1: Continued.

Species	Bond	Length (Å)	Population
IM7	C(2)-O(8)	1.357	0.194
	C(4)-N(9)	1.362	0.108
	C(6)-N(10)	1.301	0.436
	N(9)-O(11)	1.214	0.283
IM8	C(2)-O(8)	1.382	0.164
	C(4)-N(9)	1.377	0.085
	C(6)-N(10)	1.280	0.512
	N(9)-O(11)	1.426	0.033
	O(8)-N(9)	1.423	0.130
	O(11)-C(12)	1.321	0.156
IM9	C(12)-O(13)	1.187	0.491
	C(2)-O(8)	1.360	0.178
	N(9)-O(8)	1.435	0.125
	C(4)-N(9)	1.330	0.342
IM10	C(6)-N(10)	1.311	0.002
	C(2)-O(8)	1.225	0.558
	C(4)-N(9)	1.449	0.225
	N(9)-N(10)	1.285	0.300
IM11	C(6)-N(10)	1.441	0.174
	C(2)-O(9)	1.247	0.533
	C(4)-N(9)	1.340	0.190
IM12	N(9)-N(10)	1.139	0.562
	C(2)-O(8)	1.229	0.570
	C(4)-O(9)	1.375	0.255
	C(6)-O(10)	1.377	0.218
	C(11)-O(9)	1.366	0.263
	C(11)-O(10)	1.368	0.259
	C(11)-O(12)	1.191	0.648

to be easily ruptured. The thermodynamic calculation also shows that the breakage of the N-O bond is highly exothermic with  $\sim 400$  kJ/mol accompanying with the release of a  $\text{CO}_2$  molecule and the formation of an intermediate, IM3.

Structure IM3 plays an important role in the NO heterogeneous reduction because it not only introduces several different successive pathways after its interaction with CO and NO but also is a shared intermediate by M2 pathway and M3 pathway (see Figure 7). The N(10)-O(9) bond is found to be a tender point, and three different stable structures, IM4, IM4-1, and IM4-2, are obtained from further NO or CO adsorption on the active sites around the bond. IM4 seems to be the prime product among them from a thermodynamic view. The reaction channel that a CO molecule adsorbs onto IM3 with a C atom joining with N(10) and O(9) can result in the greatest  $\Delta H$  ( $\sim 200$  kJ/mol) while those of the other two channels are only 140 kJ/mol and 23 kJ/mol. Therefore, the  $\text{IM3} + \text{CO} \rightarrow \text{IM4}$  channel is more energetically favorable. However, further analysis on the atomic bond population shows that the newly formed C(11)-O(9) bond owns the smallest bond population in the structure. Calculations indicated the cleavage of the bond leads to the formation of IM4-2 in which N atom is eventually

released as NCO in a strongly endothermic reaction with heat absorbed of 438.2 kJ/mol. However, the reaction channel is not presented in the schematic diagram of NO heterogeneous reduction mechanism for its final product is not the expected  $\text{N}_2$  molecule. And thus, the C(4)-O(9) bond with the second smallest bond population is considered to examine the possibility. An intermediate IM4-3 is obtained from the presumed ring opening at the C(4)-O(9) bond. The calculation results indicated that the N(9)-C(11) bond in the structure IM4-3 becomes very fragile with a bond population of only 0.010. Eventually, a  $\text{CO}_2$  molecule escapes from the parent matrix and the left part is fully optimized to a stable structure IM5.

An active site is exposed at the unsaturated C(4) atom in IM5, which makes the intermediate a chemically active species. NO is expected to adhere to the C(4) atom to produce only two configurations, IM6 and IM7, when NO approaches toward the structure IM5 in either side-on or vertical-N-down/O-down mode. Each intermediate leads an individual reaction channel starting from IM5. And then, it is easily found the weakest bond of the structure IM6 exists between N(10) and C(6) while a strong bond exists between N(11) and N(10). And thus, the group of N(11)-N(10) shows an intensive tendency to be detached from the parent structure and leaves as a  $\text{N}_2$  molecule. This is supported by a thermodynamic analysis. Only a little external heat ( $\sim 1.24$  kJ/mol) is needed to drive the decomposition reaction  $\text{IM6} \rightarrow \text{M2} + \text{N}_2$  to complete the M2 pathway.

It is slightly more complicated for IM7 channel. The N(9)-C(4) bond, O(8)-C(2) bond, and N(9)-O(11) bond are all weakened by the CO adsorption on O(11). Their bond populations decreased by different degrees during the reaction  $\text{IM7} + \text{CO} \rightarrow \text{IM8}$ , especially for the N(9)-O(11) bond whose bond population drops from 0.283 to the minimal number of the structure, 0.033. Consequently, the bond becomes most likely to be cracked. The successive decomposition reaction  $\text{IM8} \rightarrow \text{IM9} + \text{CO}_2$  proceeds as expected and a large amount of heat (465.19 kJ/mol) is released at the same time. Afterward, two steps of configuration rearrangement,  $\text{IM9} \rightarrow \text{IM10} \rightarrow \text{IM11}$ , are found to occur with  $\Delta H$  of 306.59 and  $-384.00$ , respectively. Finally, the bonded N atoms leave the aromatic rings as a  $\text{N}_2$  molecule due to the weakness of the N(9)-C(4) bond in IM11, which terminates the M2 pathway with M1. The whole M2 pathway is schematically depicted in Figure 6 with the species and energies involved in the steps.

**3.3. NO Heterogeneous Reduction Mechanisms on M1 and M3 Model.** It is found that a significant number of reaction steps in the M1 and M3 pathways duplicate the existing ones in the M2 pathway which has been discussed in detail previously. For simplicity, only the differences are presented in Figure 7 and analyzed here.

As regards the M1 pathway, the side-on mode has been known to generate the most stable chemisorbed species, IM3, when NO interacts with M1 model. The energy barrier of the reaction is only 86.64 kJ/mol and seems to be passed over easily. The corresponding transition state is shown in Figure 8.

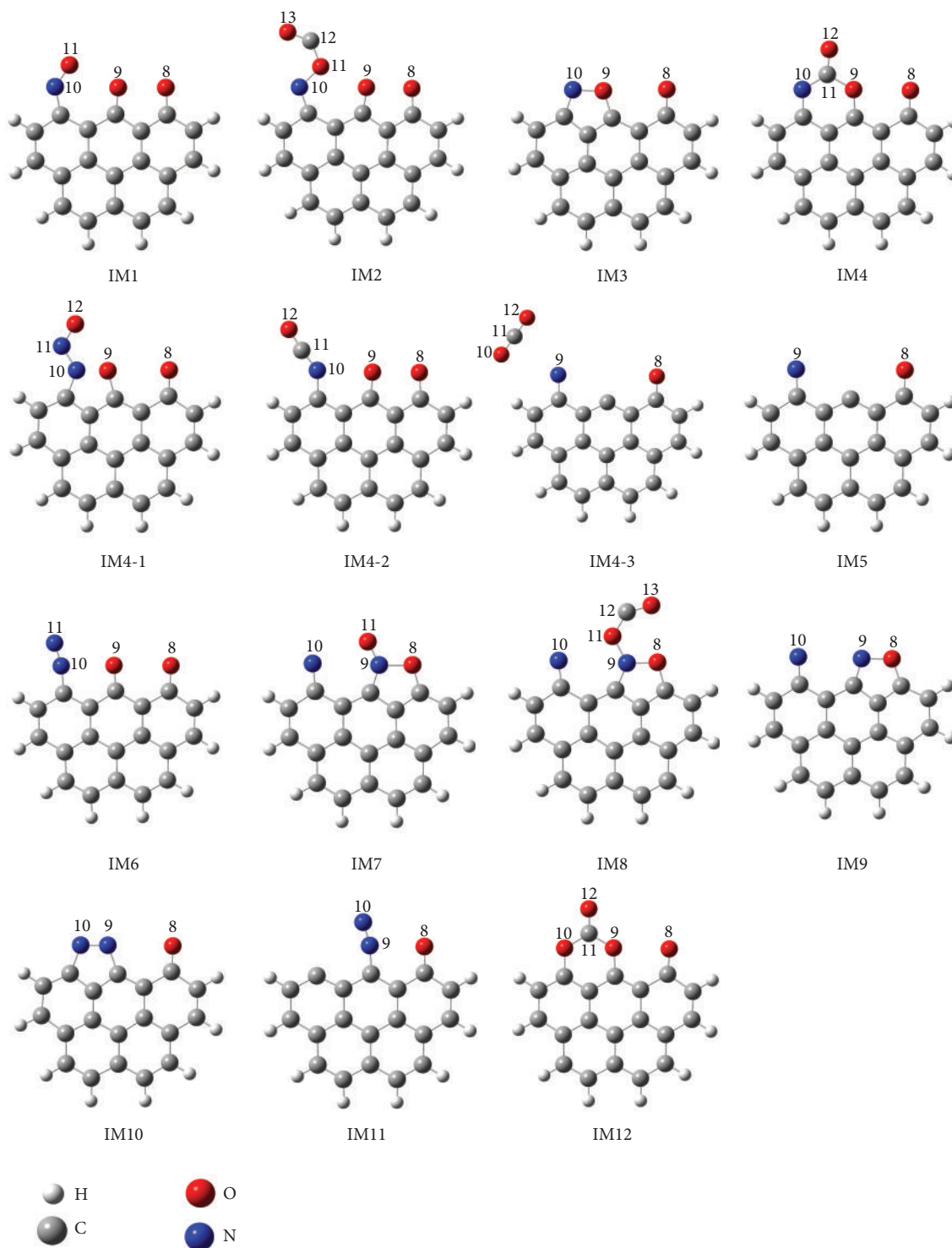


FIGURE 4: Optimized structures of stable intermediates involved in NO heterogeneous reduction. The numerical order of the first C layer in other species is the same as that in M0.

The reaction is thermally favorable with 464.13 kJ/mol, which increases the possibility for NO reduction to take place along this path. As for the M3 pathway, it is reasonable to take CO chemisorption onto M3 as an initial step, considering that it is difficult for M3 to adsorb NO stably but can easily

capture CO. The CO adsorption seems to have a greater influence on the side C-O bond (C(6)-O(10)) than that on the middle one (C(4)-O(9)). The C(6)-O(10) bond with a bond population of 0.504 is stronger than the C(4)-O(9) bond with 0.408 in M3 model. However, the former turns out to

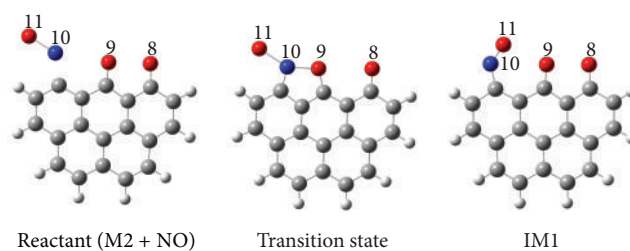


FIGURE 5: The transition state of reaction  $M2 + NO \rightarrow IM1$ . Bond length: N(10)-O(11): 1.801 Å; C(6)-N(10): 1.336 Å; O(9)-N(10): 1.677 Å; C(4)-O(9): 1.315 Å; and C(2)-O(8): 1.238 Å.

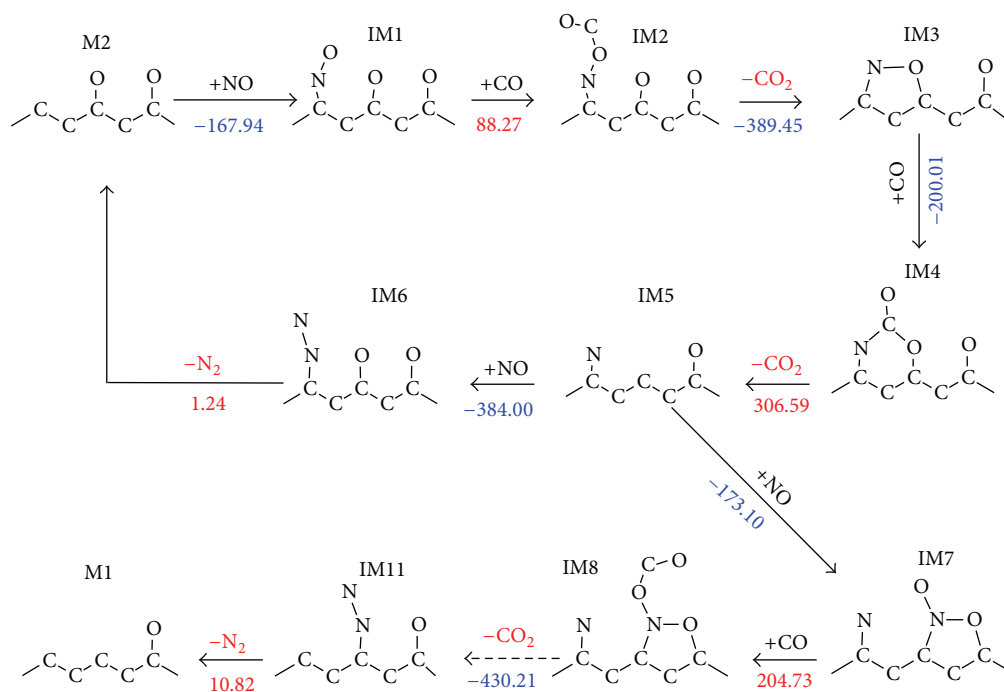


FIGURE 6: Pathways of NO heterogeneous reduction on M2 under gasification condition.

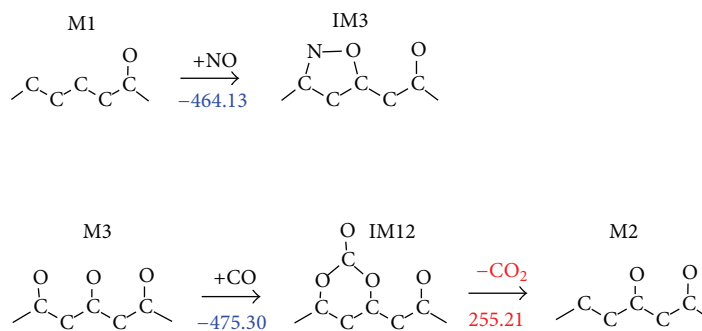


FIGURE 7: The first step(s) of NO heterogeneous reduction on M1 and M3 models.

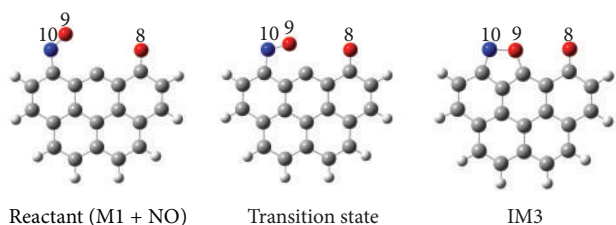


FIGURE 8: The transition state of reaction  $M1 + NO \rightarrow IM3$ . Bond length: N(10)-O(9): 1.224 Å; N(10)-C(6): 1.348 Å; O(9)-C(4): 2.925 Å; and C(2)-O(8): 1.231 Å.

be weaker with a bond population of 0.218 than the latter with 0.255 after the CO adsorption. As a result, the C(6)-O(10) bond breaking occurs due to the lowest population in IM12. Afterward, the C(11)-O(9) bond shows its weakness and is subjected to a cleavage. Finally a  $CO_2$  molecule is released and the transformation of IM12 to M2 takes place.

#### 4. Conclusions

Attempts have been made in the present study to investigate NO heterogeneous reduction on char surface under gasification by using DFT calculations. On the basis of the data acquired from our calculations, the following conclusions are drawn:

- (1) The characteristics of gasification reactions are analyzed in detail and implemented in our theoretical calculation by designing a conventional char model with preadsorbed O atom as gasification and considering the presence of CO in every reaction step.
- (2) Both the configuration of char model and adsorption mode were found to have significant influence on the NO adsorption energy. For side-on mode and vertical-N-down mode, the energy value decreases roughly as the number of preadsorbed O atoms increases. For the M0 and M1 models, the side-on mode can obtain the most stable structure while for the M2 model the N-down mode is the most stable way for adsorption.
- (3) A significant number of reaction steps in the M1, M2, and M3 pathways are repetitive. The pathways for NO heterogeneous reduction on the char models under gasification are proposed based on the detailed analysis on thermodynamic energy and bonding strength.

#### Competing Interests

The authors declare that they have no competing interests.

#### Acknowledgments

The authors gratefully acknowledge the financial supports by the National Natural Science Foundation of China (Project no. 51306158), Natural Science Foundation of Jiangsu

Province (no. BK20130621), and China Postdoctoral Science Foundation (no. 2015T80478 and no. 2014M561551).

#### References

- [1] H. Zhang, J. Liu, J. Shen, and X. Jiang, "Thermodynamic and kinetic evaluation of the reaction between NO (nitric oxide) and char(N) (char bound nitrogen) in coal combustion," *Energy*, vol. 82, pp. 312–321, 2015.
- [2] A. M. Oyarzún, L. R. Radovic, and T. Kyotani, "An update on the mechanism of the graphene-NO reaction," *Carbon*, vol. 86, pp. 58–68, 2015.
- [3] A. Montoya, T. N. Truong, and A. F. Sarofim, "Application of density functional theory to the study of the reaction of NO with char-bound nitrogen during combustion," *Journal of Physical Chemistry A*, vol. 104, no. 36, pp. 8409–8417, 2000.
- [4] T. Kyotani and A. Tomita, "Analysis of the reaction of carbon with NO/N<sub>2</sub>O using Ab initio molecular orbital theory," *Journal of Physical Chemistry B*, vol. 103, no. 17, pp. 3434–3441, 1999.
- [5] H. Zhang, X. M. Jiang, J. X. Liu, and J. Shen, "New insights into the heterogeneous reduction reaction between NO and char-bound nitrogen," *Industrial & Engineering Chemistry Research*, vol. 53, no. 15, pp. 6307–6315, 2014.
- [6] B. J. P. Buhre, L. K. Elliott, C. D. Sheng, R. P. Gupta, and T. F. Wall, "Oxy-fuel combustion technology for coal-fired power generation," *Progress in Energy and Combustion Science*, vol. 31, no. 4, pp. 283–307, 2005.
- [7] A. Molina and C. R. Shaddix, "Ignition and devolatilization of pulverized bituminous coal particles during oxygen/carbon dioxide coal combustion," *Proceedings of the Combustion Institute*, vol. 31, no. 2, pp. 1905–1912, 2007.
- [8] T. Suda, K. Masuko, J. Sato, A. Yamamoto, and K. Okazaki, "Effect of carbon dioxide on flame propagation of pulverized coal clouds in CO<sub>2</sub>/O<sub>2</sub> combustion," *Fuel*, vol. 86, no. 12–13, pp. 2008–2015, 2007.
- [9] H. Liu, R. Zailani, and B. M. Gibbs, "Comparisons of pulverized coal combustion in air and in mixtures of O<sub>2</sub>/CO<sub>2</sub>," *Fuel*, vol. 84, no. 7–8, pp. 833–840, 2005.
- [10] L. R. Radovic, "The mechanism of CO<sub>2</sub> chemisorption on zigzag carbon active sites: A Computational Chemistry study," *Carbon*, vol. 43, no. 5, pp. 907–915, 2005.
- [11] N. Chen and R. T. Yang, "Ab Initio molecular orbital study of the unified mechanism and pathways for gas-carbon reactions," *Journal of Physical Chemistry A*, vol. 102, no. 31, pp. 6348–6356, 1998.
- [12] A. Montoya, F. Mondragón, and T. N. Truong, "CO<sub>2</sub> adsorption on carbonaceous surfaces: A Combined Experimental and Theoretical Study," *Carbon*, vol. 41, no. 1, pp. 29–39, 2003.
- [13] K. Sendt and B. S. Haynes, "Density functional study of the reaction of O<sub>2</sub> with a single site on the zigzag edge of graphene," *Proceedings of the Combustion Institute*, vol. 33, no. 2, pp. 1851–1858, 2011.
- [14] M. J. Frisch, G. W. Trucks, H. B. Schlegel et al., *Gaussian 09, Revision B.01*, Gaussian, Wallingford, Conn, USA, 2010.

## Research Article

# Thermal Properties of Silver Nanoparticle Sintering Bonding Paste for High-Power LED Packaging

Ping Zhang,<sup>1,2</sup> Rongzhan Wei,<sup>1</sup> Jianhua Zeng,<sup>1</sup> Miao Cai,<sup>1</sup> Jing Xiao,<sup>1</sup> and Daoguo Yang<sup>1</sup>

<sup>1</sup>Electromechanical Engineering College, Guilin University of Electronic Technology, No. 1 Jinji Road, Guilin, Guangxi 541004, China

<sup>2</sup>Guangxi Experiment Center of Information Science, No. 1 Jinji Road, Guilin, Guangxi 541004, China

Correspondence should be addressed to Daoguo Yang; [daoguo\\_yang@vip.163.com](mailto:daoguo_yang@vip.163.com)

Received 2 May 2016; Accepted 30 June 2016

Academic Editor: Yalin Dong

Copyright © 2016 Ping Zhang et al. This is an open access article distributed under the Creative Commons Attribution License, which permits unrestricted use, distribution, and reproduction in any medium, provided the original work is properly cited.

This paper describes the preparation of low-temperature sintered nanosilver paste with inverse microemulsion method with Span-80/Triton X-100 as the mixed-surfactant and analyzes the influence of different sintering parameters (temperature, pressure) on the shear properties of low-temperature sintering of nanosilver. Experimental results show that the shear strength of the low-temperature sintering of nanosilver increases as the temperature and pressure increase. But there are many pores and relative fewer cracks on the sintering layer after low-temperature sintered. The test thermal resistance of low-temperature sintered nanosilver paste is 0.795 K/W which is greater than SAC305 weld layer with a T3ster thermal analyzer. The adhesive performance and the heat dispersion of low-temperature sintered nanosilver paste need to be further researched and improved.

## 1. Introduction

In recent years, with the development of semiconductor technology, power electronic devices, and the lead-free materials, especially the emergence of wide-band gap semiconductor materials, packaging technology and interconnect materials face new challenges. For example, Silicon Carbide (SiC) and Gallium Nitride (GaN), with high breakdown electric field, high thermal conductivity, and excellent ability of radiation resistance, can operate normally in theory at high temperature up to 600°C, but the traditional interconnect materials cannot meet the requirements of high temperature condition [1–3]. Due to the low cost, good wettability, and good mechanical properties, lead-tin solder has been widely used in high heat-flow density power devices [4]. However, the lead will harm more systems, including nerves, hematopoietic system, and internal secretion system, and result in cognitive ability decline when it enters the body. Solder alloy tends to have the disadvantage of low reliability at a high temperature. Besides, the chip is easy to fail due to the mismatch of the thermal expansion coefficient because of large thermal stress of solder alloy [5]. Conducting resin has lower thermal conductivity and is usually

10~25 W/m·K with lower glass inversion temperature  $T_g$ . During the operation, the resin matrix of the conducting resin will gradually show fatigue failure and make the thermal resistance increase, which is extremely unfavorable to the heat dissipation and physical properties of the chip and severely limits the development in the high-power density devices [6, 7]. Silver glass solder paste, as an alternative to lead-free interconnection between the chip and substrates, has high thermal conductivity and electric conductivity after sintering [8]. However, its sintering temperature is up to 600°C or even higher temperature. Besides, some processes also need pressure, which threatens the integrity and reliability of the chip and easily leads to device failure. Due to the fatal defects, it is difficult for the traditional interconnection materials to meet the development needs of high-power devices.

Compared with traditional interconnect materials, the functional phase of low-temperature sintered nanosilver paste is silver which has excellent electrical conductivity, thermal conductivity, and higher melting point (melting temperature of bulk silver is 960°C) [9, 10]; what is more, the low-temperature sintered nanosilver paste can be sintered under low temperature. All these superior performances make it widely concerned as new interconnection materials,

especially used in high temperature, high-power, and high heat dissipation field and wide-band gap semiconductor equipment [11, 12].

This work describes the preparation of low-temperature sintered nanosilver paste with inverse microemulsion method with Span-80/Triton X-100 as the mixed-surfactant and analyzes the situation of inner of the shear layer after being sintered. Low-temperature sintered nanosilver paste is attempted to interconnect large-power Light-Emitting Diode (LED) and substrates. A T3ster thermal analyzer is used to test the thermal resistance of the sintering layer of low-temperature sintered nanosilver paste, and a contrast test is made with the common SAC305 solder paste.

## 2. Materials and Methods

Nanosilver paste is prepared with inverse microemulsion method with Span-80/Triton X-100 as the mixed-surfactant. First, mix Span 80, Triton X-100, n-hexyl alcohol, and normal heptane in proportion, stir the mixed solution at 30°C and low speed, drop 0.5 mol/mL silver nitrate solution to prepare transparent yellow silver nitrate inverse microemulsion system, and then drop 0.1 mol/mL hydrazine hydrate to prepare the inverse microemulsion containing silver nanoparticles. Finally, drop a certain amount of absolute ethyl alcohol to prepare low-temperature sintered nanosilver paste through cleaning and centrifugal deposition by centrifuge. Conduct thermogravimetric (TG) curve analysis and observe the distribution of nanosilver particles through scanning electron microscopy (SEM).

Nickel plating gold direct bonded copper (DBC) substrate is used as the substrate for shear strength test. In order to simplify the experiment, nickel plating gold DBC substrate of the same material is used as the analog chip. The sizes of the substrate and the analog chip are 5 mm × 6 mm and 3 mm × 3 mm, respectively. Low-temperature sintered nanosilver paste is coated by halftone printing with the printing thickness of 150 μm. Before coating, clean the substrate and the analog chip with anhydrous ethanol and distilled water to reduce the influence of impurities on the surfaces of substrate and analog chip and conduct three groups of shear test to the sintered samples, that is, 200°C sintering, 200°C low-pressure sintering, and 450°C sintering.

When conducting analysis to the thermal performance of low-temperature sintered nanosilver paste. Low-temperature sintered nanosilver paste is used for the connection between large-power LED chip and printed circuit board (PCB) substrate. The T3ster thermal analyzer is used to test the thermal resistance of the sintering layer of low-temperature sintered nanosilver paste, and a contrast test is made with the common SAC305 solder paste.

## 3. Results and Discussion

**3.1. TG Curve and SEM Analysis of Low-Temperature Sintered Nanosilver Paste.** Figure 1 shows TG curve analysis chart of low-temperature sintered nanosilver paste prepared through settlement after being cleaned with absolute ethyl alcohol,

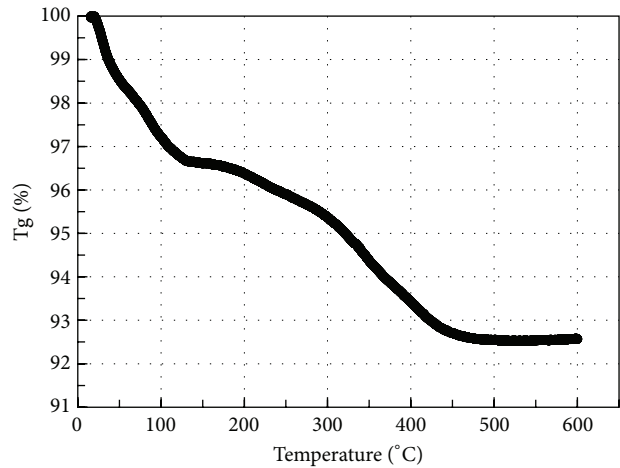


FIGURE 1: The TG curve of nanosilver paste.

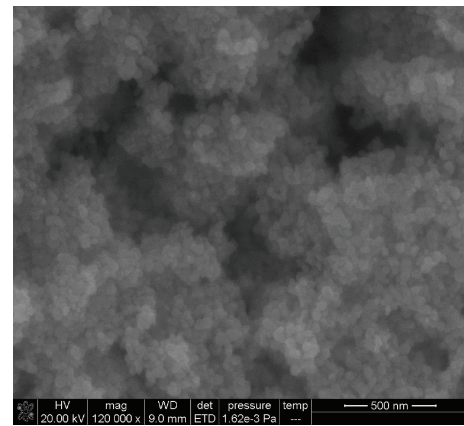


FIGURE 2: The SEM of nanosilver paste.

which analyzes the content of the components in low-temperature sintered nanosilver paste and its decomposition temperature. We can learn from the figure that content of functional phase nanosilver particles in low-temperature sintered nanosilver paste is 92.57%. TG curve can be divided into several stages below: ambient temperature 80°C, the curve declining sharply due to the volatilization of absolute ethyl alcohol; 80°C–130°C, the volatilization of normal heptane and n-hexyl alcohol; 130°C–450°C, the curve declining slowly at the beginning and declining sharply when the temperature reaches 300°C mainly due to the decomposition and volatilization of Span 80 and Triton X-100 (the total content of Span 80 and Triton X-100 accounts for 4.1% of the total mass); and 450°C and above, the curve tending to be smooth because the dispersing agent and diluent used are nonionic organics. When the sintering temperature reaches 450°C, the impurities can be negligible, and the agglomerate can be thought to be elemental silver and a small amount of silver oxide oxidized in the sintering process.

Figure 2 shows the particle size and morphology of as-prepared nanosilver particles after cleaning and vacuum drying observed with SEM. The drying temperature is about

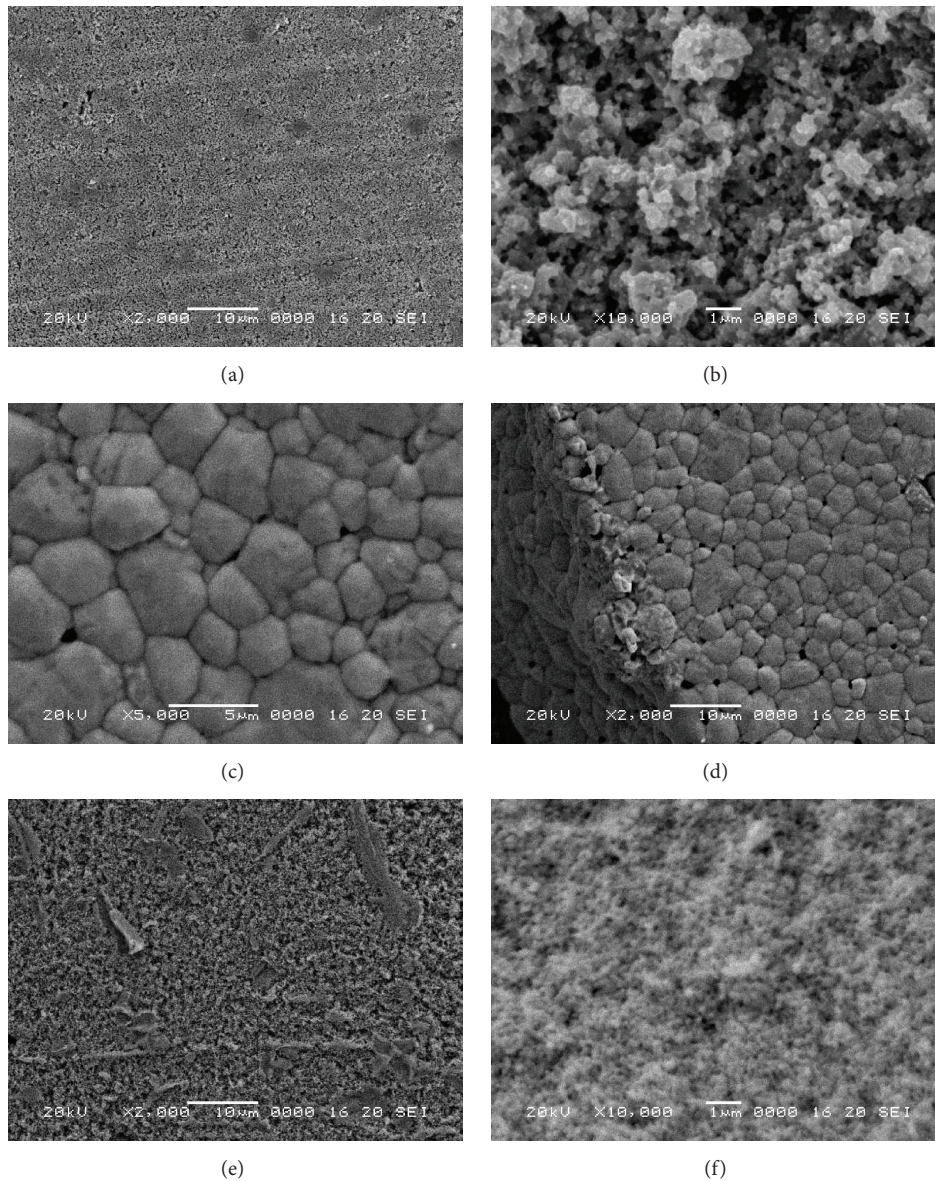


FIGURE 3: SEM images of interface microstructure of joints with different sintering temperatures and sintering pressure: 200°C sintering (a and b); 200°C low-pressure sintering (c and d); and 450°C sintering (e and f).

40°C. The nanosilver particles prepared by this method have uniform spherical particles, the distribution of nanosilver particle size is in the range of 30–60 nm, and the average diameter of nanosilver particle size is about 40 nm. The particle size of the nanosilver particles prepared in the method is larger may be because that the quantity of inverse microemulsion micelles is relatively small, and the nanosilver particles nucleate in the micelles and continue to grow due to limited quantity of inverse microemulsion micelles.

**3.2. The Shear Performance of Low-Temperature Sintered Nanosilver Paste.** When conducting shear test to 200°C sintered samples, the property of bonding between the low-temperature sintered nanosilver paste and the substrate is reduced due to larger surface roughness of substrate and

larger number of times of cleaning with absolute ethyl alcohol, making the maximum shear strength reach 12.25 MPa by homemade shear model. Figure 3(a) shows the surface topography of the structure that low-temperature sintered nanosilver paste is agglutinated with the analog chip. There are many macropores and small black spots on the surface. It is mainly due to the presence of residual organic compounds in the paste. Figure 3(b) shows the structure and morphology of the inner shear off layer of the 200°C sintering layer. The morphology analysis of the broken crack is where the low-temperature sintered nanosilver paste is sintered uniformly. However, there are many mesopores.

When the temperature is 200°C and the pressure is 1.11 MPa, the maximum shear strength of low-temperature sintered nanosilver paste can reach 18.7 MPa, which is larger

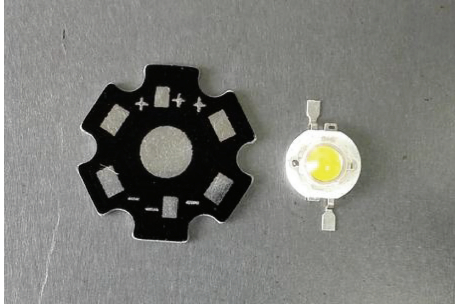


FIGURE 4: Large-power LED lamps and substrate.

than when there is no pressure. Figure 3(c) shows the morphology of the shear surface of low-temperature sintered nanosilver paste when the temperature is 200°C and the pressure is 1.11 MPa. The functional phase has a compact structure under the pressure. The sintered nanosilver particles are larger and uniform. Figure 3(d) shows the morphology of the shear fracture of low-temperature sintered nanosilver paste when the temperature is 200°C and the pressure is 1.11 MPa. The fracture structure has the same surface structure with the shear structure. The silver nanoparticles grow uniformly and are very compact.

The maximum shear strength of low-temperature sintered nanosilver paste can reach 27.36 MPa when the temperature is 450°C. Figure 3(e) shows the fractured surface topography of the sintering shearing interface at the temperature of 450°C. There are layers of thin sheets. The morphology is different from that when black stripes and spots appear during sintering at the temperature of 200°C. These sheets may be mainly the shedding layer of the surface of the analog chip, which ultimately leads to the decrease of shear strength. Figure 3(f) shows the sintering fracture structure of low-temperature sintered nanosilver paste at the temperature of 450°C. The inner fracture structure of the sintered layer has few cracks and mesopores. Functional phase of low-temperature sintered nanosilver particles sintered at the low temperature grow and connect tightly.

**3.3. The Thermal Performance of Low-Temperature Sintered Nanosilver Paste.** When conducting analysis to the thermal performance of low-temperature sintered nanosilver paste, the rated power of high-power LED is 3 W, and the input current is 650 mA, as shown in Figure 4. Number I LED lamps are represented as low-temperature sintered nanosilver paste interconnecting large-power LED lamps and the substrate, and number II LED lamps are represented as SAC305 interconnecting large-power LED lamps and the substrate. The sintering temperature for interconnection of number I LED lamps is 200°C, and the welding temperature for interconnection of number II LED lamps is 210°C. T3Ster equipment is used to analyze the coefficient of  $K$  and the thermal resistance of the two types of LED lamp samples. The results show that the optical power of SAC305 at the working current of 650 mA is 0.3932 W, and the coefficient of  $K$  is  $-2.152 \text{ mV}/^\circ\text{C}$ , the optical power of low-temperature

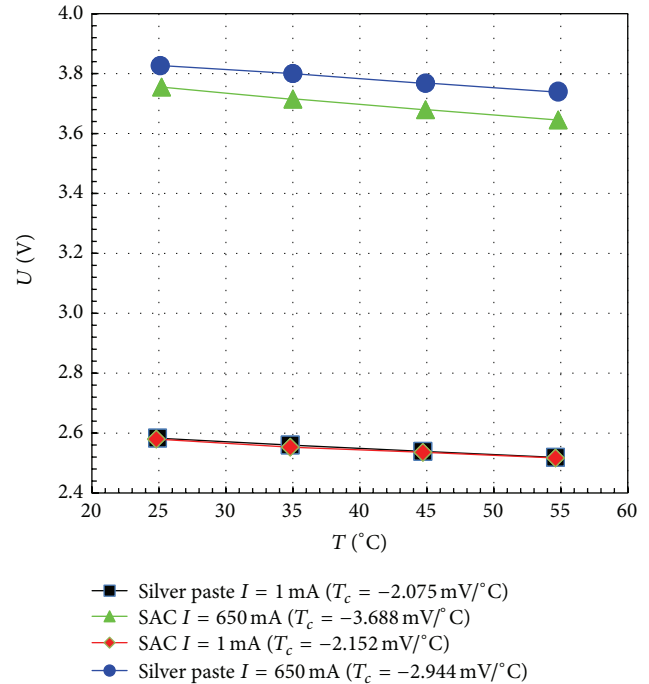


FIGURE 5: The coefficient  $K$  curve of nanosilver paste and SAC305.

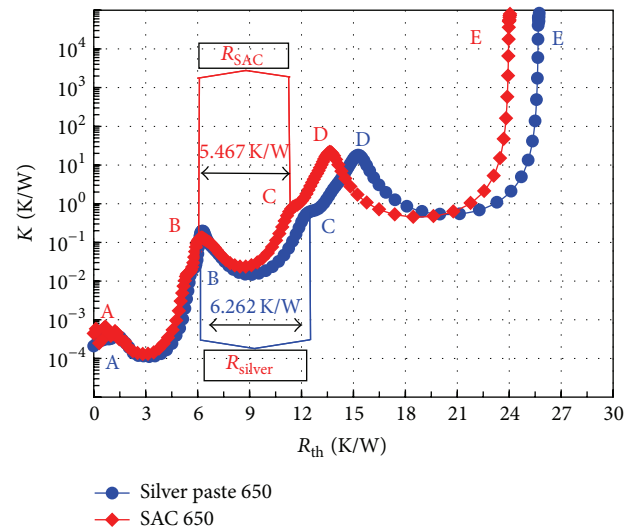


FIGURE 6: The comparison diagram of differential structure curves of number I LED lamps and number II LED lamps.

sintered nanosilver paste at the working current of 650 mA is 0.3932 W, and the coefficient of  $K$  is  $-2.075 \text{ mV}/^\circ\text{C}$ , the coefficient  $K$  curve as shown in Figure 5. We can see from the figures that coefficient  $K$  of the two samples changes not so much, also it shows that the LED chip has stable quality.

Figure 6 is the comparison diagram of differential structure functions of number I LED lamps and number II LED lamps. As shown in the figure, in both of these functions the local peaks and valleys indicate reaching new materials or changed surface areas in the heat-flow path. Peaks correspond

to regions of high thermal conductivity and valleys show region of low thermal conductivity, we can see that the thermal resistance of the low-temperature sintered nanosilver paste is 6.262 K/W, and the thermal resistance of SAC305 is 5.467 K/W. The thermal resistance of low-temperature sintered nanosilver paste is 0.795 K/W larger than that of SAC305. The junction temperature of the two types of LED lamps is obtained by processing the temperature change curves with software, which are 79.38°C and 75.34°C for number I and number II LED lamps. Because the thermal resistance of the low-temperature sintered nanosilver paste after sintering is greater than that of SAC305, causing that the junction temperature of number I LED lamps is larger than that of number II LED lamps. It also shows that the thermal performance after sintering of low-temperature sintered nanosilver paste used in this kind of LED lamp is worse than that used in SAC305. This is because the larger surface roughness of large-power LED heat dissipation block and PCB substrates and poor adhesive performance cause more pores on the sintering layer and larger interface resistance [13]; on the one hand, high-power LED heat dissipation block is made of aluminum which is easy to be oxidized, and the diffusion of silver atoms is worse on the aluminum surface than on the gold surface [14]. And SAC305 has good wettability and adhesive performance on aluminum block and PCB substrates, greatly reducing the thermal resistance of the interface.

#### 4. Conclusions

- (1) Low-temperature sintered nanosilver paste is prepared with inverse microemulsion method with Span-80/Triton X-100 as the mixed-surfactant. The shear strength of the low-temperature sintering of nanosilver under low pressure is higher, the pore is smaller, and the particles after sintering are larger and the arrangement is compact. However, there are more cracks.
- (2) The surface of the heat dissipation block and PCB is rougher, and the surface material is nonsilver material, which affects the diffusion of silver atoms during the sintering of low-temperature sintered nanosilver paste and results in poor adhesive performance. Finally, the test thermal resistance of low-temperature sintered nanosilver paste is 0.795 K/W higher than that of SAC305 in the application.
- (3) Adding functional phase materials, such as copper and graphite in low-temperature sintered nanosilver paste, may effectively improve the adhesive performance and the heat dispersion, which needs further research and improvement.

#### Competing Interests

The authors declare that there is no conflict of interests regarding the publication of this paper.

#### Acknowledgments

The authors acknowledge the financial support provided by supported by National Natural Science Foundation of China (Project no. 51506033), Guangxi University of Science and Technology Research Projects (Grant no. KY2015ZD045), Innovation Project of GUET Graduate Education (Grant no. 2016YJCX18), and Guangxi's Key Laboratory Foundation of Manufacturing Systems and Advanced Manufacturing Technology (Grant no. 15-140-30-005Z).

#### References

- [1] J. Hornberger, A. B. Lostetter, K. J. Olejniczak, T. McNutt, S. M. Lal, and A. Mantooth, "Silicon-carbide (SiC) semiconductor power electronics for extreme high-temperature environments," in *Proceedings of the IEEE Aerospace Conference Proceedings*, pp. 2538–2555, Big Sky, Mont, USA, March 2004.
- [2] T. Nomura, M. Masuda, N. Ikeda, and S. Yoshida, "Switching characteristics of GaN HFETs in a half bridge package for high temperature applications," *IEEE Transactions on Power Electronics*, vol. 23, no. 2, pp. 692–697, 2008.
- [3] R. Khazaka, B. Thollin, L. Mendizabal, D. Henry, R. Khazaka, and R. Hanna, "Characterization of nanosilver dry films for high-temperature applications," *IEEE Transactions on Device and Materials Reliability*, vol. 15, no. 2, pp. 149–155, 2015.
- [4] L. R. Garcia, W. R. Osório, L. C. Peixoto, and A. Garcia, "Mechanical properties of Sn–Zn lead-free solder alloys based on the microstructure array," *Materials Characterization*, vol. 61, no. 2, pp. 212–220, 2010.
- [5] C.-J. Chen, C.-M. Chen, R.-H. Horng, D.-S. Wu, and J.-S. Hong, "Thermal management and interfacial properties in high-power GaN-based light-emitting diodes employing diamond-added Sn-3 wt.%Ag-0.5 wt.% Cu solder as a die-attach material," *Journal of Electronic Materials*, vol. 39, no. 12, pp. 2618–2626, 2010.
- [6] P. Hu, W. O'Neil, and Q. Hu, "Synthesis of 10 nm Ag nanoparticle polymer composite pastes for low temperature production of high conductivity films," *Applied Surface Science*, vol. 257, no. 3, pp. 680–685, 2010.
- [7] W. Tao, S. Chen, P. Berggren, and J. Liu, "Reliability study for high temperature stable conductive adhesives," in *Proceedings of the International Symposium on Advanced Packaging Materials: Microtech (APM '10)*, pp. 74–77, IEEE, Cambridge, UK, March 2010.
- [8] R. Kisiel, Z. Szczepański, M. Sochacki et al., "Thermal properties of SiC-ceramics substrate interface made by silver glass composition," in *Proceedings of the 34th International Spring Seminar on Electronics Technology (ISSE '11)*, pp. 98–102, IEEE, Trstanska Lomnica, Slovakia, May 2011.
- [9] W. Guo, Z. Zeng, X. Zhang, P. Peng, and S. Tang, "Low-temperature sintering bonding using silver nanoparticle paste for electronics packaging," *Journal of Nanomaterials*, vol. 2015, Article ID 897142, 7 pages, 2015.
- [10] P. Peng, A. Hu, A. P. Gerlich, G. Zou, L. Liu, and Y. N. Zhou, "Joining of silver nanomaterials at low temperatures: processes, properties, and applications," *ACS Applied Materials & Interfaces*, vol. 7, no. 23, pp. 12597–12618, 2015.
- [11] P. Ning, T. G. Lei, F. Wang, G.-Q. Lu, K. D. T. Ngo, and K. Rajashekhara, "A novel high-temperature planar package for SiC multichip phase-leg power module," *IEEE Transactions on Power Electronics*, vol. 25, no. 8, pp. 2059–2067, 2010.

- [12] R. Khazaka, L. Mendizabal, and D. Henry, "Review on joint shear strength of nano-silver paste and its long-term high temperature reliability," *Journal of Electronic Materials*, vol. 43, no. 7, pp. 2459–2466, 2014.
- [13] L. Jiang, T. G. Lei, K. D. T. Ngo, G.-Q. Lu, and S. Luo, "Evaluation of thermal cycling reliability of sintered nanosilver versus soldered joints by curvature measurement," *IEEE Transactions on Components, Packaging and Manufacturing Technology*, vol. 4, no. 5, pp. 751–761, 2014.
- [14] E. Ide, S. Angata, A. Hirose, and K. F. Kobayashi, "Bonding of various metals using Ag metallo-organic nanoparticles—a novel bonding process using Ag metallo-organic nanoparticles," in *Materials Science Forum*, pp. 383–388, Trans Tech Publications, 2006.

## Research Article

# Nonlinear Absorptions of CdSeTe Quantum Dots under Ultrafast Laser Radiation

Zhijun Chai, Yachen Gao, Degui Kong, and Wenzhi Wu

*School of Electronic Engineering, Heilongjiang University, Harbin 150080, China*

Correspondence should be addressed to Yachen Gao; [gaoyachen@hlju.edu.cn](mailto:gaoyachen@hlju.edu.cn) and Wenzhi Wu; [wuwenzhi@hlju.edu.cn](mailto:wuwenzhi@hlju.edu.cn)

Received 7 May 2016; Accepted 20 June 2016

Academic Editor: Yan Wang

Copyright © 2016 Zhijun Chai et al. This is an open access article distributed under the Creative Commons Attribution License, which permits unrestricted use, distribution, and reproduction in any medium, provided the original work is properly cited.

The oil-soluble alloyed CdSeTe quantum dots (QDs) are prepared by the electrostatic method. The basic properties of synthesized CdSeTe QDs are characterized by UV-Vis absorption spectroscopy, photoluminescence spectroscopy, inductively coupled plasma mass spectrometry, and transmission electron microscope. The off-resonant nonlinear optical properties of CdSeTe QDs are studied by femtosecond Z-scan at 1 kHz (low-repetition rate) and 84 MHz (high-repetition rate). Nonlinear absorption coefficients are calculated under different femtosecond laser excitations. Due to the long luminescent lifetime of CdSeTe QDs, under the conditions of high-repetition rate, for open-aperture curve, heat accumulation and bleaching of ground state are responsible for the decrease of two-photon absorption (TPA) coefficient.

## 1. Introduction

Quantum dots (QDs) provide a feasible alternative for electroluminescence light-emitting diode and fluorescence imaging because of their unique photophysical characteristics, such as size tunable photoluminescence (PL) spectrum, high quantum yields, broad absorption, and narrow emission wavelengths [1]. When the nanoparticles are excited by ultrafast laser pulse, nonlinear absorption, luminescence, coherent phonon vibration, and plastic deformation [2] can be predicted and observed. The study of nonlinear optical properties for nanoparticles using Z-scan techniques provides complementary information to extend the potential application to optical switching and information storage [3, 4]. This nonlinear optical information can help to understand deeply fundamental properties of nanomaterials including but not limited to linear optical properties. Many experiments as well as theoretical calculations were carried out to investigate the nonlinear optical properties of II-VI QDs, including CdTe [5], CdSe [6], and CdS [7] QDs. Recently alloyed II-VI QDs have been extensively synthesized since their band gap can be tuned without the change of nanoparticle size. Through changing the composition of QDs' element, the band gap can be expanded from ultraviolet to near infrared range, so the nonlinear optical properties are important

for the further investigation to alloyed QDs. Now Z-scan measurements have performed on some kinds of alloyed QDs, such as CdSeS/polystyrene film [8], CdSeS/ZnS [9], and CuInS<sub>2</sub> QDs [10], due to their unique optoelectronic properties.

Nonlinear absorption, especially TPA, of semiconductor QDs is of current interest toward applications such as nonlinear optical gain media [11], optical limiting [12], or biological labeling/imaging [13]. The higher the cross section per particle or volume, the lower the excitation intensities needed to obtain a high enough response in TPA applications with the same amount of material [14]. II-VI semiconductor-based QDs offer significantly higher TPA cross sections with respect to the particle volume.

In this work we investigated nonlinear absorption of CdSeTe QDs in toluene using femtosecond Z-scan technique at 800 nm. CdSeTe QDs are one kind of alloy II-VI semiconductor QDs, which can change the band gap through the change of the molar ratio of Selenium (Se) and Tellurium (Te). The open-aperture Z-scan behaviors of the samples are investigated based on the local nonlinear responses including TPA. The results obtained from the experimental Z-scan measurements are compared with the influence of repetition rate. With pump-power intensity increasing, TPA is investigated using classical theoretical formula [15]. Finally,

the origin of nonlinear absorption for CdSeTe QDs is briefly discussed.

## 2. Experimental Approach

**2.1. Synthesis.** CdSeTe QDs are prepared by injecting of cadmium oxide, oleic acid, Selenium powder, Tellurium powder, trioctylphosphine (TOP), and octadecene into the flask with three necks. Mixed solution keeps on a period of one hour for this solution is cooled to room temperature; then the reaction temperature increases at a rate of  $10^{\circ}\text{C}$  per minute to  $180\sim 260^{\circ}\text{C}$ . The detailed preparation method was similar to the description in [16, 17]. Samples of colloidal CdSeTe QDs passivated with organic ligands (octadecene and trioctylphosphine). The organic capping groups sterically stabilize the dots in toluene. Optically thin and transparent, close-packed QDs are deposited on carbon-coated copper grids. High-resolution transmission electron microscope (TEM) measurement is performed on a Tecnai G220 S-Twin microscope operating at a high voltage at 200 kV.

**2.2. Experimental Setup.** The Z-scan measurements with low-repetition rate are carried out with femtosecond laser pulses (Coherent, Legend) operating at 800 nm at a repetition rate of 1 kHz to avoid thermal accumulation. The Z-scan measurements with high-repetition rate are performed with seed laser (Spectra Physics, Mai Tai) operating at 800 nm at a repetition rate of 84 MHz as shown in Figure 1. In the Z-scan technique, a sample of thickness  $L$  is translated through the focus of a beam with a Gaussian spatial profile, and the transmission through an aperture behind the sample is measured as a function of the longitudinal coordinate  $Z$ . The linear transmittance of the solution is adjusted to be 50% at 800 nm by adding toluene to CdSeTe QDs solution. The incident and transmitted laser powers are monitored as the samples are moving along the propagation direction of the laser pulses. The laser pulses are focused onto a 2 mm thick quartz cuvette, which contained the CdSeTe QDs solution, with a planoconvex lens (focal length of 200 mm). The Gaussian laser beam waist  $\omega_0$  is measured to be  $80\ \mu\text{m}$  after focusing with the scanning knife-edge technique. The open-aperture Z-scan signals are detected with Silicon detector (Thorlabs, Det36A) and collected by the computer through a lock-in amplifier (EG&G, Model 5210). In order to testify the validity of femtosecond Z-scan experiment, the measurement of carbon sulfide is performed. The nonlinear absorption coefficients of carbon sulfide at femtosecond laser excitation are  $\beta = 1.5 \times 10^{-2}\ \text{cm/GW}$  at power density of  $I_0 = 31\ \text{GW/cm}^2$ , which is reasonably consistent with the reported results in [18].

## 3. Results and Discussion

**3.1. Optical and Structural Characterization.** The band gap for bulk CdSe is around 712 nm (1.74 eV) at room temperature, and the band gap for bulk CdTe is 827 nm (1.50 eV) [19]. When the size of them is reduced to several nanometers, the band gaps of II-VI semiconductors shift to higher energy due to quantum size confinement, causing a blue shift of the

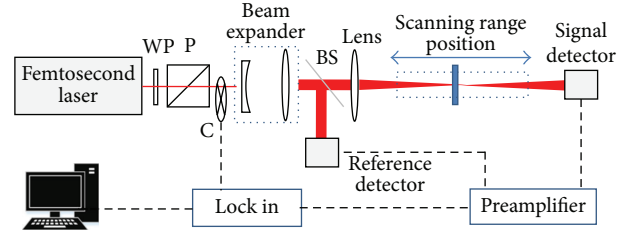


FIGURE 1: Schematic diagram of Z-scan setup using femtosecond seed laser as excitation source (high-repetition rate). WP is a half-wave plate, P is a polarizer, C is a chopper, and BS is a beam splitter.

adsorption spectrum. Figure 2(a) shows the UV-absorption and PL spectra of the CdSeTe QDs spectra, which reveals that the size of the nanoparticles is nearly monodispersed represented by the sharp absorption and emission peaks (FWHM  $\sim 57\ \text{nm}$ ). The absorption peak can be assigned to excitonic transitions between the lowest electron state ( $1S_{1/2}$ ) and hole states ( $1S_{3/2}$ ). The molar ratio of Se and Te in CdSeTe QDs measured is 3:1 using inductively coupled plasma mass spectrometry (ICP-MS). The CdSeTe QDs in Figure 2(b) are basically spherical, sufficiently monodisperse, and well separated, with the average sizes distribution of 3.5 nm from the observation of TEM image.

**3.2. Nonlinear Absorption at Low-Repetition Rate.** In the transparent spectral region, the off-resonant nonlinear absorption coefficient can be ascribed multiphoton absorption, free carrier absorption, bleaching, and so on. For the sample, the first absorption peak of nanomaterial usually corresponds to the band gap energy  $E_g$ , where  $E_g$  is the band gap energy of samples. Nonlinear absorption mainly results from TPA and free carrier absorption in semiconductor materials. Due to the fact that the femtosecond excitation condition of CdSeTe QDs satisfies ( $E_g = 2.2\ \text{eV}$ ), TPA can take place. However, the contribution of excitonic emission to the nonlinearity cannot be neglected. Off-resonant optical nonlinearity of a series of CdSe nanocrystallite-doped glasses with CdSe particle radii from 3.5 to 6.5 nm is measured using Nd:YAG pulsed laser as excitation source [20]. The bound electron nonlinearity of nanometer-sized CdSe is negative and reflects the dominant role of the free carrier absorption which is different from the bulk semiconductors. Therefore, nonlinear optical properties of CdSeTe QDs should also come mainly from the contribution of the quantum confinement. Here, open-aperture Z-scan curves are shown in Figure 3, which reveals TPA occurs when photon energy of laser radiation is smaller than  $E_g$ , nonlinear absorption coefficient of CdSeTe QDs is measured to be about  $3.1 \times 10^{-2}\ \text{cm/GW}$  under the pump-power intensity from 70 to  $175\ \text{GW/cm}^2$ , and it is ascribed to TPA because the heat accumulation is highly depressed by employing femtosecond laser pulses with very low-repetition rate [21, 22].

**3.3. Upconversion Luminescent Dynamics at Low-Repetition Rate.** Luminescent decay dynamics provides additional major information on photoinduced carriers in CdSeTe

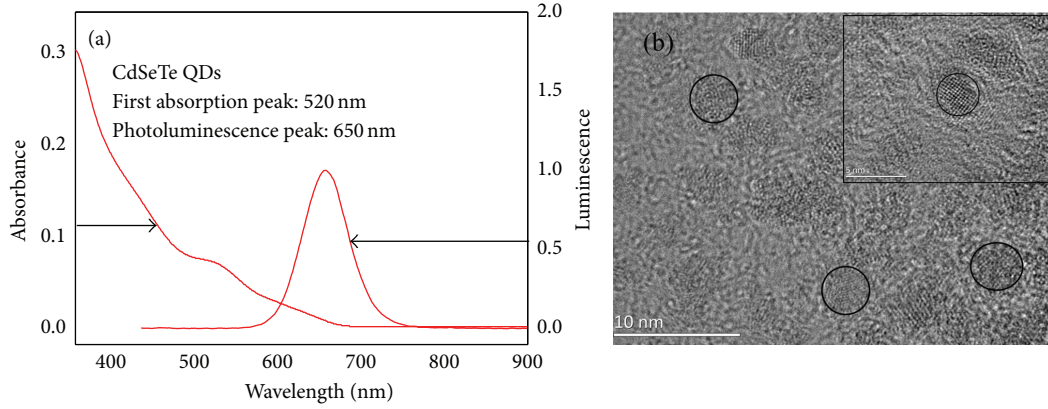


FIGURE 2: (a) UV-Vis and PL spectra of CdSeTe QDs samples. (b) TEM image of red-emitting alloyed CdSeTe QDs, where the average size is 3.5 nm. Inset: a high-resolution image displays clear crystal lattice from one of QDs.

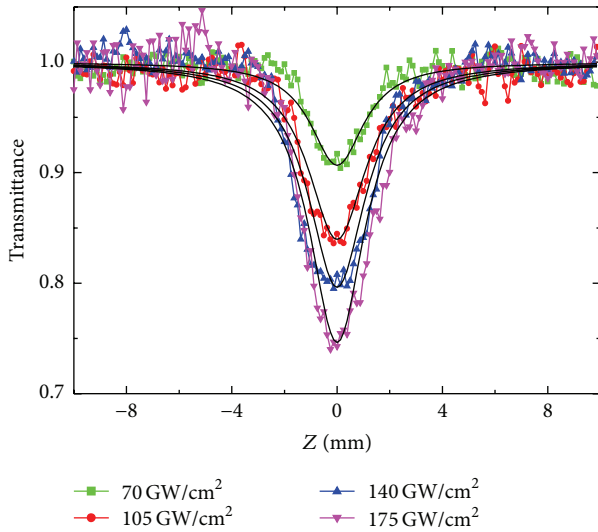


FIGURE 3: Open-aperture Z-scan curves for CdSeTe QD at 800 nm femtosecond excitation.

QDs. Upconversion luminescence of CdSeTe QDs is easily observed at 800 nm femtosecond laser excitation. A defect-related or trapping state is commonly observed in II-VI semiconductor QDs [23]. A broad emission band [24] has been reported and has been attributed to trapping states or surface states. Upconversion luminescence largely ascribes to TPA in nature through a virtual or real intermediate state. Upconversion luminescence decay is not monoexponential and consists of multiple exponential components. The biexponential fitting with convolution strongly implies the involvement of two different states in this upconversion luminescence process [25].

The average PL lifetime values are estimated using the following equation [26]:

$$\tau_{av} = \frac{a_1\tau_1 + a_2\tau_2}{a_1 + a_2}, \quad (1)$$

where  $\tau_{av}$  is the average lifetime, which is used to describe recombination rate of charge carrier for CdSeTe QDs in terms

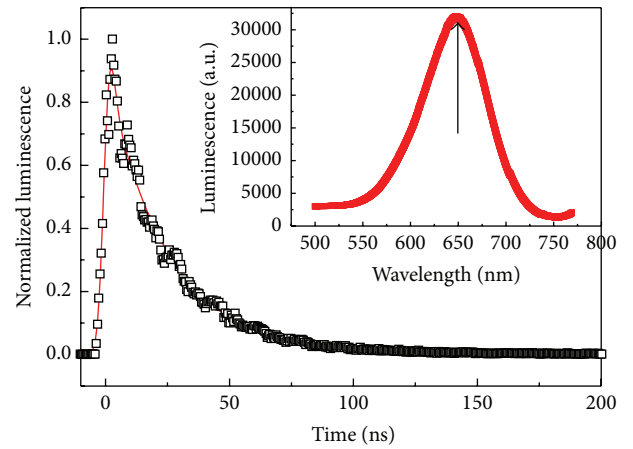


FIGURE 4: Nanosecond luminescent dynamics at the wavelength of the peak at 650 nm.

of a variation in the luminescence decay rates caused by excitonic and trapping states [27]. The average lifetime of CdSeTe QDs is 23.3 ns as shown in Figure 4.

**3.4. Nonlinear Absorption at High-Repetition Rate.** In order to investigate the nonlinear absorption properties, the excitation laser source has been changed as seed laser with high-repetition rate. For high-repetition rate lasers as excitation source, the effects of heat accumulation following the passage of one laser pulse linger for several characteristic thermal time constants. As a result, the thermal effect will increase whenever the time interval between incident laser pulses is much shorter than the characteristic thermal time constant until a steady state is reached between the rates of heat generation and heat diffusion. The repetition rate of the excitation laser source is 84 MHz, so the time interval between two pulses is 11.9 ns. As well as we know, alloyed CdSeTe QDs is a typical luminescent nanomaterial. Here the average luminescence lifetime of QDs sample used is about 23.3 ns, so the first laser pulse is used to excite the luminescence of CdSeTe QDs; a variety of carriers are still on the excited state

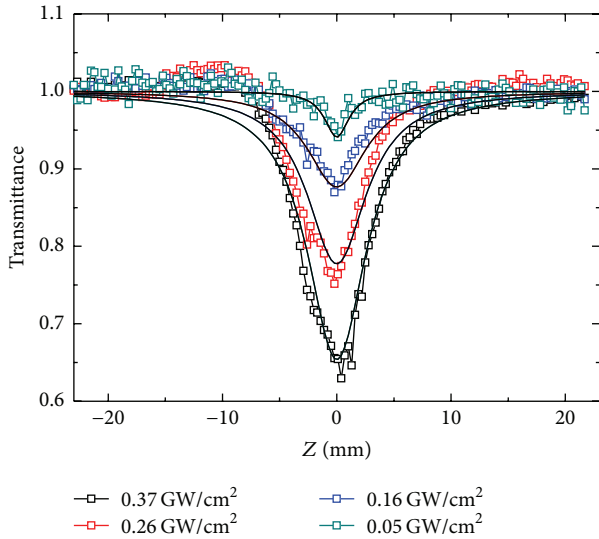


FIGURE 5: Open-aperture Z-scan curves for CdSeTe QDs at 800 nm femtosecond excitation.

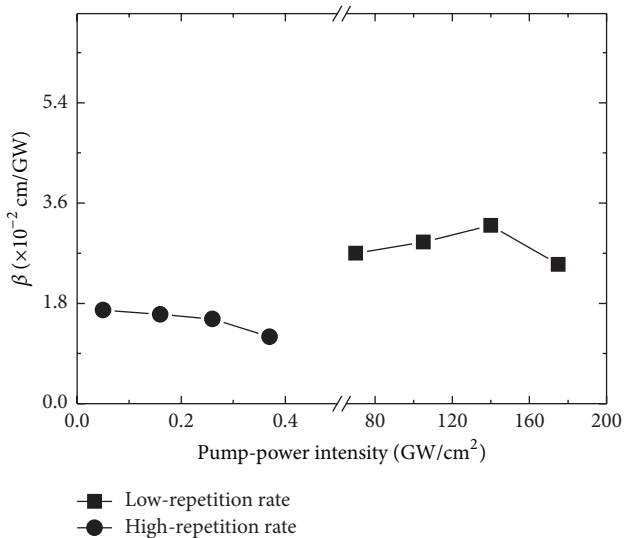


FIGURE 6: TPA coefficient as a function of pump-power intensity of the CdSeTe QDs in toluene.

and not yet back to ground state when the second laser is coming. Open-aperture Z-scan curves under different pump-power intensities are shown in Figure 5. The normalized transmittance for the open-aperture condition is calculated from value of  $q_0(Z)$  and  $Z$  [28]. The values of TPA coefficient are calculated by the formula from [29]. Obviously TPA can be affected by the heat accumulation and bleaching of ground state.

**3.5. Comparison with the Influence of Repetition Rate.** The TPA coefficients of CdSeTe QDs calculated are shown in Figure 6. The values of TPA coefficients of CdSeTe QDs are about  $2.4 \times 10^{-2}$  cm/GW which are found to be four and two orders higher in CdSe nanoparticles, respectively, as

compared to the bulk CdSe direct and indirect band gap crystal and hence third-order nonlinear susceptibility enhanced in semiconductors QDs [30]. These results obtained are due to the crystalline nature and smaller size of particles. With the pump-power intensities increasing at high-repetition rate, TPA becomes a little smaller. Heat accumulation and the bleaching of ground state can affect the nonlinear absorption coefficient. Ignoring thermal effects in these types of experiments will lead to an erroneous interpretation of the origin and strength of the nonlinearity.

In short, the repetition-rate influence of nonlinear absorption properties for CdSeTe QDs is discussed through the classical theoretical formula. Under the high-repetition rate, heat accumulation due to the fast excitation and bleaching of ground state should be considered. The larger value of third nonlinear optical susceptibility makes them potential candidates for all-optical switching and nonlinear optical devices. Maybe, it is also necessary to consider the laser pump flux in the application of alloyed II-VI QDs to biological and medical imaging.

## 4. Conclusions

In summary, optical nonlinear properties of CdSeTe QDs in toluene are investigated by femtosecond Z-scan techniques at low- and high-repetition rate. The properties of TPA are discussed under the consideration of heat accumulation. With the pump intensity increasing, TPA appears and becomes smaller at high-repetition rate. Due to the long luminescent lifetime of CdSeTe QDs, under the conditions of high-repetition rate, for open-aperture curve, the bleaching of ground state and heat accumulation are responsible for the changes of TPA coefficient.

## Competing Interests

All the authors declare that there are no competing interests regarding the publication of this paper.

## Acknowledgments

This research was supported in partial finance by Science Fund of Heilongjiang University for Young Scholars (QL201211, JCL201205), Electronic Engineering Provincial Key Laboratory (P201404), Natural Science Foundation of China (61275117, 61204007), New-Century Training Program Foundation for the Talents by Heilongjiang Province (1254-NCET-018), Foundation for University Key Teacher by Heilongjiang University (1252G047), and Heilongjiang Province Postdoctoral Science Foundation (LBH-Q14139).

## References

- [1] C.-Y. Zhang and L. W. Johnson, "Quantum dot-based fluorescence resonance energy transfer with improved FRET efficiency in capillary flows," *Analytical Chemistry*, vol. 78, no. 15, pp. 5532–5537, 2006.
- [2] L. Cao and M. Koslowski, "Rate-limited plastic deformation in nanocrystalline Ni," *Journal of Applied Physics*, vol. 117, no. 24, Article ID 244301, 2015.

- [3] J. R. Heath, "The chemistry of size and order on the nanometer scale," *Science*, vol. 270, no. 5240, pp. 1315–1316, 1995.
- [4] P. Reiss, J. Bleuse, and A. Pron, "Highly luminescent CdSe/ZnSe core/shell nanocrystals of low size dispersion," *Nano Letters*, vol. 2, no. 7, pp. 781–784, 2002.
- [5] Q. H. Jin, W. Z. Wu, Z. R. Zheng et al., "The third-order optical nonlinearity and upconversion luminescence of CdTe quantum dots under femtosecond laser excitation," *Journal of Nanoparticle Research*, vol. 11, no. 3, pp. 665–670, 2009.
- [6] C. A. Leatherdale, W.-K. Woo, F. V. Mikulec, and M. G. Bawendi, "On the absorption cross section of CdSe nanocrystal quantum dots," *The Journal of Physical Chemistry B*, vol. 106, no. 31, pp. 7619–7622, 2002.
- [7] N. Venkatram, D. N. Rao, and M. A. Akundi, "Nonlinear absorption, scattering and optical limiting studies of CdS nanoparticles," *Optics Express*, vol. 13, no. 3, pp. 867–872, 2005.
- [8] X. Li, F. Li, and Z. He, "Large off-resonant and intensity-dependent third-order optical nonlinearities of CdSeS quantum dots/polystyrene composite film," *Materials Letters*, vol. 93, pp. 366–369, 2013.
- [9] F. Wu, W. Tian, W. Chen et al., "Optical nonlinearity and optical limiting of CdSeS/ZnS quantum dots," *Journal of Modern Optics*, vol. 56, no. 17, pp. 1868–1873, 2009.
- [10] N. Venkatram, S. K. Batabyal, L. Tian, J. J. Vittal, and W. Ji, "Shape-dependent nonlinear absorption and relaxation in CuInS<sub>2</sub> nanocrystals," *Applied Physics Letters*, vol. 95, no. 20, Article ID 201109, 2009.
- [11] B. Guzelturk, Y. Kelestemur, M. Olutas, S. Delikanli, and H. V. Demir, "Amplified spontaneous emission and lasing in colloidal nanoplatelets," *ACS Nano*, vol. 8, no. 7, pp. 6599–6605, 2014.
- [12] G. S. He, K.-T. Yong, Q. Zheng et al., "Multi-photon excitation properties of CdSe quantum dots solutions and optical limiting behavior in infrared range," *Optics Express*, vol. 15, no. 20, pp. 12818–12833, 2007.
- [13] F. Wang, D. Banerjee, Y. Liu, X. Chen, and X. Liu, "Upconversion nanoparticles in biological labeling, imaging, and therapy," *Analyst*, vol. 135, no. 8, pp. 1839–1854, 2010.
- [14] R. Scott, A. W. Achtstein, A. Prudnikau et al., "Two photon absorption in II-VI semiconductors: the influence of dimensionality and size," *Nano Letters*, vol. 15, no. 8, pp. 4985–4992, 2015.
- [15] M. Sheik-Bahae, A. A. Said, T.-H. Wei, D. J. Hagan, and E. W. Van Stryland, "Sensitive measurement of optical nonlinearities using a single beam," *IEEE Journal of Quantum Electronics*, vol. 26, no. 4, pp. 760–769, 1990.
- [16] R. E. Bailey and S. Nie, "Alloyed semiconductor quantum dots: tuning the optical properties without changing the particle size," *Journal of the American Chemical Society*, vol. 125, no. 23, pp. 7100–7106, 2003.
- [17] Z. Pan, K. Zhao, J. Wang, H. Zhang, Y. Feng, and X. Zhong, "Near infrared absorption of CdSe<sub>x</sub>Te<sub>1-x</sub> alloyed quantum dot sensitized solar cells with more than 6% efficiency and high stability," *ACS Nano*, vol. 7, no. 6, pp. 5215–5222, 2013.
- [18] S. Couris, M. Renard, O. Faucher et al., "An experimental investigation of the nonlinear refractive index ( $n_2$ ) of carbon disulfide and toluene by spectral shearing interferometry and z-scan techniques," *Chemical Physics Letters*, vol. 369, no. 3–4, pp. 318–324, 2003.
- [19] W. W. Yu, L. H. Qu, W. Z. Guo, and X. G. Peng, "Experimental determination of the extinction coefficient of CdTe, CdSe, and CdS nanocrystals," *Chemistry of Materials*, vol. 15, no. 14, pp. 2854–2860, 2003.
- [20] D. Cotter, M. G. Burt, and R. J. Manning, "Below-band-gap third-order optical nonlinearity of nanometer-size semiconductor crystallites," *Physical Review Letters*, vol. 68, no. 8, pp. 1200–1203, 1992.
- [21] K. Kamada, K. Matsunaga, A. Yoshino, and K. Ohta, "Two-photon-absorption-induced accumulated thermal effect on femtosecond Z-scan experiments studied with time-resolved thermal-lens spectrometry and its simulation," *Journal of the Optical Society of America B*, vol. 20, no. 3, pp. 529–537, 2003.
- [22] S. M. Mian, S. B. McGee, and N. Melikechi, "Experimental and theoretical investigation of thermal lensing effects in mode-locked femtosecond Z-scan experiments," *Optics Communications*, vol. 207, no. 1–6, pp. 339–345, 2002.
- [23] S. F. Wuister, F. Van Driel, and A. Meijerink, "Luminescence and growth of CdTe quantum dots and clusters," *Physical Chemistry Chemical Physics*, vol. 5, no. 6, pp. 1253–1258, 2003.
- [24] W. Chen, A. G. Joly, and D. E. Mccready, "Upconversion luminescence from CdSe nanoparticles," *Journal of Chemical Physics*, vol. 122, no. 22, Article ID 224708, 2005.
- [25] W. Z. Wu, Z. R. Zheng, J. P. Zhang et al., "Upconversion luminescence of CdTe nanocrystals by use of near-infrared femtosecond laser excitation," *Optics Letters*, vol. 32, no. 9, pp. 1174–1176, 2007.
- [26] W. Wu, Y. Gao, Q. Chang et al., "Upconversion luminescent characteristics and peak shift of CdSeS nanocrystals under different wavelength laser excitation," *Journal of Nanoparticle Research*, vol. 13, no. 3, pp. 1049–1061, 2011.
- [27] A. L. Rogach, T. Franzl, T. A. Klar et al., "Aqueous synthesis of thiol-capped CdTe nanocrystals: state-of-the-art," *The Journal of Physical Chemistry C*, vol. 111, no. 40, pp. 14628–14637, 2007.
- [28] M. Sharma and S. K. Tripathi, "Two photon absorption studies of PVA coated CdSe/ZnSe and CdSe/CdS core/shell nanostructures," *Chemical Physics Letters*, vol. 634, Article ID 33029, pp. 266–270, 2015.
- [29] G. Tsigaridas, I. Polyzos, P. Persephonis, and V. Giannetas, "A novel approach for analyzing open Z-scan experiments," *Optics Communications*, vol. 266, no. 1, pp. 284–289, 2006.
- [30] A. Gaur, D. K. Sharma, D. S. Ahlawat, and N. Singh, "Multiphoton photoconductivity and optical nonlinearities in ZnSe and CdSe direct band gap crystals," *Journal of Optics A: Pure and Applied Optics*, vol. 9, no. 3, pp. 260–264, 2007.

## Research Article

# Effect of Strain on Thermal Conductivity of Si Thin Films

Xingli Zhang<sup>1</sup> and Guoqiang Wu<sup>2</sup>

<sup>1</sup>College of Mechanical and Electrical Engineering, Northeast Forestry University, Harbin 150040, China

<sup>2</sup>The State Key Laboratory of Structural Analysis for Industrial Equipment, Dalian University of Technology, Dalian 116024, China

Correspondence should be addressed to Xingli Zhang; zhang-xingli@nefu.edu.cn

Received 1 March 2016; Revised 29 April 2016; Accepted 10 May 2016

Academic Editor: Yan Wang

Copyright © 2016 X. Zhang and G. Wu. This is an open access article distributed under the Creative Commons Attribution License, which permits unrestricted use, distribution, and reproduction in any medium, provided the original work is properly cited.

Nonequilibrium molecular dynamics (NEMD) simulations are employed to gain an understanding of the effect of strain on the thermal conductivity of Si thin films. The analysis shows that the strain has an appreciable influence on the thermal conductivity of Si thin films. The thermal conductivity decreases as the tensile strain increases and increases as the compressive strain increases. The decrease of the phonon velocities and surface reconstructions generated under strain could explain well the effects of strain on the thermal conductivity of Si thin films.

## 1. Introduction

The Si thin films have shown important applications in many fields, such as microelectronic, optoelectronic, and microelectromechanical devices. Understanding and predicting thermal transport of Si thin films at the nanoscale are essential for improving the performance and reliability of these devices. Because the characterized size is down to the nanoscale, the heat transfer of Si thin films becomes unusual as compared to bulk materials. Researchers can design nanomaterials with certain thermal properties through probing the factors which affect thermal properties, so the thermal conductivity of Si thin films depending on the size of the system and defects have been researched by Boltzmann transport equation (BTE) based approaches and molecular dynamics (MD) simulations [1–5].

Nanoscale devices, particularly thin films, usually contain residual strain after fabrication [6], which may considerably affect the thermal transport properties of the material. Many researchers have attempted to simulate the effect of strain on the thermal properties of material using different methods. Bhowmick and Shenoy [7] derived the relationship of thermal conductivity as a function of temperature and strain using the Peierls-Boltzmann formulation; Zhang et al. [8] investigated how the thermal conductivity responded to the external tensile strain by nonequilibrium molecular dynamics (NEMD) simulations on functionalized bilayer graphene sheet; Wang

and Shen [9] investigated the thermal properties of Ni/Al laminated structures using NEMD method; Xu and Li [10] presented a model that combined lattice dynamics and the phonon BTE to analyze strain effect on the cross-plane phonon thermal conductivity of silicon wire-germanium host nanocomposites. These studies have shown the significance of strain on the nanoscale thermal transport.

In this work, we carry out NEMD simulations to investigate the thermal properties of Si thin films. We find that strain has a strong influence on the thermal conductivity of thin films. Our work suggests that applying strain could serve as a means of tuning the thermal conductivity of nanoscale material.

## 2. Molecular Dynamic Simulation

The NEMD simulations of the Si thin films are performed using LAMMPS code. Figure 1 shows the simulation model in the present research. At the initialized condition, the positions of each atom are arranged according to the crystal lattice structure, and atomic velocities meet the Maxwell-Boltzmann distribution function. The thickness of the Si thin films chosen for this study is 10 Å, 15 Å, 20 Å, and 50 Å respectively, where Å is the lattice constant of Si. The periodic boundary conditions are applied in *X* and *Z* direction, and the free boundary conditions are applied in *Y* direction.

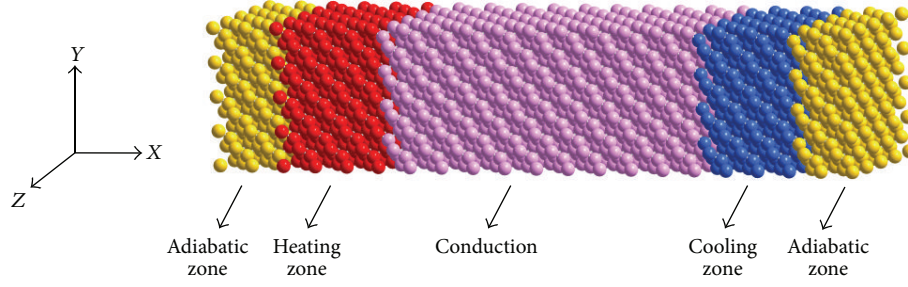


FIGURE 1: MD simulation model in Si thin film.

The cross-sectional area of YOZ is  $4 \text{ \AA} \times 4 \text{ \AA}$ . The heating and cooling zones with the thickness of  $3 \text{ \AA}$  create a temperature gradient in the system by controlling the energy given or taken from these regions. Adiabatic zones with the thickness of  $2 \text{ \AA}$  are constructed to prevent the atoms escaping from the system, and the velocities of each atom in this region are 0.

Tersoff three-body potential model is employed to describe the interaction among different Si atoms in the simulation film that is reliable to describe the semiconductor atoms potential properties [11]. The Newton's classical equations of motion for those atoms are solved with the Velocity-Verlet integration algorithm. The time step for the simulation is set as 1 fs. The simulations consist of two stages: the first stage is the constant-temperature simulation, in which the temperature is maintained at constant value with a coupling time of  $2 \times 10^6$  MD steps; the second stage is the constant-energy one with a coupling time of  $8 \times 10^6$  MD steps to ensure that the whole system reached an equilibrium state. The method proposed by Juncl and Jullien [12] is used to apply a specified heat flux by scaling the velocities of the atoms in the heating and cooling zones of the simulations. A specified amount of energy  $\Delta E$  (set to 1% of  $k_B T$ ) is added to the heating zone and the same amount of energy is subtracted from the cooling zone at each time step.

The velocities of all the particles in the heating and cooling zones are scaled according to the following equation:

$$v_{i,\text{new}} = v_G + \alpha (v_{i,\text{old}} - v_G), \quad (1)$$

where  $v_G$  is the velocity of the center mass, which is set as zero at the beginning of our simulations. A scaling factor  $\alpha$  is calculated from the following equation:

$$\alpha = \sqrt{1 \pm \frac{\Delta E}{\Delta E_k}}, \quad (2)$$

where  $E_k = \sum_{i=1}^N (1/2)m_i v_i^2$  is the kinetic energy of atoms in the hot or cold reservoirs.

Based on Fourier's law of conduction, the thermal conductivity is given as

$$\lambda = \frac{\Delta E}{2A\tau \cdot (\partial T / \partial x)}, \quad (3)$$

where  $\tau$  is the simulation step time and  $A$  is the cross-sectional area. To obtain the temperature distribution,

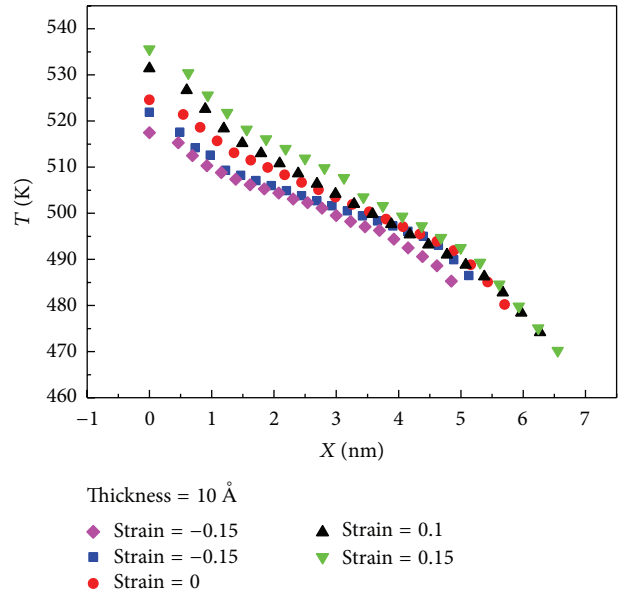


FIGURE 2: Temperature profile in the direction of heat transfer.

the system is divided into 20 planes along the X direction, and the instantaneous temperature of each plane is calculated using the following equation:

$$T = \frac{1}{3k_B N} \left\langle \sum_{i=1}^N \left( \frac{1}{2} m_i v_i^2 \right) \right\rangle, \quad (4)$$

where  $m_i$  is the mass of atoms,  $v_i$  is the velocity of atoms,  $N$  is the number of atoms in each plane,  $k_B$  is Boltzmann constant, and  $k_B = 1.38 \times 10^{-23} \text{ J/K}$ .

For the analysis, 0~15% tensile and compressive strain is imposed on our NEMD simulation system by recalibrating the atomic coordinates. The rate is 0.005 nm per  $10^5$  steps. When each load applying process is finished, the thin films need to achieve equilibrium for a certain relaxation time.

### 3. Results and Discussion

All the simulations are implemented at 500 K. Figure 2 displays the calculated temperature distributions in the film with strain of -0.1, 0, and 0.1, respectively. The typical distributions have been obtained in all simulation runs. Both ends of

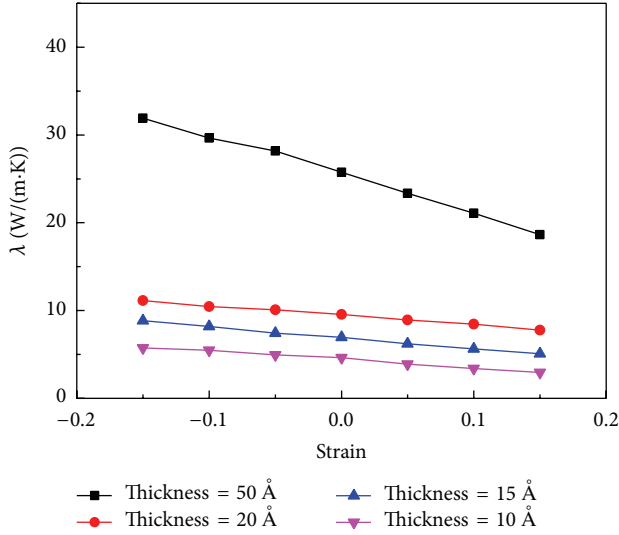


FIGURE 3: Thermal conductivity variation with strain.

the temperature profile show a nonlinear trend attributed to the strong scattering of heating and cooling zones. A linear temperature profile exists in the middle regions, and the gradient increases as the film strain increases.

As the film strain is changed in the range of  $-0.15 \sim 0.15$ , the thermal conductivity is collected in Figure 3. It is noted that the thermal conductivity decreases as the tensile strain increases and increases as the compressive strain increases. In addition, the strain has an even more significant effect on the thermal conductivity of the thin films with the thickness of  $50 \text{ \AA}$ , which may suggest that the strain effect on the thermal conductivity is largely preserved in the nanoscale configuration over all the sizes. When the thickness of thin film is  $10 \text{ \AA}$ , the thermal conductivity from its initial value of  $4.65 \text{ W/m}\cdot\text{K}$  decreases by about 27% as the tensile strain increases to 0.1 and increases by 18% as the compressive strain increases to 0.1. Such trend is consistent with the earlier reported analyses of other nanostructures in literature [13, 14]. It is also observed from Figure 3 that the thermal conductivity of Si thin films increases with the increase in thickness. This result has been proven earlier by both experimental and computational works. The explanation of the size effect on the thermal conductivity is due to the discretisation of the wave vectors for small systems and the phonon scattering at the boundary surface [15, 16].

To explain the coupling between strain and thermal conductivity, we calculated the phonon density of states (PDOS) for different strain which can describe accurately the thermal transport property of the material. Figure 4 shows that the peaks of PDOS almost coincide for different strain at low frequencies, and they are more sensitive to the strain at high frequencies. Different from bulk material, high frequency phonons play a much more important role in thermal conduction of thin films. The peak moves towards the left when the tensile strain is applied, while it moves towards the right when the compressive strain is applied. The results imply that the tensile strain can shift the high frequency phonons

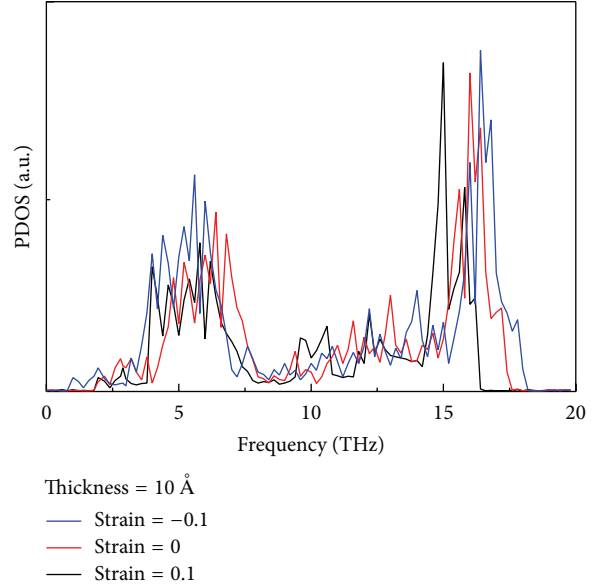


FIGURE 4: Strain dependent phonon density of states of Si thin films.

into low frequency phonons, and this shift could slow down the phonon group velocities [17]. Under compressive strain, most phonons will be at a higher frequency which could enhance thermal transportation capacity [18].

In gas kinetic theory, the lattice thermal conductivity can be calculated using the following expression:

$$\lambda = \frac{1}{3} C v \Lambda_{\text{eff}}, \quad (5)$$

where  $C$  is the heat capacity per unit volume and  $v$  and  $\Lambda_{\text{eff}}$  are the velocity of sound and mean free path of the phonons, respectively. It can be seen from (5) that the decline of phonon velocities due to the tensile strain will decrease the thermal conductivity of thin films.

On the other hand, the surface reconstructions of the simulation system contribute to the change in thermal conductivity. In Figures 5 and 6, the Si thin films with the thickness of  $10 \text{ \AA}$  under different tensile and compressive strain exhibit different atomic configuration characteristics. Under small strain (Figures 5(a), 5(b), 6(a), and 6(b)), the surface disorder is significantly small, and there is no plastic deformation in the simulation system. As the applied strain is increased, dislocations could be generation in the Si thin films under large strain due to the fact that the atoms will recombine with each other to form new bonds. Figures 5(c), 5(d), 6(c), and 6(d) show that the disordered region expands to the whole conducting zones and the plastic deformation occurs gradually, which are stable agreeing with the dislocation simulations result that the partial dislocations are nucleated raising the contribution of extended full dislocations [19]. The simulation partial dislocations are even separated into two pieces in our simulation with the tensile strain of 0.15. The surface reconstructions can scatter phonons significantly which leads to a reduction of the thermal conductivity. For the compressive strain increase to 0.15, a convex distortion is formed near the center of the thin films, while this structure

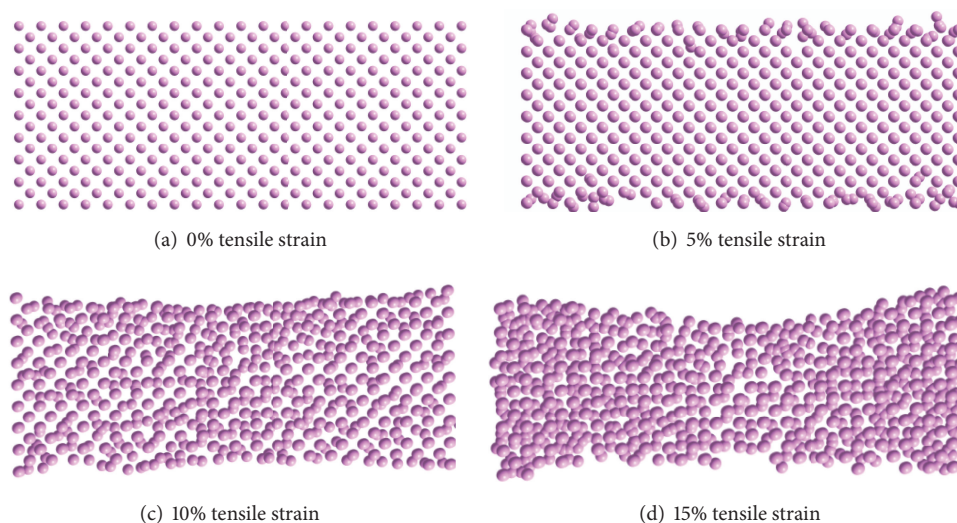


FIGURE 5: Configuration plots of Si thin films as the tensile strain increases.

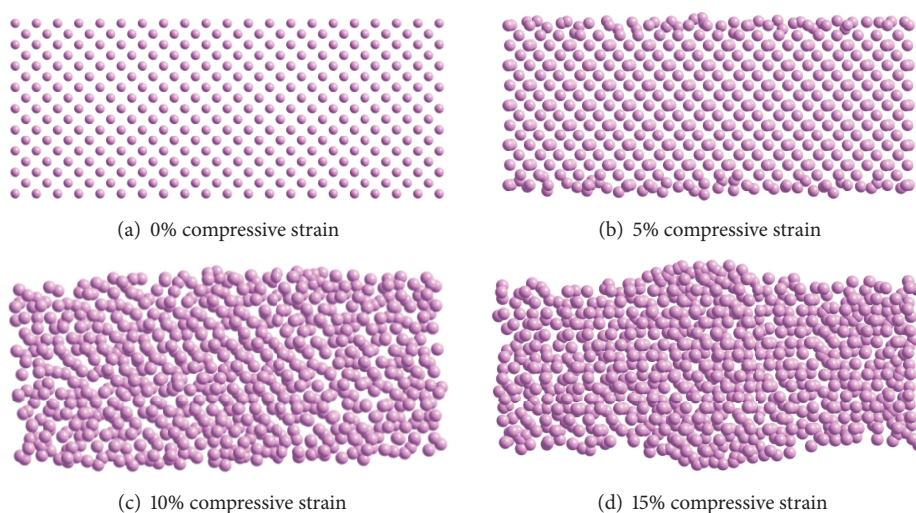


FIGURE 6: Configuration plots of Si thin films as the compressive strain increases.

transformation does not reduce the thermal conductivity. It may be due to the fact that the surface effect is lower than the effect of phonon group velocity under compressive strain.

#### 4. Conclusions

This study has performed an investigation into the thermal conductivities of Si thin films with varying strain. The simulation used the NEMD method to obtain a temperature gradient, and the thermal conductivities are then evaluated using the heat current and temperature gradient. The results have shown that the thermal conductivity of the Si thin films could be significantly decreased or increased by tensile or compressive strain. This is due to the mode-specific group velocities of phonons decreasing continuously from

compressive strain to tensile strain. In addition, the surface disorder is significantly increased from compressive strain to tensile strain. Our demonstration of large changes in thermal conductivity driven by strain may point to a new direction of dynamic thermal management.

#### Competing Interests

The authors declare no competing interests.

#### Acknowledgments

The project was supported by the Fundamental Research Funds for the Central Universities of China (Grant no. DL12BB38).

## References

- [1] D. Terris, K. Joulain, D. Lemonnier, D. Lacroix, and P. Chantrenne, "Prediction of the thermal conductivity anisotropy of Si nanofilms: results of several numerical methods," *International Journal of Thermal Sciences*, vol. 48, no. 8, pp. 1467–1476, 2009.
- [2] S. Ju and X. Liang, "Thermal conductivity of nanocrystalline silicon by direct molecular dynamics simulation," *Journal of Applied Physics*, vol. 112, no. 6, article 064305, 2012.
- [3] A. Bodapati, P. K. Schelling, S. R. Phillpot, and P. Keblinski, "Vibrations and thermal transport in nanocrystalline silicon," *Physical Review B*, vol. 74, no. 24, Article ID 245207, 2006.
- [4] S. H. Ju, X. G. Liang, and X. H. Xu, "Out-of-plane thermal conductivity of polycrystalline silicon nanofilm by molecular dynamics simulation," *Journal of Applied Physics*, vol. 110, no. 5, Article ID 054318, 2011.
- [5] X. L. Zhang and Z. W. Sun, "Effects of vacancy structural defects on the thermal conductivity of silicon thin films," *Semiconductor*, vol. 32, Article ID 053002, 2011.
- [6] M. Adamczyk, J. H. Schmid, T. Tiedje et al., "Comparison of strain relaxation in InGaAsN and InGaAs thin films," *Applied Physics Letters*, vol. 80, no. 23, pp. 4357–4359, 2002.
- [7] S. Bhowmick and V. B. Shenoy, "Effect of strain on the thermal conductivity of solids," *Journal of Chemical Physics*, vol. 125, no. 16, article 164513, 2006.
- [8] Y. Y. Zhang, Q. X. Pei, X. Q. He, and Y.-W. Mai, "A molecular dynamics simulation study on thermal conductivity of functionalized bilayer graphene sheet," *Chemical Physics Letters*, vol. 622, pp. 104–108, 2015.
- [9] X. Wang and S. P. Shen, "Effects of temperature and strain on thermal properties of Ni/Al laminated structure," *Computational Materials Science*, vol. 84, pp. 13–17, 2014.
- [10] Y. Xu and G. Li, "Strain effect analysis on phonon thermal conductivity of two-dimensional nanocomposites," *Journal of Applied Physics*, vol. 106, no. 11, Article ID 114302, 2009.
- [11] J. Tersoff, "New empirical approach for the structure and energy of covalent systems," *Physical Review B*, vol. 37, no. 12, pp. 6991–7000, 1988.
- [12] P. Juncl and R. Jullien, "Molecular-dynamics calculation of the thermal conductivity of vitreous silica," *Physical Review B—Condensed Matter and Materials Physics*, vol. 59, no. 21, pp. 13707–13711, 1999.
- [13] K. Jung, M. Cho, and M. Zhou, "Thermal and mechanical response of [0001]-oriented GaN nanowires during tensile loading and unloading," *Journal of Applied Physics*, vol. 112, no. 8, Article ID 083522, 2012.
- [14] X. Li, K. Maute, M. L. Dunn, and R. Yang, "Strain effects on the thermal conductivity of nanostructures," *Physical Review B*, vol. 81, no. 24, Article ID 245318, 2010.
- [15] P. K. Schelling, S. R. Phillpot, and P. Keblinski, "Comparison of atomic-level simulation methods for computing thermal conductivity," *Physical Review B—Condensed Matter and Materials Physics*, vol. 65, no. 14, Article ID 144306, 2002.
- [16] P. Chantrenne and J.-L. Barrat, "Finite size effects in determination of thermal conductivities: comparing molecular dynamics results with simple models," *Journal of Heat Transfer*, vol. 126, no. 4, pp. 577–585, 2004.
- [17] Z. Xu and M. J. Buehler, "Strain controlled thermomutability of single-walled carbon nanotubes," *Nanotechnology*, vol. 20, no. 18, Article ID 185701, 2009.
- [18] J. Zhang, X. He, L. Yang et al., "Effect of tensile strain on thermal conductivity in monolayer graphene nanoribbons: a molecular dynamics study," *Sensors*, vol. 13, no. 7, pp. 9388–9395, 2013.
- [19] L. Cao, A. Hunter, I. J. Beyerlein, and M. Koslowski, "The role of partial mediated slip during quasi-static deformation of 3D nanocrystalline metals," *Journal of the Mechanics and Physics of Solids*, vol. 78, pp. 415–426, 2015.

## Research Article

# Synthesis and Thermoelectric Properties of $C_{60}/Cu_2GeSe_3$ Composites

Degang Zhao, Jiai Ning, Shuyu Li, and Min Zuo

School of Materials Science and Engineering, University of Jinan, Jinan 250022, China

Correspondence should be addressed to Degang Zhao; mse\_zhaodg@ujn.edu.cn

Received 10 March 2016; Accepted 12 April 2016

Academic Editor: Yalin Dong

Copyright © 2016 Degang Zhao et al. This is an open access article distributed under the Creative Commons Attribution License, which permits unrestricted use, distribution, and reproduction in any medium, provided the original work is properly cited.

Nanosized  $C_{60}$  powder was sufficiently incorporated with  $Cu_2GeSe_3$  powder by ball milling and  $C_{60}/Cu_2GeSe_3$  composites were prepared by spark plasma sintering.  $C_{60}$  distributed uniformly in the form of clusters and the average size of cluster was lower than  $1\ \mu m$ . With the addition of  $C_{60}$  increasing, the electrical resistivity and Seebeck coefficient of  $C_{60}/Cu_2GeSe_3$  composites increased while the thermal conductivity decreased significantly which resulted from the phonon scattering by  $C_{60}$  clusters locating on the grain boundaries of  $Cu_2GeSe_3$  matrix. The maximum  $ZT$  of 0.20 was achieved at 700 K for 0.9%  $C_{60}/Cu_2GeSe_3$  sample.

## 1. Introduction

Thermoelectric (TE) material which directly converts electricity to heat (and vice versa) has attracted increasing worldwide attention due to their potential applications in electronic cooling, waste heat recovery, and special power supplies [1, 2]. The conversion efficiency of TE material is determined by the dimensionless figure of merit,  $ZT = \alpha^2 T / \rho \kappa$ , where  $\alpha$  is the Seebeck coefficient,  $\rho$  is the electrical resistivity,  $T$  is the absolute temperature, and  $\kappa$  is the total thermal conductivity. The total thermal conductivity consists of an electron part ( $\kappa_E$ ) and a phonon part ( $\kappa_L$ ). Therefore, to maximize  $ZT$  value of TE material, low  $\kappa$  and  $\rho$  as well as large  $\alpha$  are required. In recent years, several classes of bulk materials with high  $ZT$  have been developed, such as lead telluride, skutterudite, clathrates, and Cu-based chalcogenide semiconductors [3–5]. Cu-based chalcogenide compounds with a diamond-like structure such as ternary  $Cu_2MSe_3$  ( $M = Sn, Ge$ ) and  $Cu_3SbSe_4$  have attracted a lot of attention recently due to their quite low thermal conductivity. In several Cu-based chalcogenide systems, the  $Cu_2GeSe_3$  structure has partial “phonon glass electron crystal” (PGEC) characteristic which is possible to achieve high TE performance. The Cu-Se bond network dominates the electron conduction while the contribution from the element Ge is very weak; thus the Ge site is suitable for optimizing TE property. Various

attempts including doping by partial substitution have been made to improve the thermoelectric properties of  $Cu_2GeSe_3$  compound [6–8]. Cho et al. synthesized the  $Cu_2Ga_xGe_{1-x}Se_3$  samples and achieved the  $ZT$  value of 0.50 for  $Cu_2Ga_{0.07}Sn_{0.93}Se_3$  sample [9]. Chetty et al. reported the maximum  $ZT$  value of in-doped  $Cu_2In_xGe_{1-x}Se_3$  was 0.23 at 700 K for  $Cu_2In_{0.1}Ge_{0.9}Se_3$  sample [10]. Besides doping, the dispersion of nanostructure phases into thermoelectric matrix is also an attractive approach to improve the performance of TE materials. However,  $Cu_2GeSe_3$ -based thermoelectric composites are scarcely investigated because the enhancement of  $ZT$  is unapparent compared with the doping. Although significant reduction in  $\kappa_L$  can be achieved via enhanced phonon scattering at matrix/inclusion interfaces, the electrical resistivity of TE composites maybe also increases resulting in a marginal improvement of the overall  $ZT$  value. Therefore, effective enhancement of  $ZT$  for TE composites depends on the good selection of dispersed nanophase and the control of microstructure of composites [11].

Fullerene  $C_{60}$  has ultra high elastic module and is a chemically stable nonpolar molecule. Nanosized  $C_{60}$  maybe provide an effective phonon scattering which decreases  $\kappa_L$ . Meanwhile, the scattering of the charge carriers by  $C_{60}$  molecules could be ineffective due to the large value of electron (hole) wavelength compared to a fullerene size. Blank et al. ever reported that the addition of 0.5 vol%

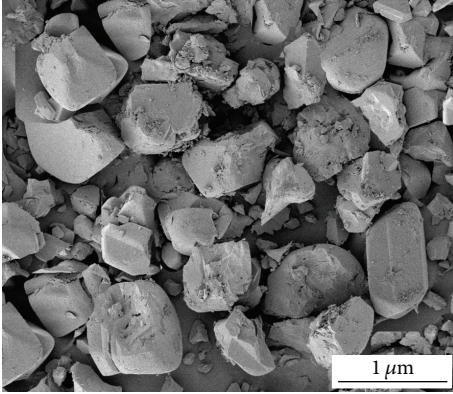


FIGURE 1: SEM image of fullerene powder with average particle size of 500 nm.

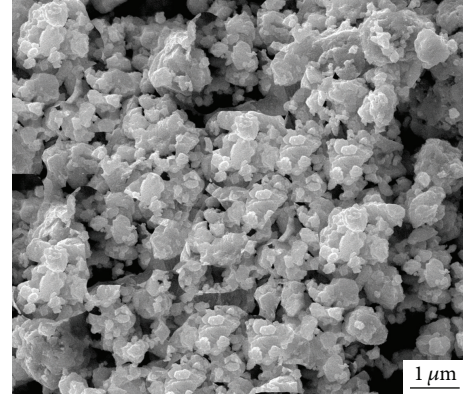


FIGURE 2: SEM image of the 1.2 vol%  $C_{60}/Cu_2GeSe_3$  powder after ball milling.

$C_{60}$  improved the TE properties of  $Bi_{0.5}Sb_{1.5}Te_3$  and the maximum  $ZT$  of 1.17 was obtained at 450 K [12, 13]. Shi et al. found that adding 6.5 mass%  $C_{60}$  into the binary  $CoSb_3$  can increase the  $ZT$  while adding amounts between 0.5% and 4.8% into  $CoSb_3$  decreased the  $ZT$  [14]. Nandihalli et al. also reported the  $ZT$  value of  $C_{60}/Ni_{0.05}Mo_3Sb_{5.4}Te_{1.6}$  composites was enhanced in the whole temperature range due to the large decrease of  $\kappa_L$  [15]. In this contribution, we attempted to introduce  $C_{60}$  into  $Cu_2GeSe_3$  system and expect to achieve larger reduction in  $\kappa_L$  of  $C_{60}/Cu_2GeSe_3$  composites.

In the present work,  $C_{60}$  powder was incorporated into  $Cu_2GeSe_3$  matrix using ball milling (BM) and  $C_{60}/Cu_2GeSe_3$  composites were fabricated by spark plasma sintering (SPS). Effects of  $C_{60}$  particles on the thermoelectric properties of  $C_{60}/Cu_2GeSe_3$  composites were discussed.

## 2. Experimental Procedures

The polycrystalline samples  $Cu_2GeSe_3$  were synthesized by melting method. The stoichiometric amounts of starting materials Cu (powder, 99.95%), Ge (powder, 99.999%), and Se (shot, 99.999%) were first placed in carbon crucible enclosed in evacuated fused-silica ampoules. The ampoules were slowly heated to 1223 K, held for 48 h in a vertical furnace, and then cooled to room temperature. To increase the homogeneity and crystallinity, the samples were annealed at 823 K for 72 h. The resulting ingots were initially ground into fine powder using mortar and pestle. Commercially available  $C_{60}$  powder with average particle size of 500 nm (Figure 1, XFNANO, China) was chosen as the nano-inclusions.  $C_{60}$  purity is 99.98% and the other 0.02% refers to impurities of  $C_{70}$  and other carbon structures.  $C_{60}$  particles were added to the  $Cu_2GeSe_3$  powder at fractions of 0.3, 0.6, 0.9, and 1.2 vol%, respectively. Then  $C_{60}$ -added  $Cu_2GeSe_3$  powders were mechanically ground with planetary ball milling equipment at 200 rpm for 300 min in an argon atmosphere. Steel balls of  $\Phi 5$  mm were charged as the milling media. The as-milled powders were sintered by spark plasma sintering (SPS 2040) at around 850 K for about 8 min under uniaxial pressure of 50 MPa in vacuum.

The densities of the sintered  $C_{60}/Cu_2GeSe_3$  composites were measured using the Archimedes method. The constituent phases of composites were determined by X-ray diffractometry (Cu  $K\alpha$ , Rigaku, Rint2000). The chemical compositions of bulk samples were characterized using electron probe microanalysis (EPMA, JEOL, and JXA-8100) with a wavelength dispersive spectrometer (WDS). The compositions were calculated by averaging five spots. The microstructure of all  $C_{60}/Cu_2GeSe_3$  composites was observed by high-resolution transmission electron microscopy (HREM, JEM2100F). The thermal diffusivity ( $\lambda$ ) was measured by laser flash method (Netzsch LFA427) in a flowing Ar atmosphere. The thermal conductivity was calculated from the relationship  $\kappa = c\lambda C_p$ , where  $c$  is the density of the sintered sample and  $C_p$  is the specific heat capacity.  $C_p$  (taken as 0.33 J/gK) was determined by the ratio method with a sapphire reference using a Netzsch Differential Scanning Calorimetry. The electrical resistivity and Seebeck coefficient were measured simultaneously using commercial equipment (ZEM-3, ULVAC-RIKO) on the bar-type sample with a dimension of  $2 \times 2 \times 10$  mm. The Hall coefficient ( $R_H$ ) was measured using the van der Pauw's method in vacuum with the magnetic field of 2 T. The carrier concentration ( $p_H$ ) and mobility ( $\mu_H$ ) were estimated from the relations of  $p_H = 1/(eR_H)$  and  $\mu_H = R_H/\rho$  based on the single band model, where  $e$  is the electronic charge. All the measurements were performed in a temperature range of 300–700 K.

## 3. Results and Discussion

**3.1. Microstructure and XRD Analysis.** Figure 2 displays the SEM image of 0.9 vol%  $C_{60}$ -added  $Cu_2GeSe_3$  powder after ball milling. It can be observed that the average size of milled  $C_{60}/Cu_2GeSe_3$  powder was about 100 nm. Figure 3 shows the XRD patterns of  $x C_{60}/Cu_2GeSe_3$  composites ( $x = 0, 0.3, 0.6, 0.9, \text{ and } 1.2$  vol%) after SPS. The measured relative densities for all  $C_{60}/Cu_2GeSe_3$  composites after SPS are above 97% of the theoretical value. The diffraction peaks in Figure 3 are well indexed based on the JCPDS 65-2533 of  $Cu_2GeSe_3$  (Imm2 group). However, no diffraction peak of  $C_{60}$  is found in the XRD of all  $C_{60}/Cu_2GeSe_3$  samples,

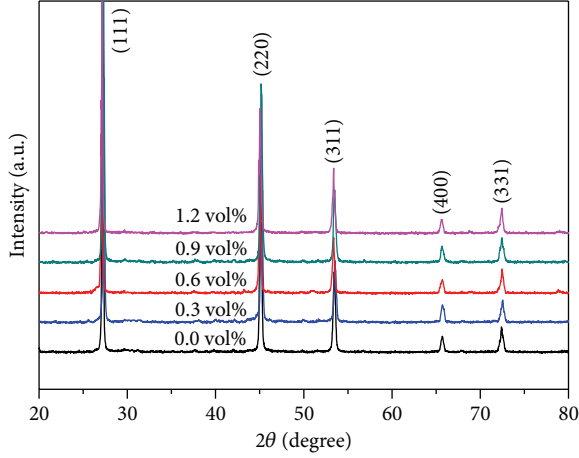


FIGURE 3: XRD patterns of sintered  $C_{60}/Cu_2GeSe_3$  composites.

which may be due to the low content of  $C_{60}$  in the composites. Therefore, all  $C_{60}/Cu_2GeSe_3$  samples show the same XRD patterns with the pure  $Cu_2GeSe_3$  sample. The sintered pure  $Cu_2GeSe_3$  sample and 1.2 vol%  $C_{60}/Cu_2GeSe_3$  composite are listed in Figures 4(a) and 4(b), respectively.  $C_{60}$  distributed uniformly in the form of clusters and the average size of cluster was lower than  $1\mu m$ . In Shi et al.'s research, most of  $C_{60}$  agglomerate into irregular micrometer size clusters located at the grain boundaries in the  $CoSb_3$  material [14]. The smaller size of clusters in this study should be due to the ball milling technology. The chemical composition of bulk  $C_{60}/Cu_2GeSe_3$  composites was characterized by SEM and EDS, as shown in Figure 5. The results of EDS also confirm that the matrix was composed of 33.53 at.% Cu, 16.85 at.% Ge, and 49.62 at.% Se, indicating  $Cu_2GeSe_3$  phase. The black phase only contains C element, corresponding to  $C_{60}$  phase. Figure 6 is the HRTEM image of  $C_{60}$  clusters in the composite. The area surrounded by the dashed lines in Figure 6 is a  $C_{60}$  particle. The size of  $C_{60}$  was about 80 nm, which means the ball milling process decreases the average size of  $C_{60}$  powder significantly. According to the theory proposed by Faleev et al. [16, 17], nanophases that distribute in the thermoelectric matrix can result in strain fields, which could cause some changes in the band structure of material and greatly influence its thermoelectric properties.

**3.2. Electrical Transport Properties.** The electrical resistivity ( $\rho$ ) as a function of temperature for  $C_{60}/Cu_2GeSe_3$  composites with different vol%  $C_{60}$  is shown in Figure 7.  $\rho$  of  $Cu_2GeSe_3$  matrix increases with rising temperature over the whole temperature range, indicating a typical behavior of a heavily doped semiconductor. The similar tendency of  $\rho$  was also present in  $C_{60}/Cu_2GeSe_3$  composites. In addition,  $\rho$  of  $C_{60}/Cu_2GeSe_3$  composites increases with the content of  $C_{60}$  increasing, which should be due to the enhanced carrier scattering at the incoherent interfaces between well dispersed  $C_{60}$  clusters and the  $Cu_2GeSe_3$  matrix. Generally, in the case of carriers dominantly scattered by grain barriers

or interfaces between the second phase and matrix in the composites, the carrier mobility can be expressed as [18]

$$\mu_H = \frac{el}{\sqrt{8k_B T \pi m^*}} e^{-E_B/k_B T}, \quad (1)$$

where  $k_B$  is the Boltzmann constant,  $m^*$  is the carrier effective mass,  $l$  is the average grain size, and  $E_B$  is the activation energy characterizing the barrier height between the matrix and second phase. As the relative density of  $x C_{60}/Cu_2GeSe_3$  composite is higher than 97%, the porosity effect could be eliminated. Table 1 lists some physical parameters of  $C_{60}/Cu_2GeSe_3$  composites at room temperature. It can be noted that the carrier mobility ( $\mu_H$ ) decreases with the content of  $C_{60}$  increasing. Therefore,  $\rho$  of  $C_{60}/Cu_2GeSe_3$  composites increases compared with  $\rho$  of  $Cu_2GeSe_3$  matrix.

Figure 8 displays the Seebeck coefficient ( $\alpha$ ) of  $x C_{60}/Cu_2GeSe_3$  composites as a function of temperature. All composites have a positive  $\alpha$  over the whole temperature range, indicating the holes are major carriers. With rising temperature,  $\alpha$  of all  $x C_{60}/Cu_2GeSe_3$  composites increases and  $\alpha$  of 1.2%  $C_{60}/Cu_2GeSe_3$  composite reaches  $183\mu V/K$  at 700 K. In addition,  $\alpha$  of  $C_{60}/Cu_2GeSe_3$  composites increases with the content of  $C_{60}$  increasing. At room temperature,  $\alpha$  increases from  $58\mu V/K$  for  $Cu_2GeSe_3$  matrix to  $101\mu V/K$  for 1.2%  $C_{60}/Cu_2GeSe_3$  composite. The enhancement of  $\alpha$  of  $x C_{60}/Cu_2GeSe_3$  composites should be related with the "energy filter" effect. The Seebeck coefficient can be expressed as [19]

$$\alpha = -\frac{\pi k_B}{3} \frac{k_B T}{e} \left. \frac{d \ln \sigma(E)}{dE} \right|_{E=E_F} - \frac{T}{n(E)} \left. \frac{dn(E)}{dE} \right|_{E=E_F}, \quad (2)$$

where  $k_B$ ,  $n(E)$ , and  $\sigma(E)$  are Boltzmann constant, value of density of states (DOS), and electrical conductivity, respectively. When nanophases or nano-inclusions are incorporated into a semiconducting matrix, the band bending at inclusion/matrix interface will produce potential energy barrier which could effectively block low energy electrons, while transmitting high energy electrons [20]. This "electron energy filter" could enhance the Seebeck coefficient by moving the Fermi level ( $E_F$ ) to an energy level with larger local DOS.

**3.3. Thermal Transport Properties.** Figure 9 displays the temperature dependence of total thermal conductivity ( $\kappa$ ) and lattice thermal conductivity ( $\kappa_L$ ) for  $C_{60}/Cu_2GeSe_3$  composites.  $\kappa_L$  is estimated by subtracting the electronic contribution via the Wiedemann-Franz law ( $\kappa_E = L_0 \sigma T$ , where the Lorenz number  $L_0$  is taken as a constant of  $2.0 \times 10^{-8} V^2/K^2$ ) from the total thermal conductivity.  $\kappa$  for all samples declines with increasing temperature. Moreover,  $\kappa$  of  $x C_{60}/Cu_2GeSe_3$  composites decreases with the content of  $C_{60}$  increasing. The achieved  $\kappa$  of 1.2%  $C_{60}/Cu_2GeSe_3$  composite at room temperature is  $1.43 W/mK$ , which is 45% lower than that of  $Cu_2GeSe_3$  matrix. The minimal  $\kappa$  of 1.2%  $C_{60}/Cu_2GeSe_3$  composite is  $0.65 W/mK$  at 700 K. As known to all, the grain boundary, wide or point defects, porosity, and impurity could contribute to the decrease of  $\kappa$ . Owing to the high relative density of  $C_{60}/Cu_2GeSe_3$  composites, the

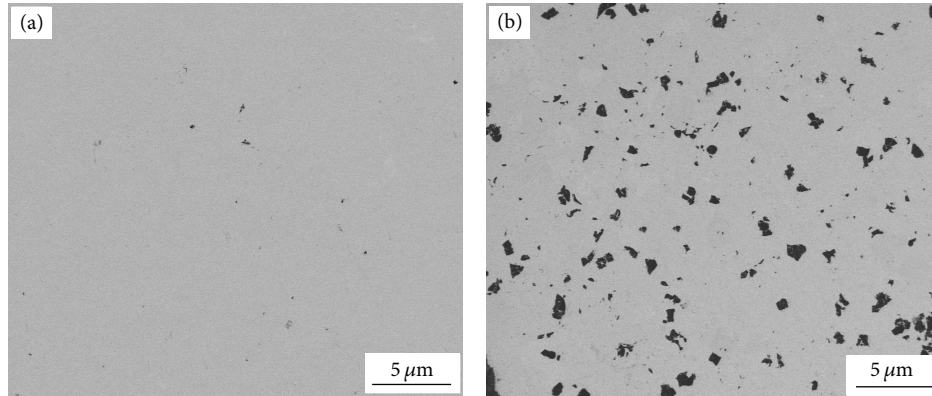


FIGURE 4: (a) SEM microstructure of the sintered pure  $\text{Cu}_2\text{GeSe}_3$ ; (b) SEM microstructure of sintered 1.2 vol%  $\text{C}_{60}/\text{Cu}_2\text{GeSe}_3$  composite.

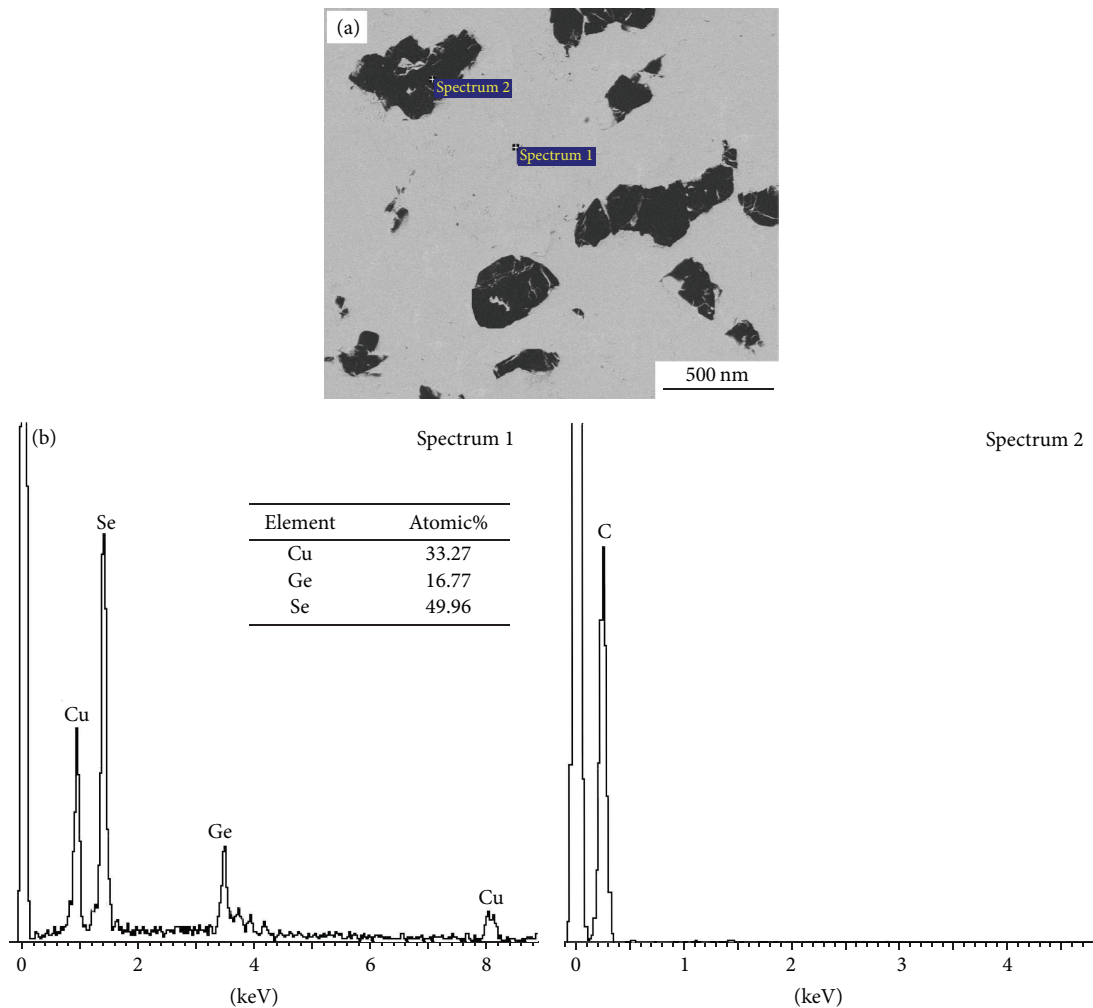


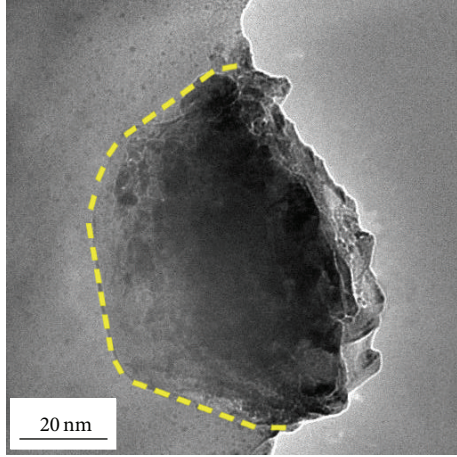
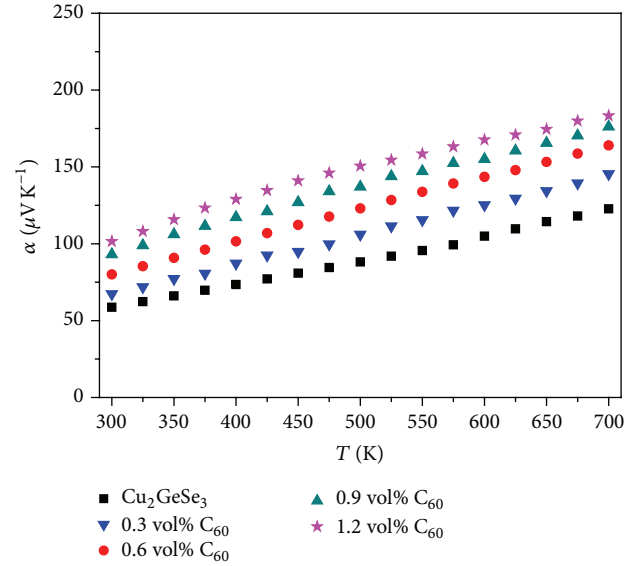
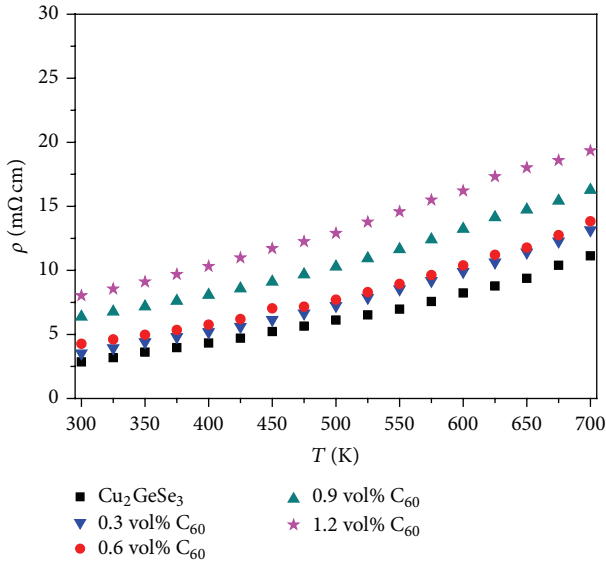
FIGURE 5: (a) SEM image of the sintered 1.2%  $\text{C}_{60}/\text{Cu}_2\text{GeSe}_3$  composite; (b) EDS results of  $\text{Cu}_2\text{GeSe}_3$  matrix and  $\text{C}_{60}$  phase.

reduction of  $\kappa$  originated from the porosity is negligible. Meanwhile, the calculation of  $\kappa_E$  shows that the reduction of  $\kappa_E$  has a limited contribution to the decrease of  $\kappa$ . Therefore, the decrease of  $\kappa$  for  $\text{C}_{60}/\text{Cu}_2\text{GeSe}_3$  composites mainly originates from the depression of  $\kappa_L$  due to the enhancement

of phonon scattering by  $\text{C}_{60}$  inclusions or nanoparticles in the composite. Figure 9(b) is the temperature dependence of  $\kappa_L$  of  $\text{C}_{60}/\text{Cu}_2\text{GeSe}_3$  composites.  $\kappa_L$  of  $\text{C}_{60}/\text{Cu}_2\text{GeSe}_3$  composites drastically decreases with the content of  $\text{C}_{60}$  increasing. The minimal  $\kappa_L$  achieved in the present work is 0.58 W/mK at

TABLE 1: Chemical composition and some physical parameters of  $x\text{C}_{60}/\text{Cu}_2\text{GeSe}_3$  composites at room temperature.

$x$ (vol%)	Relative density	$\rho$ (m $\Omega$ cm)	$p$ ( $10^{19}$ cm $^{-3}$ )	$\mu_H$ (cm $^2$ /Vs)	$\alpha$ ( $\mu$ V/K)	$\kappa_L$ (Wm $^{-1}$ K $^{-1}$ )
0	97.6%	2.85	13.8	15.7	58	2.37
0.3	98.1%	3.53	12.4	14.2	67	1.49
0.6	97.5%	4.26	12.1	12.0	80	1.46
0.9	98.3%	6.37	10.7	9.1	93	1.40
1.2	97.8%	8.02	9.5	8.2	101	1.36

FIGURE 6: HRTEM image of  $\text{C}_{60}$  particle in  $\text{C}_{60}/\text{Cu}_2\text{GeSe}_3$  composite.FIGURE 8: The Seebeck coefficient ( $\alpha$ ) as a function of temperature for  $\text{C}_{60}/\text{Cu}_2\text{GeSe}_3$  composites.FIGURE 7: The electrical resistivity ( $\rho$ ) as a function of temperature for  $\text{C}_{60}/\text{Cu}_2\text{GeSe}_3$  composites.

700 K for 1.2%  $\text{C}_{60}/\text{Cu}_2\text{GeSe}_3$ , which is 59% lower than that of pure  $\text{Cu}_2\text{GeSe}_3$ .

**3.4. Figure of Merit.** Figure 10 shows the dimensionless figure of merit ( $ZT$ ) of  $\text{C}_{60}/\text{Cu}_2\text{GeSe}_3$  composites as a function of temperature. Like other doped  $\text{Cu}_2\text{GeSe}_3$  investigated

before [9, 10, 21], the  $ZT$  value of  $\text{C}_{60}/\text{Cu}_2\text{GeSe}_3$  composites increases approximately linearly with increasing temperature. Compared with the  $ZT$  of  $\text{Cu}_2\text{GeSe}_3$  sample, the  $ZT$  value of  $\text{C}_{60}/\text{Cu}_2\text{GeSe}_3$  composites is enhanced. The inset in Figure 10 shows the  $ZT$  value as a function of volume fraction of  $\text{C}_{60}$  at different temperature. For 0.9%  $\text{C}_{60}/\text{Cu}_2\text{GeSe}_3$  composite, the maximum  $ZT$  is 0.20 at 700 K which is almost three times higher than that of pure  $\text{Cu}_2\text{GeSe}_3$  sample. The enhancement of  $ZT$  for  $\text{C}_{60}/\text{Cu}_2\text{GeSe}_3$  composites is mainly attributed to the reduced  $\kappa_L$  and the enhanced  $\alpha$ . The addition of nano- $\text{C}_{60}$  into the  $\text{Cu}_2\text{GeSe}_3$  matrix through BM method improves the TE properties, which provides a novel process to design Cu-based chalcogenide compounds with high TE performance. When the material with optimized carrier concentration is selected as the matrix, the higher  $ZT$  value of TE composite could be obtained.

#### 4. Conclusions

In this study,  $\text{C}_{60}$  was incorporated into  $\text{Cu}_2\text{GeSe}_3$  matrix and  $\text{C}_{60}/\text{Cu}_2\text{GeSe}_3$  composites were fabricated using BM-SPS method.  $\text{C}_{60}$  phase distributed uniformly in the form of clusters and the average size of cluster was lower than  $1\mu\text{m}$ . With the content of  $\text{C}_{60}$  increasing, the electrical

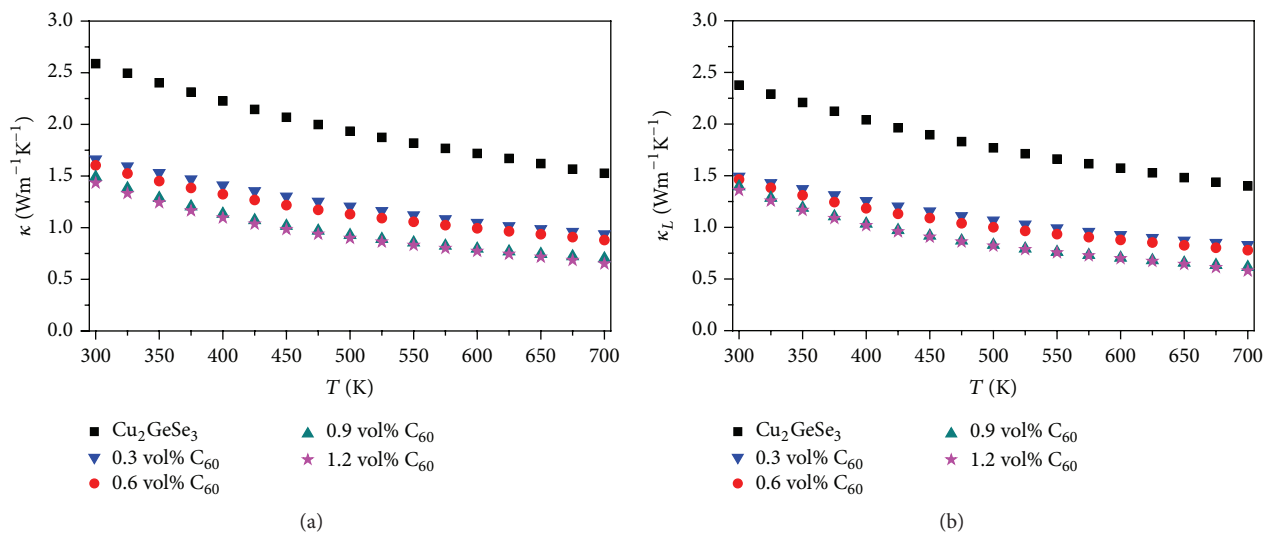


FIGURE 9: Temperature dependence of total thermal conductivity ( $\kappa$ ) of  $C_{60}/Cu_2GeSe_3$  composites; (b) temperature dependence of lattice thermal conductivity ( $\kappa_L$ ) of  $C_{60}/Cu_2GeSe_3$  composites.

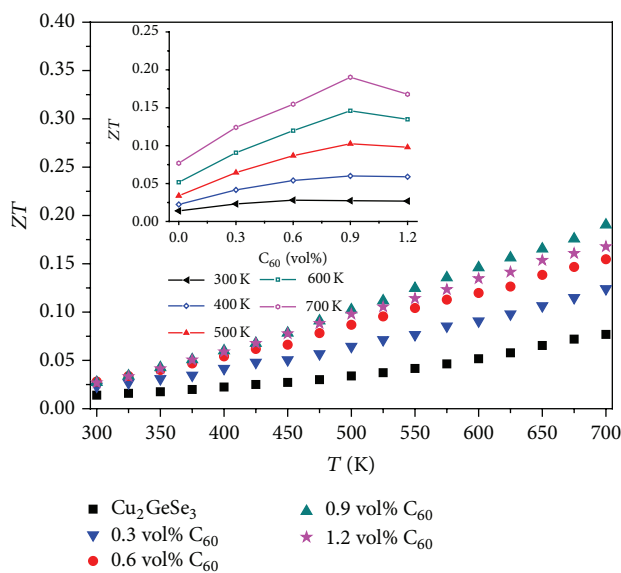


FIGURE 10: Temperature dependence of dimensionless figure of merit ( $ZT$ ) of  $C_{60}/Cu_2GeSe_3$  composites. The inset shows the  $ZT$  value as a function of volume fraction of  $C_{60}$ .

resistivity and Seebeck coefficient of  $C_{60}/Cu_2GeSe_3$  composites increased. The thermal conductivity of  $C_{60}/Cu_2GeSe_3$  composites decreased significantly which originated from the phonon scattering by  $C_{60}$  clusters locating on the grain boundaries of  $Cu_2GeSe_3$  matrix. The highest  $ZT$  value for 0.9%  $C_{60}/Cu_2GeSe_3$  composite was 0.20 at 700 K.

## Competing Interests

The authors declare that they have no competing interests.

## Acknowledgments

The authors would like to thank the help for the measurement of TE properties in California Institute of Technology and the discussion with Dr. Jeffrey. G. Snyder. Financial support from the National Natural Science Foundations of China (51202088) is acknowledged.

## References

- [1] F. J. Disalvo, "Thermoelectric cooling and power generation," *Science*, vol. 285, no. 5428, pp. 703–706, 1999.
- [2] W. S. Liu, X. Yan, G. Chen, and Z. F. Ren, "Recent advances in thermoelectric nano-composites," *Nano Energy*, vol. 1, no. 1, pp. 42–56, 2012.
- [3] S. K. Bux, J.-P. Fleurial, and R. B. Kaner, "Nanostructured materials for thermoelectric applications," *Chemical Communications*, vol. 46, no. 44, pp. 8311–8324, 2010.
- [4] L. L. Xi, J. Yang, C. F. Lu, Z. Mei, W. Q. Zhang, and L. Chen, "Systematic study of the multiple-element filling in caged skutterudite  $CoSb_3$ ," *Chemistry of Materials*, vol. 22, no. 7, pp. 2384–2394, 2010.
- [5] Y. Gelbstein and J. Davidow, "Highly efficient functional  $Ge_xPb_{1-x}Te$  based thermoelectric alloys," *Physical Chemistry Chemical Physics*, vol. 16, pp. 20120–20126, 2014.
- [6] W. G. Zerer, A. Lalonde, Z. M. Gibbs et al., "Influence of a nano phase segregation on the thermoelectric properties of the p-type doped stannite compound  $Cu_{2+x}Zn_{1-x}GeSe_4$ ," *Journal of the American Chemical Society*, vol. 134, no. 16, pp. 7147–7154, 2012.
- [7] J. Fan, H. L. Liu, X. Y. Shi et al., "Investigation of thermoelectric properties of  $Cu_2Ga_xSn_{1-x}Se_3$  diamond-like compounds by hot pressing and spark plasma sintering," *Acta Materialia*, vol. 61, no. 11, pp. 4297–4304, 2013.
- [8] G. H. Liu, J. T. Li, K. X. Chen et al., "Direct fabrication of highly-dense  $Cu_2ZnSnSe_4$  bulk materials by combustion synthesis for

- enhanced thermoelectric properties,” *Material Design*, vol. 93, no. 19, pp. 238–246, 2016.
- [9] J. Y. Cho, X. Shi, J. R. Salvador et al., “Thermoelectric properties and investigations of low thermal conductivity in Ga-doped  $\text{Cu}_2\text{GeSe}_3$ ,” *Physical Review B*, vol. 84, Article ID 085207, 2011.
- [10] R. Chetty, D. S. P. Kumar, M. Falmbigl et al., “Thermoelectric properties of Indium doped  $\text{Cu}_2\text{GeSe}_3$ ,” *Intermetallics*, vol. 54, no. 6, pp. 1–6, 2014.
- [11] M. Zebarjadi, K. Esfarjani, M. S. Dresselhaus, Z. F. Ren, and G. Chen, “Perspectives on thermoelectrics: from fundamentals to device applications,” *Energy and Environmental Science*, vol. 5, no. 1, pp. 5147–5162, 2012.
- [12] V. D. Blank, S. G. Buga, V. A. Kulbachinskii et al., “Thermoelectric properties of  $\text{Bi}_{0.5}\text{Sb}_{1.5}\text{Te}_3/\text{C}_{60}$  nanocomposites,” *Physical Review B*, vol. 86, no. 7, Article ID 075426, 8 pages, 2012.
- [13] V. A. Kulbachinskii, V. G. Kytin, M. Yu. Popov et al., “Composites of  $\text{Bi}_{2-x}\text{Sb}_x\text{Te}_3$  nanocrystals and fullerene molecules,” *Journal of Solid State Chemistry*, vol. 193, no. 18, pp. 64–70, 2012.
- [14] X. Shi, L. Chen, J. Yang, and G. P. Meisner, “Enhanced thermoelectric figure of merit of  $\text{CoSb}_3$  via large-defect scattering,” *Applied Physics Letters*, vol. 84, no. 13, pp. 2301–2303, 2004.
- [15] N. Nandihalli, A. Lahwal, D. Thompson et al., “Thermoelectric properties of composites made of  $\text{Ni}_{0.05}\text{Mo}_3\text{Sb}_{5.4}\text{Te}_{1.6}$  and fullerene,” *Journal of Solid State Chemistry*, vol. 203, pp. 25–30, 2013.
- [16] S. V. Faleev and F. Léonard, “Theory of enhancement of thermoelectric properties of materials with nanoinclusions,” *Physical Review B*, vol. 77, no. 21, Article ID 214304, 2008.
- [17] M. Zebarjadi, K. Esfarjani, A. Shakouri et al., “Effect of nanoparticle scattering on thermoelectric power factor,” *Applied Physics Letters*, vol. 94, no. 20, Article ID 202105, 2009.
- [18] J. W. Orton and M. J. Powell, “The Hall effect in polycrystalline and powdered semiconductors,” *Reports on Progress in Physics*, vol. 43, no. 11, pp. 1263–1307, 1980.
- [19] D. G. Zhao, M. Zuo, J. Leng, and H. Geng, “Synthesis and thermoelectric properties of  $\text{CoSb}_3/\text{WO}_3$  thermoelectric composites,” *Intermetallics*, vol. 40, no. 3, pp. 71–75, 2013.
- [20] Z. Xiong, X. Chen, X. Huang, S. Bai, and L. Chen, “High thermoelectric performance of  $\text{Yb}_{0.26}\text{Co}_4\text{Sb}_{12}/y\text{GaSb}$  nanocomposites originating from scattering electrons of low energy,” *Acta Materialia*, vol. 58, no. 11, pp. 3995–4002, 2010.
- [21] E. J. Skoug, J. D. Cain, and D. T. Morelli, “Thermoelectric properties of the  $\text{Cu}_2\text{SnSe}_3$ - $\text{Cu}_2\text{GeSe}_3$  solid solution,” *Journal of Alloys and Compounds*, vol. 506, no. 1, pp. 18–21, 2010.

## Research Article

# Active Multiple Plasmon-Induced Transparency with Graphene Sheets Resonators in Mid-Infrared Frequencies

Jicheng Wang,<sup>1,2</sup> Baojie Tang,<sup>2</sup> Xiushan Xia,<sup>2</sup> and Shutian Liu<sup>1</sup>

<sup>1</sup>*Department of Physics, Harbin Institute of Technology, Harbin 150001, China*

<sup>2</sup>*School of Science, Jiangnan University, Wuxi 214122, China*

Correspondence should be addressed to Jicheng Wang; [jcwanghit@163.com](mailto:jcwanghit@163.com) and Shutian Liu; [stliu@hit.edu.cn](mailto:stliu@hit.edu.cn)

Received 20 January 2016; Accepted 30 March 2016

Academic Editor: Yan Wang

Copyright © 2016 Jicheng Wang et al. This is an open access article distributed under the Creative Commons Attribution License, which permits unrestricted use, distribution, and reproduction in any medium, provided the original work is properly cited.

A multiple plasmon-induced transparency (PIT) device operated in the mid-infrared region has been proposed. The designed model is comprised of one graphene ribbon as main waveguide and two narrow graphene sheets resonators. The phase coupling between two graphene resonators has been investigated. The multimode PIT resonances have been found in both cases and can be dynamically tuned via varying the chemical potential of graphene resonators without optimizing its geometric parameters. In addition, this structure can get multiple PIT effect by equipping extra two sheets on the symmetric positions of graphene waveguide. The simulation results based on finite element method (FEM) are in good agreement with the resonance theory. This work may pave new way for graphene-based thermal plasmonic devices applications.

## 1. Introduction

Surface plasmon polaritons (SPPs), coupled modes of plasmons and photons, propagate along the metal-dielectric interface [1, 2]. SPPs provide an intriguing approach to localize and guide light in subwavelength metallic structures. In recent years, a great variety of efforts have been devoted to applications based on SPPs, which promotes the development for high density integration of photonic circuits. Electromagnetically induced transparency (EIT) is a sharp transparency window within a broad absorption spectrum in the medium, which is due to the coherent interaction between atomic upper levels and applied optical field [3, 4]. Recently, a novel analogy phenomenon to EIT, known as plasmonically induced transparency (PIT), has been manifested in various systems based on metamaterial structures [5–12]. The PIT effect has been applied in various applications such as nonlinear optical processes, ultrafast switching, slow light, and signal processing [13, 14]. However, the most of PIT effects are based on MIM (metal-insulator-metal) structure, and the adjustment of PIT effects must rely on changing the geometrical parameter of structures. Recently, multimode

PIT effects have been achieved by dual coupled graphene-integrated ring resonators [15, 16]. The MIM was replaced by graphene structure to achieve PIT effects without modifying parameter of structure. The dynamically tunable PIT planar hybrid metamaterials have been proposed, in which the VO<sub>2</sub> stripes are filled in the grooves of the device surface. The simulation results indicate that the PIT effects can be achieved by changing the temperature of VO<sub>2</sub> stripes [17]. To compare with [18], the structure of our proposal is simpler and more convenient in modulating PIT effects.

In recent years, graphene has aroused extensive attention for its unique and fantastic properties in optics and electronics [19]. A monolayer graphene has been widely researched as a promising platform for plasmonics for well supporting SPPs on graphene [20, 21]. Most importantly, the surface conductivity of graphene could be dynamically tuned by chemical potential via gate voltage, electric field, magnetic field, and chemical doping [22], which increasingly promotes the development of active plasmonic devices including polarizers [23], high-speed optical modulators [24], absorbers [25], and transformation optical devices [26]. Zeng et al. have

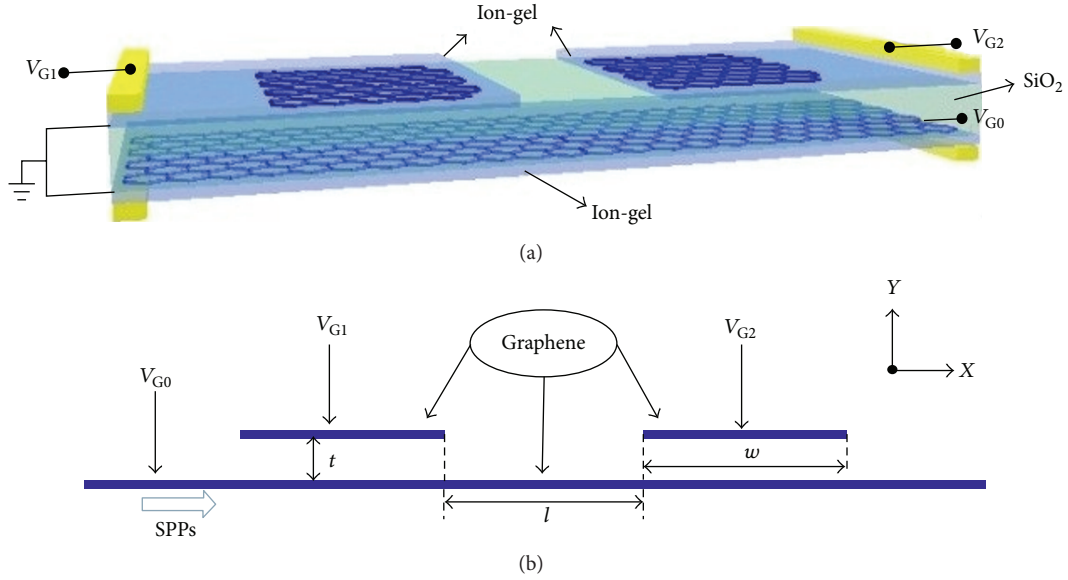


FIGURE 1: Schematic of plasmonic structure consists of two graphene ribbon and two graphene sheets. (a) Three-dimensional schematic of the plasmonic device. (b) Side view of the device configuration.  $w = 200$  nm is the length of two graphene sheets;  $t = 50$  nm is the coupling distance between graphene waveguide and two graphene sheets;  $l = 300$  nm is the separation between two graphene sheets;  $V_{G0}$ ,  $V_{G1}$ , and  $V_{G2}$ , respectively, represent the gate voltages on graphene waveguide and two graphene sheets.

studied a graphene-integrated Fabry-Perot (F-P) microcavity to efficiently modulate plasmon-induced transparency effect [27]. Shi et al. numerically demonstrated a plasmonic analog to EIT based on graphene nanostructures [28]. Therefore, the monolayer graphene is a promising platform to design a dynamically wavelength tunable PIT planar device.

In this paper, we have proposed and investigated a PIT device operating in the mid-infrared region. The designed model consisted of one graphene ribbon as main waveguide and two narrow graphene sheets as resonators. Firstly, a graphene waveguide side-coupled with single graphene resonator has been studied as a filter. Next, the phase coupling between two graphene resonators side-coupled to the main graphene waveguide has been investigated. In order to modulate multipeak PIT, four sheets were inserted into the symmetric position of graphene waveguide. The multimode and multipeak PIT resonances can be actively controlled via changing the chemical potential (Fermi energy) of graphene. Our designs have been well verified by numerical simulation based on finite element method (FEM). Hence, the proposed structures may have great potential in ultra-compact graphene thermal plasmonic devices in the infrared range.

## 2. Method

The structure of proposed device is schematically depicted in Figure 1. It consists of one graphene ribbon as main waveguide and two uniform graphene sheets as resonators. For experimental consideration, the designed graphene system is assumed in the  $\text{SiO}_2$  medium. It should be noted that the  $\text{SiO}_2$  medium is replaced with air in simulation for simplicity. The Kubo formula has governed the optical conductivity of graphene including the interband and intraband transition

contributions [29]. It depends on the momentum relaxation time  $\tau$ , temperature  $T$ , incident wavelength  $\lambda$  (angular frequency  $\omega$ ), and chemical potential (Fermi energy  $E_f$ )  $\mu_c$ . The surface conductivity of graphene  $\sigma_g$  follows the equation

$$\sigma_g = \frac{ie^2\mu_c}{\pi\hbar^2(\omega + i\tau^{-1})} + \frac{ie^2}{4\pi\hbar} \ln \left[ \frac{2|\mu_c| - (\omega + i\tau^{-1})\hbar}{2|\mu_c| + (\omega + i\tau^{-1})\hbar} \right] + \frac{ie^2k_B T}{\pi\hbar^2(\omega + i\tau^{-1})} 2 \ln \left[ \exp\left(-\frac{\mu_c}{k_B T}\right) + 1 \right]. \quad (1)$$

In our simulation, the employed incident light is in the mid-infrared region where the intraband transition contribution dominates in monolayer graphene [30]. Under this condition, the optical conductivity is given by

$$\sigma_g(\omega) = \frac{ie^2\mu_c/\pi\hbar^2}{\omega + i\tau^{-1}}. \quad (2)$$

Here,  $e$  is the electron charge and the carrier relaxation time  $\tau = \mu\mu_c/(ev_f^2)$  relates to the carrier mobility  $\mu$ , chemical potential  $\mu_c$ , and Fermi velocity  $v_f = 10^6$  m/s in graphene. The equivalent permittivity of graphene is given by the equation [26]

$$\varepsilon_{g,eq} = 1 + \frac{i\sigma_g\eta_0}{k_0\Delta}, \quad (3)$$

where  $k_0 = 2\pi/\lambda$  is wave number in vacuum and  $\eta_0 \approx 377 \Omega$  is the intrinsic impedance of air. The carrier mobility is reasonably chosen to be  $\mu = 20000 \text{ cm}^2 \text{ V}^{-1} \text{ s}^{-1}$  from experiment results [25, 31]. The thickness of graphene is assumed as  $\Delta = 0.5$  nm in order to take the numerical

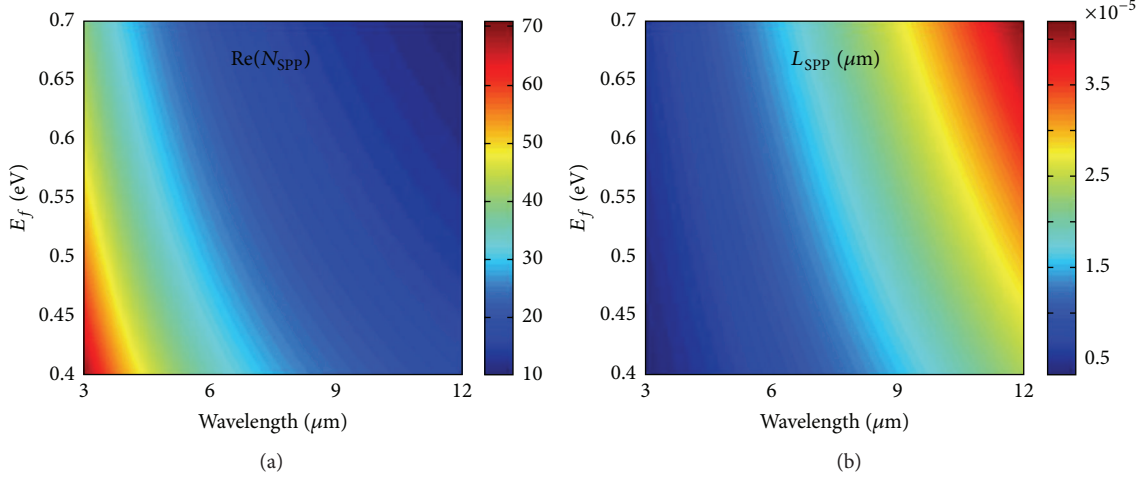


FIGURE 2: (a) Real part of effective refractive index for graphene SPPs as a function of incident wavelength and Fermi level. (b) Dependence of propagation length  $L_{\text{SPP}}$  on incident wavelength and the Fermi level.

simulation, but  $\Delta$  is not the real thickness of the graphene [19, 21]. TM- (Transverse Magnetic-) polarized SPPs on graphene are only in consideration for the investigation. The dispersion relation of this TM SPP surface wave follows the equation

$$\beta_{\text{SPP}} = k_0 \sqrt{\epsilon_r - \left( \frac{2\epsilon_r}{\eta_0 \sigma_g} \right)^2}, \quad (4)$$

where  $\beta_{\text{SPP}}$  is the propagation constant of graphene SPPs in air ( $\epsilon_r = 1$ ). The effective refractive index of graphene SPPs shows the ability to confine SPPs on graphene, which is defined as  $N_{\text{SPP}} = \beta_{\text{SPP}}/k_0$ . The propagation length  $L_{\text{SPP}} = 1/\text{Im}(\beta_{\text{SPP}})$  that indicates the SPP propagation loss in graphene. The dependences of  $\text{Re}(N_{\text{SPP}})$  and  $L_{\text{SPP}}$  on the Fermi level  $E_f$  and incident light wavelength  $\lambda$  are shown in Figure 2. Obviously, from Figure 2(a),  $\text{Re}(N_{\text{SPP}})$  increases as the Fermi level  $E_f$  decreases for a fixed wavelength, which means that SPPs are better confined when Fermi level is lower. Nevertheless, the tendency in Figure 2(b) is evidently opposite to that in Figure 2(a), indicating that a lower Fermi level gives a smaller propagation length. Thus, both these important factors should be taken into consideration in the design of PIT systems. Interestingly,  $\text{Re}(N_{\text{SPP}})$  varies greatly when the Fermi level is changed slightly, which provides a way to actively control our configuration.

### 3. Result and Discussion

At first, we focus on one single graphene resonator side-coupled to graphene waveguide as a filter. As shown in Figure 1, there are two graphene sheet resonators whereas we set the right resonator inactive by fixing its  $E_f$  at 0.05 eV. Under this condition SPPs will not be supported on graphene because the interband transition of electrons occurs at this Fermi energy [11]. The Fermi level of graphene waveguide is fixed at 0.4 eV. When SPPs on graphene meets the resonant condition, the graphene resonator will influence the transmission of main waveguide by forming standing wave. The resonance wavelength is determined by the width and Fermi

level of the graphene resonator, which can be deduced from quasi-static analysis and Drude-like model [19, 32]. It follows the following equation:

$$\lambda_r \approx \frac{2\pi\hbar c}{e} \sqrt{\frac{\epsilon_r \epsilon_0 \pi \eta w}{\chi E_f}}. \quad (5)$$

Here,  $c$  is the velocity of light in vacuum and  $\chi$  parameter is introduced for a freestanding graphene sheet ( $\chi = 1/\epsilon_r = 1$ ) [33]. The fitting dimensionless parameter  $\eta$  can be derived from numerical simulation [19, 31, 34] and  $w = 200$  nm is the width of graphene sheet. The resonance condition is given by  $2\text{Re}(k_{\text{SPP}})w + \Phi = 2m\pi$  [34]. Here,  $m$  is an arbitrary positive integer, resonance mode number, and  $\Phi$  is an additional phase shift because of the edge ends of the graphene sheets. Actually, the influence of the edge ends is only effective when the structure is in extremely small size, so we can neglect the influence in most cases [33, 35]. Besides, another equation for propagation constant of SPPs on monolayer graphene has been derived by combining the Drude-like model with the dispersion relation [36]:

$$k_{\text{SPP}} \approx \frac{8\pi^3 \hbar^2 c \epsilon_r}{e^2 E_f \eta_0 \lambda^2} + i \frac{4\pi^2 \hbar^2 \epsilon_r}{e^2 E_f \eta_0 \tau \lambda}. \quad (6)$$

By using the FEM, the transmission spectra have been calculated for different Fermi level  $E_f$  of left graphene resonator ranging from 3.6  $\mu\text{m}$  to 5  $\mu\text{m}$ , shown in Figure 3(a). The above discussion indicates that SPPs are better confined when Fermi level is lower. So the Fermi level is selected to be 0.42 eV, 0.43 eV, 0.44 eV, 0.45 eV, and 0.46 eV, respectively. The corresponding transmission spectra are denoted by blue, pink, green, purple, and red lines, respectively. As the Fermi level  $E_f$  decreases, an obvious red shift of the transmission dip can be found. Obviously, the larger Fermi levels correspond to the higher transmission dips at the same resonance mode, shown in Figure 3(a). It is because that the loss of propagation mode determined by the imaginary part of  $k_{\text{SPP}}$  is inversely proportional to the Fermi level.

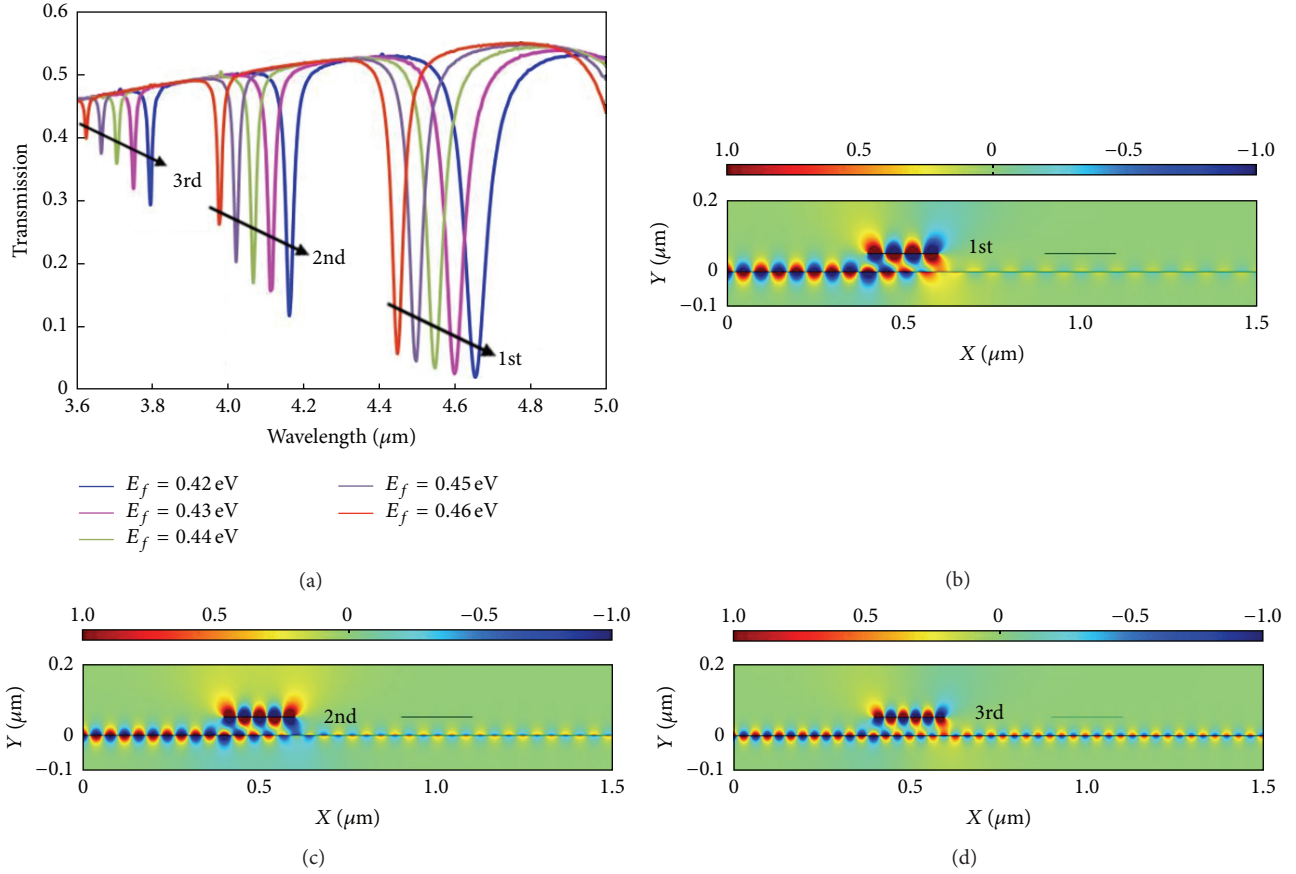


FIGURE 3: The graphene system with the right graphene sheet turned off. (a) The transmission spectra correspond to different Fermi level  $E_f$  of left graphene sheet,  $E_f = 0.42$  eV,  $0.43$  eV,  $0.44$  eV,  $0.45$  eV, and  $0.46$  eV denoted by blue, pink, green, purple, and red lines, respectively. The magnetic distributions  $|H_z|$  correspond to different resonance wavelengths when the Fermi level has been fixed at  $0.42$  eV. (b)  $\lambda_r = 3.8 \mu\text{m}$ . (c)  $\lambda_r = 4.17 \mu\text{m}$ . (d)  $\lambda_r = 4.66 \mu\text{m}$ .

As shown in Figures 3(b)–3(d), when SPPs on graphene meets the resonant condition, the energy can be confined in graphene sheet by forming a standing wave mode, which leads transmission dips. According to the above analysis, this structure can achieve filter effects by controlling Fermi level without optimizing geometric parameters.

Next, the influence of interval  $t$  has been investigated. The transmission spectra have been calculated for different values of  $t$  (45 nm, 50 nm, 55 nm, 60 nm, and 65 nm), shown in Figure 4. The transmission spectra of  $t$  selected to be 45, 50, 55, 60, and 65 nm are represented by blue, pink, green, purple, and red lines, respectively. Obviously, as the interval  $t$  increases, the coupling process becomes weaker. In order to investigate the coupling between main waveguide and graphene sheet concretely, the coupled mode theory is introduced to interpret the simulation results. By using coupled mode theory, the transmission can be expressed as  $T = (1/\tau_\omega)^2 / [(\omega - \omega_0)^2 + (1/\tau_i + 1/\tau_\omega)^2]$  [37]. Here,  $\omega$  and  $\omega_0$  are the incident frequency and the resonance frequency, respectively.  $1/\tau_i$  is the decay rate resulting from the intrinsic loss of graphene sheet resonator, and  $1/\tau_\omega$  is the decay rate due to the power escaping from the graphene waveguide. With the growing of interval  $t$ , the decay rate  $1/\tau_\omega$  decreases while the decay rate  $1/\tau_i$  remains the same. In this way, the

energy confined in graphene resonator will become less for an increasing interval  $t$ , which leads to a growing value of the transmission dip. At the same time, the spectra width  $\Delta\lambda \approx 4\pi c(1/\tau_i + 1/\tau_\omega)/\omega_0^2$  is proportional to the decay rate  $1/\tau_\omega$ . That explains that the spectrum width becomes narrower with a growing interval  $t$  at one resonance mode. This structure can achieve best filter effect when interval  $t$  is fixed at 50 nm.

In this section, the discussion focuses on the phase coupling between two graphene sheet resonators. To avoid the direct interference between two graphene sheets, the separation  $l$  has been chosen to be large enough. The other geometric parameters are selected as follows:  $l = 300$  nm and  $t = 50$  nm. We know that the resonance wavelength can be tuned via gate voltage on graphene sheets through the resonant condition. The difference of resonant wavelength between two graphene resonators is defined as  $\delta_i = \lambda_1 - \lambda_2$  ( $i = 1, 2, 3$  for each mode). The  $E_f$  of left graphene sheet is fixed at  $0.42$  eV, which presents three resonance dips ( $4.655 \mu\text{m}$ ,  $4.165 \mu\text{m}$ ,  $3.8 \mu\text{m}$ ) corresponding to first-order, second-order, and third-order resonance modes depicted in Figure 3(a). The gradually increasing  $\delta_i$  leads to a broader gap between two resonance dips for three resonance modes as  $E_f$  of the right sheet grows from  $0.425$  eV to  $0.44$  eV. In Figures 5(a), 5(b), and 5(c), for each resonance mode, all PIT windows

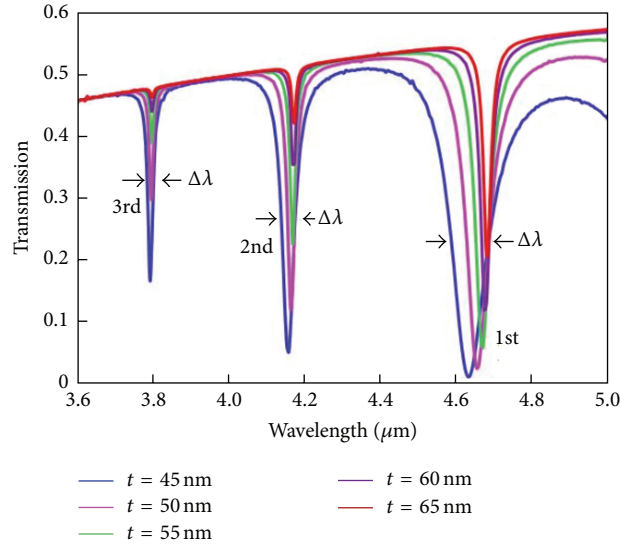


FIGURE 4: The graphene system with the right graphene sheet turned off. The transmission spectra correspond to different coupling interval  $t$  of graphene sheets;  $t = 45$  nm, 50 nm, 55 nm, 60 nm, and 65 nm are expressed by blue, pink, green, purple, and red lines, respectively.

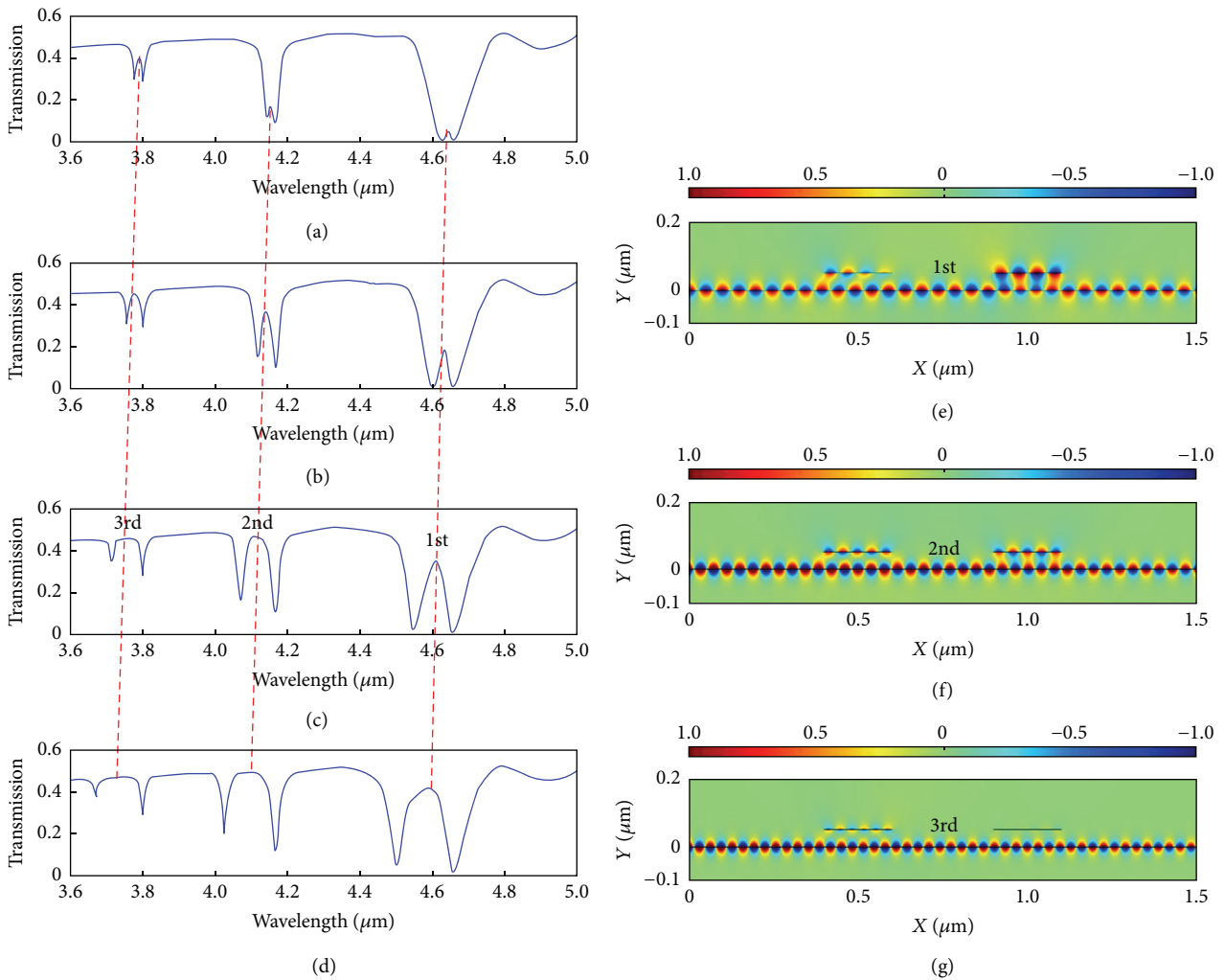


FIGURE 5: The Fermi level  $E_f$  of left graphene sheet is fixed at 0.42 eV and the Fermi level  $E_f$  of right graphene sheet is set as follows: (a)  $E_f = 0.425$  eV, (b)  $E_f = 0.43$  eV, (c)  $E_f = 0.44$  eV, and (d)  $E_f = 0.46$  eV. The magnetic distributions  $|H_z|$  corresponding to the transparency peaks. (e)  $\lambda = 4.61$   $\mu\text{m}$  for 1st resonance mode. (f)  $\lambda = 4.11$   $\mu\text{m}$  for 2nd resonance mode. (g)  $\lambda = 3.76$   $\mu\text{m}$  for 3rd resonance mode.

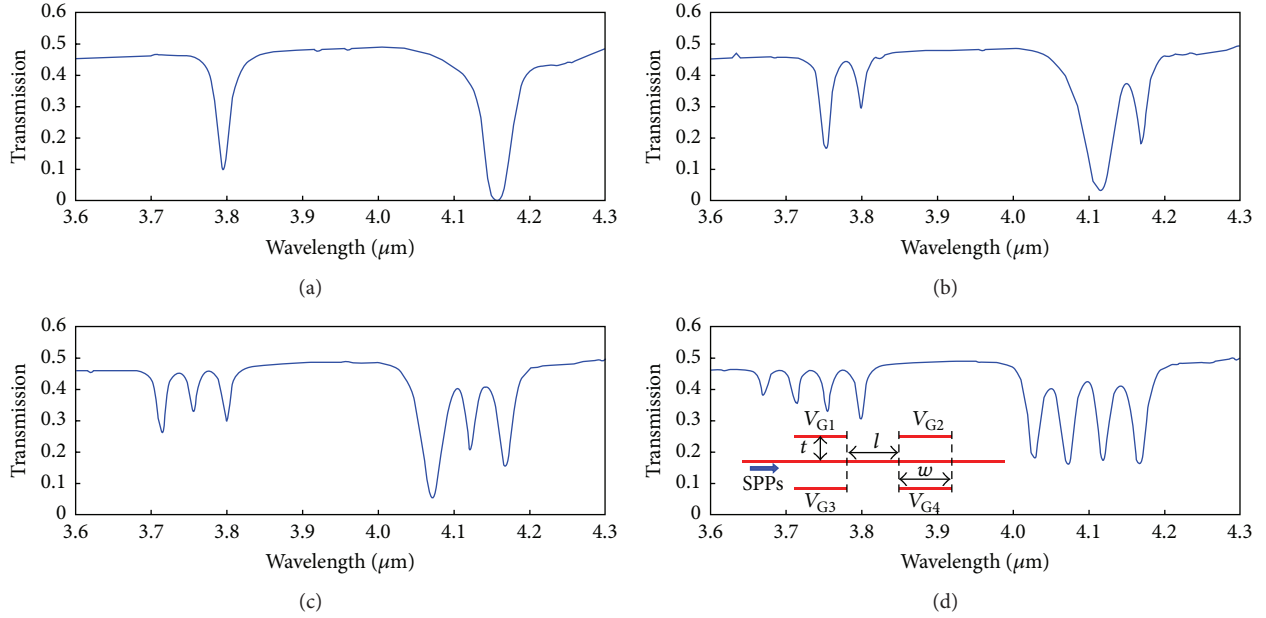


FIGURE 6: The transmission spectra of multipeak PIT. The Fermi level of graphene waveguide is fixed at 0.4 eV. (a)  $E_{f1} = E_{f2} = E_{f3} = E_{f4} = 0.42$  eV. (b)  $E_{f1} = E_{f2} = 0.42$  eV,  $E_{f3} = E_{f4} = 0.43$  eV. (c)  $E_{f1} = E_{f2} = 0.42$  eV,  $E_{f3} = 0.43$  eV, and  $E_{f4} = 0.44$  eV. (d)  $E_{f1} = 0.42$  eV,  $E_{f2} = 0.43$  eV,  $E_{f3} = 0.44$  eV, and  $E_{f4} = 0.45$  eV.

show obvious off-to-on feature and the transparency bands become broader with the  $\delta_i$  growing. The magnetic distributions  $|H_z|$  corresponding to the transparency peaks of 1st, 2nd, and 3rd resonance modes are depicted in Figures 5(e), 5(f), and 5(g). In this way, the tunable PIT effects based on graphene sheet resonators are achieved.

In this section, the phase coupling between the four graphene sheets structure has been investigated by contrasting with the two graphene sheets structure. The extra graphene sheets are placed to graphene waveguide symmetric position on the basis of two sheets structure, which is shown in insert picture of Figure 6(d). The transmission spectra of second-order mode and third-order mode are depicted in Figures 6(a), 6(b), 6(c), and 6(d); the modulation of multipeak PIT can be achieved by controlling the Fermi level of four graphene sheets. By adjusting Fermi level gradually can result in tunable off-to-on multipeak PIT feature. Figure 7 shows the transmission spectra in the mid-infrared region of two peaks PIT based on the four graphene sheets structure. The upper and lower picture of Figure 7 show the magnetic distributions of the second-order mode under  $\lambda_0 = 4.105 \mu\text{m}$ ,  $4.12 \mu\text{m}$ , and  $4.14 \mu\text{m}$ , which correspond to the standing wave modes originating from the splitting of the second-order resonance. In addition, Figure 8 shows the transmission spectra of three peaks PIT based on the four graphene sheets structure. The upper and lower picture of Figure 8 show the magnetic distributions of the second-order mode under  $\lambda_0 = 4.05 \mu\text{m}$ ,  $4.1 \mu\text{m}$ , and  $4.12 \mu\text{m}$ . Due to the great difference of resonant wavelengths in first-order mode from Figure 3(a), the first-order mode of multipeak PIT has disorderly phenomenon because of the interference between two random resonance wavelengths.

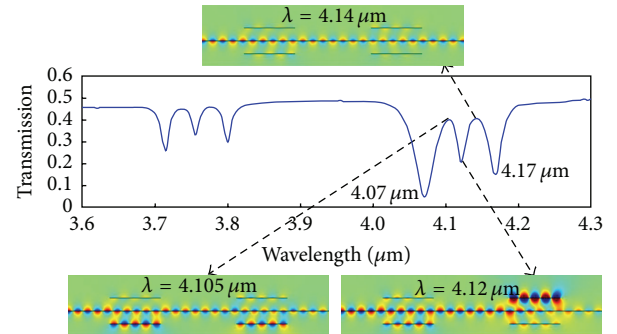


FIGURE 7: The transmission spectra of two-peak PIT based on the four graphene sheets structure. Magnetic field distributions of the 2nd mode under  $\lambda_0 = 4.105 \mu\text{m}$ ,  $4.12 \mu\text{m}$ , and  $4.14 \mu\text{m}$ , respectively.

#### 4. Conclusion

In this paper, we have numerically investigated a multimode plasmonically induced transparency (PIT) device operating in the mid-infrared region. The proposed model consisted of one graphene ribbon as main waveguide and two graphene sheets as resonators. In phase coupling systems, the simulation results evidently demonstrate the multimode PIT phenomenon. On the other hand, the multipeak PIT spectral responses emerge in four graphene sheets system. For phase coupling, the off-to-on PIT feature could be effectively achieved by varying the Fermi level of one graphene sheet resonator. Besides, by turning off one graphene resonator, this structure can achieve filter effects. The filter wavelength can be adjusted via varying the Fermi energy of graphene

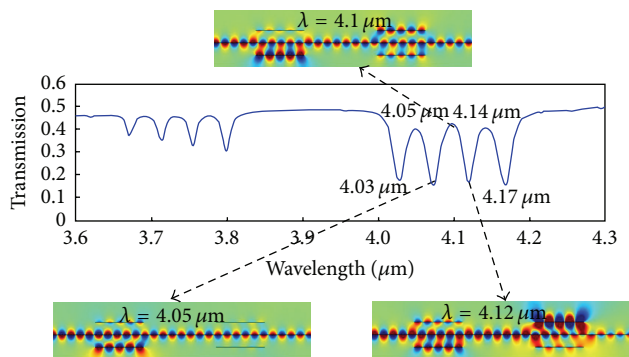


FIGURE 8: The transmission spectra of three-peak PIT based on the four graphene sheets structure. Magnetic distributions of the 2nd mode under  $\lambda_0 = 4.05 \mu\text{m}$ ,  $4.1 \mu\text{m}$ , and  $4.12 \mu\text{m}$ , respectively.

resonator without optimizing geometric parameters. All of the observed PIT spectral features are of great importance to provide platforms for the design of the dynamical control PIT systems. The work may open up new ways for the development of compact thermal plasmonic devices such as tunable sensors, spectral splitter, and switchers in mid-infrared region.

## Competing Interests

The authors declare that they have no competing interests.

## Acknowledgments

This work is supported by the National Basic Research Program of China (Grant no. 2013CBA01702), the National Natural Science Foundation of China (Grant no. 61377016, 61308017, and 11504139), and the Natural Science Foundation of Jiangsu Province (Grant no. BK20140167).

## References

- [1] P. Berini, "Plasmon-polariton waves guided by thin lossy metal films of finite width: bound modes of symmetric structures," *Physical Review B*, vol. 61, no. 15, pp. 10484–10503, 2000.
- [2] W. L. Barnes, A. Dereux, and T. W. Ebbesen, "Surface plasmon subwavelength optics," *Nature*, vol. 424, no. 6950, pp. 824–830, 2003.
- [3] K.-J. Boller, A. Imamolu, and S. E. Harris, "Observation of electromagnetically induced transparency," *Physical Review Letters*, vol. 66, no. 20, pp. 2593–2596, 1991.
- [4] S. E. Harris, "Electromagnetically induced transparency," *Physics Today*, vol. 50, no. 7, pp. 36–42, 1997.
- [5] B. J. Tang, J. Wang, X. Xia, X. Liang, C. Song, and S. Qu, "Plasmonic-induced transparency and unidirectional control based on the waveguide structure with quadrant ring resonators," *Applied Physics Express*, vol. 8, no. 3, Article ID 032202, 2015.
- [6] J. Wang, B. Yuan, C. Fan et al., "A novel planar metamaterial design for electromagnetically induced transparency and slow light," *Optics Express*, vol. 21, no. 21, pp. 25159–25166, 2013.
- [7] T. F. Krauss, "Why do we need slow light?" *Nature Photonics*, vol. 2, no. 8, pp. 448–450, 2008.
- [8] M. Fleischhauer, A. Imamoglu, and P. J. Marangos, "Electromagnetically induced transparency," *Reviews of Modern Physics*, vol. 77, no. 2, pp. 633–673, 2005.
- [9] S. Zhang, D. A. Genov, Y. Wang, M. Liu, and X. Zhang, "Plasmon-induced transparency in metamaterials," *Physical Review Letters*, vol. 101, no. 4, Article ID 047401, 2008.
- [10] N. Liu, L. Langguth, T. Weiss et al., "Plasmonic analogue of electromagnetically induced transparency at the Drude damping limit," *Nature Materials*, vol. 8, no. 9, pp. 758–762, 2009.
- [11] J. Gu, R. Singh, X. Liu et al., "Active control of electromagnetically induced transparency analogue in terahertz metamaterials," *Nature Communications*, vol. 3, article 1151, 2012.
- [12] Y. H. Guo, L. Yan, W. Pan et al., "Electromagnetically induced transparency (EIT)-like transmission in side-coupled complementary split-ring resonators," *Optics Express*, vol. 20, no. 22, pp. 24348–24355, 2012.
- [13] X. Liu, J. Gu, R. Singh et al., "Electromagnetically induced transparency in terahertz plasmonic metamaterials via dual excitation pathways of the dark mode," *Applied Physics Letters*, vol. 100, no. 13, Article ID 131101, 2012.
- [14] G. Cao, H. Li, S. Zhan et al., "Formation and evolution mechanisms of plasmon-induced transparency in MDM waveguide with two stub resonators," *Optics Express*, vol. 21, no. 8, pp. 9198–9205, 2013.
- [15] X. Xia, J. Wang, F. Zhang et al., "Multi-mode plasmonically induced transparency in dual coupled graphene-integrated ring resonators," *Plasmonics*, vol. 10, no. 6, pp. 1409–1415, 2015.
- [16] X. Wang, X. Xia, J. Wang, F. Zhang, Z. Hu, and C. Liu, "Tunable plasmonically induced transparency with unsymmetrical graphene-ring resonators," *Journal of Applied Physics*, vol. 118, no. 1, Article ID 013101, 2015.
- [17] X. Y. Duan, S. Chen, H. Cheng, Z. Li, and J. Tian, "Dynamically tunable plasmonically induced transparency by planar hybrid metamaterial," *Optics Letters*, vol. 38, no. 4, pp. 483–485, 2013.
- [18] A. H. Castro Neto, F. Guinea, N. M. R. Peres, K. S. Novoselov, and A. K. Geim, "The electronic properties of graphene," *Reviews of Modern Physics*, vol. 81, no. 1, pp. 109–162, 2009.
- [19] L. Ju, B. Geng, J. Horng et al., "Graphene plasmonics for tunable terahertz metamaterials," *Nature Nanotechnology*, vol. 6, no. 10, pp. 630–634, 2010.
- [20] B. Wang, X. Zhang, X. Yuan, and J. Teng, "Optical coupling of surface plasmons between graphene sheets," *Applied Physics Letters*, vol. 100, Article ID 131111, 2012.
- [21] B. Wang, X. Zhang, F. J. García-Vidal, X. Yuan, and J. Teng, "Strong coupling of surface plasmon polaritons in monolayer graphene sheet arrays," *Physical Review Letters*, vol. 109, no. 7, Article ID 073901, 2012.
- [22] A. K. Geim, "Graphene: status and prospects," *Science*, vol. 324, no. 5934, pp. 1530–1534, 2009.
- [23] Q. Bao, H. Zhang, B. Wang et al., "Broadband graphene polarizer," *Nature Photonics*, vol. 5, no. 7, pp. 411–415, 2011.
- [24] M. Liu, X. Yin, E. Ulin-Avila et al., "A graphene-based broadband optical modulator," *Nature*, vol. 474, no. 7349, pp. 64–67, 2011.
- [25] S. Thongrattanasiri, F. H. L. Koppens, and F. J. García de Abajo, "Complete optical absorption in periodically patterned graphene," *Physical Review Letters*, vol. 108, no. 4, Article ID 047401, 2012.
- [26] A. Vakil and N. Engheta, "Transformation optics using graphene," *Science*, vol. 332, no. 6035, pp. 1291–1294, 2011.

- [27] C. Zeng, J. Guo, and X. Liu, "High-contrast electro-optic modulation of spatial light induced by graphene-integrated Fabry-Pérot microcavity," *Applied Physics Letters*, vol. 105, Article ID 121103, 2014.
- [28] X. Shi, D. Han, Y. Dai et al., "Plasmonic analog of electromagnetically induced transparency in nanostructure graphene," *Optics Express*, vol. 21, no. 23, pp. 28438–28443, 2013.
- [29] P.-Y. Chen and A. Alù, "Atomically thin surface cloak using graphene monolayers," *ACS Nano*, vol. 5, no. 7, pp. 5855–5863, 2011.
- [30] G. W. Hanson, "Quasi-transverse electromagnetic modes supported by a graphene parallel-plate waveguide," *Journal of Applied Physics*, vol. 104, no. 8, Article ID 084314, 2008.
- [31] K. S. Novoselov, A. K. Geim, S. V. Morozov et al., "Electric field effect in atomically thin carbon films," *Science*, vol. 306, no. 5696, pp. 666–669, 2004.
- [32] H.-S. Chu and C. How Gan, "Active plasmonic switching at mid-infrared wavelengths with graphene ribbon arrays," *Applied Physics Letters*, vol. 102, no. 23, Article ID 231107, 2013.
- [33] J. Christensen, A. Manjavacas, S. Thongrattanasiri, F. H. L. Koppens, and F. J. García De Abajo, "Graphene plasmon waveguiding and hybridization in individual and paired nanoribbons," *ACS Nano*, vol. 6, no. 1, pp. 431–440, 2012.
- [34] H. Lu, "Plasmonic characteristics in nanoscale graphene resonator-coupled waveguides," *Applied Physics B*, vol. 118, no. 1, pp. 61–67, 2015.
- [35] J. L. Garcia-Pomar, A. Y. Nikitin, and L. Martin-Moreno, "Scattering of graphene plasmons by defects in the graphene sheet," *ACS Nano*, vol. 7, no. 6, pp. 4988–4994, 2013.
- [36] A. Y. Nikitin, T. Low, and L. Martin-Moreno, "Anomalous reflection phase of graphene plasmons and its influence on resonators," *Physical Review B*, vol. 90, Article ID 041407, 2014.
- [37] Q. Li, T. Wang, Y. Su, M. Yan, and M. Qiu, "Coupled mode theory analysis of mode-splitting in coupled cavity system," *Optics Express*, vol. 18, no. 8, pp. 8367–8382, 2010.